Irradiation Processing of Major Dust Components

Dissertation
zur Erlangung des akademischen Grades

doctor rerum naturalium (Dr. rer. nat.)

vorgelegt dem Rat der Physikalisch-Astronomischen Fakultät
der Friedrich-Schiller-Universität Jena

von Hagen Walter MSc
geboren am 23. Januar 1989 in Nordhauen

Gutachter

1. **Prof. Dr. Thomas Henning**
Max-Planck-Institut für Astronomie Heidelberg
2. **Dr. Vito Mennella**
Osservatorio Astronomico di Capodimonte Neapel
3. **Prof. Dr. Gerhard Wurm**
Universität Duisburg-Essen

Tag der Disputation: 27.07.2017

Abstract

German Abstract

In dieser Arbeit wurde das Verhalten amorphen, fullerenartigen Rußes unter UV-Bestrahlung untersucht. Weiterhin wurde der Einfluss von Eisennanopartikeln bei der Produktion und bei der Bestrahlung erforscht. Die Herstellung der Materialien erfolgte mittels Laserablation. Die Charakterisierung der Proben erfolgte spektroskopisch vom NIR bis ins VUV sowie mit dem HRTEM.

Neben wasserstofffreien und wasserstoffhaltigen amorphen, fullerenartigen Rußen wurden von Graphenschichten umhüllte Eisennanopartikel in einer amorphen Kohlenstoffmatrix mithilfe der Laserablation hergestellt. Die gleichzeitige Verdampfung von Kohlenstoff und Eisen bewirkt, dass sich Kohlenstoff während der Kondensation im Eisen löst und, wenn das Eisen erstarrt, als aromatische Hülle um die Eisennanoteilchen auskristallisiert. Die gleichzeitige Verdampfung von Kohlenstoff schützt das Eisen durch seine reduzierende Wirkung vor Oxidation. Die Größe und Verteilung der Eisennanopartikel lässt sich im Rahmen der Laserablation mit dem Druck der Kühlgasatmosphäre und deren Wasserstoffanteil grob regulieren. Die Zahl der Graphenschichten um ein Eisennanoteilchen hängt hauptsächlich von der Größe des Eisenteilchens ab. Außer einer allgemein höheren Absorption gegenüber amorphem Kohlenstoff gibt es keine auffallenden spektroskopischen Signaturen.

Das Hauptanliegen dieser Arbeit ist die Untersuchung durch UV-Strahlung hervorgerufener Veränderung der Ruße. Die Energie der UV-Photonen reichte vom nahen UV mit $6.3\,eV$ herunter bis ins harte UV bei $500\,eV$. Niederenergetische Photonen mit Energien kleiner als der Bindungsenergie von $C{=}C$ bewirken eine leichte Graphitisierung des Materials sowie Dehydrierung. Energien, die höher sind als die Bindungsspaltungsenergie von Kohlenstoffdoppelbindungen, bewirken lokal die Ausbildung von Krümmungen in Graphenschichten. Diese Krümmungen werden durch Stone-Wales-Thrower-Defekte verursacht. Die Krümmungen haben eine deutlich sichtbare spektroskopische Signatur als Bande bei etwa 210 bis $200\,nm$. Dabei handelt es sich um p_z-Orbitale, die nicht mehr orthogonal zu den sp^2-Hybridorbitalen stehen und den Charakter des Materials in Richtung sp^3 ver-

schieben.
Es deutet vieles daraufhin, dass, sobald die Photonenenergie eine Schwelle von $9\,eV$ überschreitet und STW-Defekte erzeugen kann, die Krümmung nicht weiter mit der Photonenenergie korreliert. Die Morphologie des Ausgangsmaterials scheint einen deutlicheren Einfluss auf die zukünftige Krümmung zu haben. Das Vorhandensein von Eisennanopartikeln, bzw. deren Graphenschichten, beeinflusst die Stärke der entstehenden Bande und anscheinend auch deren Lage, d.h. den Krümmungsradius der Graphenschichten. Ein eindeutiger Zusammenhang konnte jedoch noch nicht gefunden werden.

Ein weiterer Prozess, der mit der Ausbildung der Bande konkurriert, ist die Graphitisierung, welche die Bande, die durch die Krümmungen hervorgerufen wird, maskieren kann. Dies ist insbesondere dann der Fall, wenn die Eindringtiefe der zum Bestrahlen verwendeten Photonen kleiner als die Dicke der bestrahlten Schicht ist. Dieser Effekt beruht prinzipiell darauf, dass bei der Wechselwirkung der Photonen mit der Rußschicht niederenergetische Sekundärphotonen entstehen, die erst in tiefer liegenden Schichten absorbiert werden und Graphitisierung hervorrufen können.

English Abstract

In this work the irradiation behaviour of amorphous, fullerene-like soot upon UV-irradiation was investigated. Furthermore, the influence of iron nanoparticles on the formation and processing of the soot were subject to investigation, too. The samples were produced by means of laser-ablation. The characterization of the samples was done spectroscopically from the NIR to the VUV, and via HRTEM.

Aside from hydrogenated and hydrogen-free amorphous, fullerene-like soot, graphene-covered iron nanoparticles embedded in a matrix of amorphous carbon were produced using laser-ablation. The simultaneous evaporation of carbon and iron forces the carbon to dissolve in the iron and is precipitated upon cooling. Thus aromatic mantles are formed around the iron nanoparticles. The simultaneous evaporation inhibits the oxidation of the iron nanoparticles by creating a strongly-reducing atmosphere. The size and distribution of the iron nanoparticles can be controlled coarsely by means of the pressure and hydrogen-content of the quenching atmosphere. The number of graphene layers around the iron depends mainly on the size of the iron nanoparticles. Aside from a general increase of the mass absorption coefficient with respect to amorphous carbon, there are no significant spectral features.

The main goal of this thesis is the investigation of the UV-irradiation-induced

processing of soot. The energy of the UV-photons ranges from the near-UV at $6.3\,eV$ to the hard UV at $500\,eV$. Lower-energy photons with energies below the binding energy of $C{=}C$ result in a slight graphitization of the material as well as dehydrogenation. Energies that are higher than the binding energy of double-bound carbon, cause local bendings in the graphene structures. These curved structures are caused by Stone-Wales-Thrower defects that are induced by the photons. These curved structures bear a clearly-detectable spectroscopic feature giving rise to a band between $210\,nm$ and $200\,nm$. This band is caused by p_z-orbitals that are no longer orthogonally-aligned to the sp^2 hybrid orbitals. Thus, they shift the character of the material more towards sp^3 hybridized carbon.

It points to the notion that the photon energy, once exceeding a threshold of $9\,eV$ and becoming able to induce STW defects, does not correlate with the curvature radius of the processed carbon. The morphology of the precursor material seems to have a non-negligible influence on the future curvature. The presence of iron nanoparticles, or their graphene layers respectively, influences the strength and its central wavelength, i.e. its curvature. Yet, a clear correlation could not be established.

Another process that competes with the formation of the band, is graphitization, which is able to mask the curvature-related band. This is especially the case, when the penetration depth of the incident photons is smaller than the thickness of the sample layer. This effect is, in principle, caused by the interaction of secondary, lower-energy photons that are absorbed in deeper regions of the soot layer.

Contents

Abbreviations

AC	amorphous carbon
ArF	UV-photons from argon-fluoride laser
DUV	UV-photons generated by D_2-gas discharge lamp
FeAC	iron-containing amorphous carbon produced in an hydrogen-free atmosphere
FeHAC	iron-containing amorphous carbon produced in an hydrogen-containing atmosphere
FWHM	full width at half of the maximum
HAC	hydrogenated amorphous carbon
HUV	UV-photons generated by H_2-gas discharge lamp
IR	infrared
MCM	Monte-Carlo method
NIR	near infrared
NEXAFS	near edge X-ray fine structure spectroscopy
OLC	onion-like carbon-related band
ROD	region of domination
STW	Stone-Thrower-Wales (defect)
UV	general ultra-violet
VIS	visible range of electro-magnetic spectrum
VUV	vacuum ultra-violet, $\lambda < 190\,nm$
X	X-ray photons of $500\,eV$
XUV	extreme ultra-violet: photons from multi-harmonics laser in the range from $20\,eV$ to $60\,eV$

Chapter 1

Introduction

1.1 Foreword

Carbon is one of the most interesting and important elements, as it can form one-, two- and three-dimensional structures. The major part of carbon dust is formed by AGB stars, where it is expected to not be graphitic (Henning et al., 2004), and it is ejected by stellar winds into the interstellar medium (Cherchneff, 1998). There, however, in the diffuse interstellar medium, it exists as both graphitic material and as small molecules, such as gaseous PAHs or C-chains (Henning et al., 2004). In the proximity of their parent stars, the carbon and its derived molecules experience shocks and cosmic rays (Cherchneff, 2006). Later on, when they have reached the ISM, it is mostly collisions with energetic particles and photons, as well as supernovae shocks that influence the chemistry and morphology of the molecules and clusters derived from carbon.

Carbon forms a manifold of different materials that can be found in space: graphite and graphene, fullerenes (Bernard-Salas et al., 2012), diamonds and amorphous composites. Furthermore, as hydrogen is the major component of the interstellar and circumstellar gas, it forms many molecules with it — from simple ones like methane CH_4 to more complex polycyclic aromatic hydrogenated carbonaceous species, derived from benzene, like the circular coronene $C_{24}H_{12}$.

When in 1965 the interstellar extinction bump at $217\,nm$ (Figure 1.2) was discovered by Stecher (1969); Stecher and Donn (1965), soon it became clear that the material in question was derived from carbon. It is of particular interest, that the position of this band is relatively stable around $217\,nm$. However, this extinction feature might shift as far towards the red as $235\,nm$ (Blasberger et al., 2017). Schnaiter et al. (1996) found that the position of the $\pi \rightarrow \pi^{\star}$-transition, which is thought to be responsible for this band, highly depends on the degree

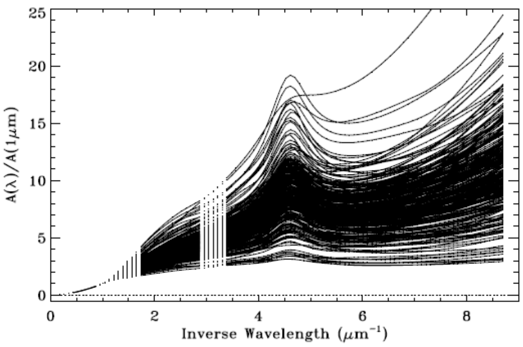

Figure 1.1: Analytical representations of 328 Galactic UV-through-IR extinction curves plotted in their IR-normalized form $A(\lambda)/A(1\,\mu m)$. This plot illustrates the variations of the carrier curve of the interstellar extinction bump. Taken from Fitzpatrick and Massa (2007).

of coagulation and size of the carbon particles. Furthermore, even though the position is mostly stable, the width of this feature, as well as its strength and the shape of its carrier curve are subject to wider variations (Figure 1.1).

An answer for the specifics of the material causing this feature, was long due and still is (Blasberger et al., 2017). But in recent years approaches have been made to resolve this question. Among the attempts were UV-treated carbonaceous matter by e.g. Mennella et al. (1996) and Blanco et al. (1993), mixtures of PAHs by Steglich et al. (2010), slow deposition by Duley and Hu (2012) and carbon particles of specific size and coagulation (Schnaiter et al., 1996, 1998; Rouleau et al., 1997), or carbonaceous species of the quenched plasma of hydrocarbons (Sakata et al., 1994). The first way proved to be the more successful one. Additionally, Chhowalla et al. (2003) proposed carbon onions as carrier of the interstellar extinction feature.

Another key element contributing to dust, is iron which is formed in supernovae (Dwek, 2016). However, it is still unclear in what form it is released into space — whether it is ejected as iron granules, whether it is locked into magnesium-rich silicates or else. But more recent research (Dwek, 2016) suggests, that it is ejected in gaseous form into the ISM. *Pure iron grains are rare in the universe* — that is the name paper by the Japanese researchers Kimura et al. (2017). At least metallic iron clusters are invisible, according to Cherchneff and Dwek (2010). Some authors (Ristorcelli and Klotz, 1997; Marty et al., 1994) propose that iron could serve as a catalyst for the formation of PAHs and other carbonaceous species in space. On earth, however, iron proved to be a useful catalyst for the growth of carbon nano-tubes (Dai, 2001). Dunk et al. (2013) urge, accordingly, that metallofullerenes should be taken into consideration as well. We, therefore, conclude that the incorporation of iron into carbonaceous materials is well worth

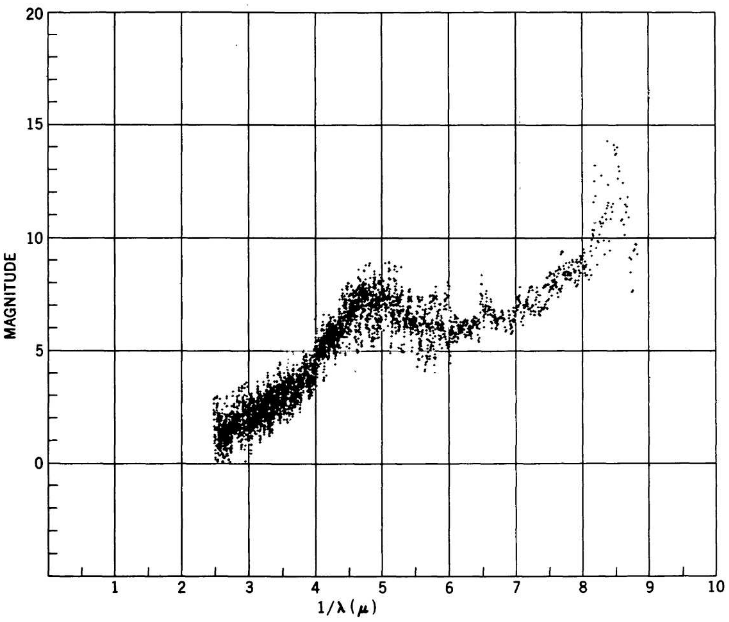

Figure 1.2: The interstellar extinction bump at 217 nm, discovered by Stecher in the 1960s. Taken from Stecher (1969).

investing, although authors such as Jones (2013) assume that the inclusion of pure iron into carbonaceous species is of no great importance. However, Dwek (2016) proposes that it is somehow locked up. Jones (1990) assumes that iron is very likely to react with e.g. sulphur or oxygen instead of remaining plain and pure iron. Aside from its astrophysical relevance, there seems to be a demand for carbon-iron granules, especially for core-shell particles with separated phases. Various techniques have already been applied to produces such species: detonations by Luo et al. (2012) with an average particle size of 18 to 55 nm or even by acid corrosion of cast iron by Wang et al. (2014) yielding sizes of some tens of microns.

In this thesis we aim to investigate two connected topics. Firstly, it is the behaviour of refractory carbonaceous materials under energetic photon irradiation that shall be studied. Secondly, the interaction of carbon and iron shall be investigated: the grain formation of carbonaceous materials is thought to be different, when iron is present. Furthermore, the presence and incorporation of iron into carbon might influence its behaviour under photon-irradiation.

1.2 Morphology and Electronic Properties of Carbon

Many different allotropes of carbon are known, with the most prominent ones being diamond, graphite, graphene and fullerenes (left-hand side of Figure 1.5).

Carbon is quite unique, even within the fourth group of the periodic table. Its electron configuration is $1s^2 2s^2 2p^2$. Whenever carbon forms a structure, it tends to hybridize its orbitals, allowing it to bind to up to four other atoms. Amorphous carbon is a special kind of carbonaceous material where all kinds of hybridization as well as aromatic and aliphatic regions are present. Figure 1.3 illustrates the concept of amorphous carbonaceous materials (AC). When carbon hybridizes its four outer electrons to form sp^3-orbitals, the electrons assume the nodes of a tetrahedron around the nucleus. These four bonds are identical and allow the carbon structure to become three-dimensional. Methane and diamonds are compounds where the carbon is fully sp^3-hybridized. The angles between the orbitals are 109.47 degree.

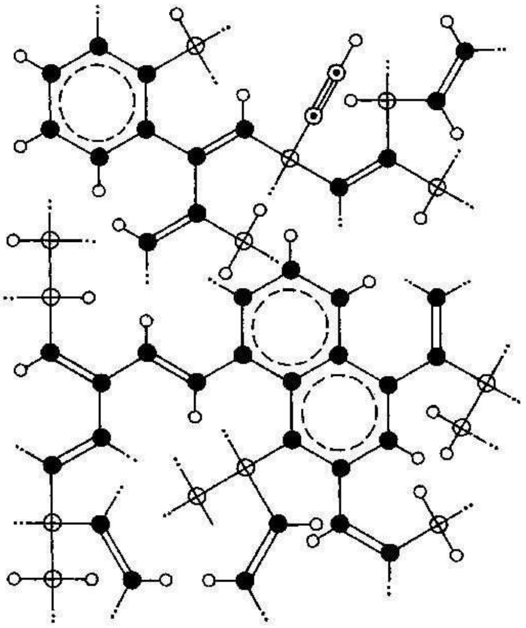

Figure 1.3: This image shows the variety of local structures that one encounters in hydrogenated amorphous carbon, taken from Jones et al. (1990). The circles with a cross represent sp^3-carbon, those that are black represent sp^2-carbon and the white circles with small black dots inside are sp^1-hybridized carbon atoms. The smaller, hollow circles represent hydrogen. The dashed line represents delocalised π-electrons.

Fully sp^2-hybridized carbon is found in graphite and graphene. The term sp^2 hybridization means that one of the $2s$-electrons is promoted into the $2p$-orbital to create three energetically identical orbitals — called sp^2-orbitals. The carbon atom then has three sp^2-orbitals that lie in a plane with an angle of 120 degree between them, and a p-orbital that is normal to the plane of the three hybrid-orbitals. The structures sp^2-hybridized carbons can form, are two-dimensional. The sp^2-hybridized atoms are able to form six-membered rings with three single bonds and three double bonds. The double-bonds are not localised in that case. Structures with delocalised electrons are called aromatic.

Rolling such a graphene structure produces carbon-nanotubes. The hybridization of these tubes is different from graphene, diamond and fullerenes, as it can be sp^x with $2 < x < 3$. This is due to the bending of the layer. Thereby the distances and the angles between the atoms are varied and the remaining $2p$-orbitals that are perpendicular to the six-membered ring, are no longer perpendicular to the other orbitals of its parent atom (illustrated on the right hand side of Figure 1.5) (Reich et al., 2004). This causes an increase of the hybridization, as the angles of the sp^2-orbitals are deviating more and more towards the angles expected in sp^3-orbitals, as Zhao et al. (2004) have shown.

Rance et al. (2010) have found a relation between the diameter of a carbon nanotube (rolled-up graphene) and the position of its π-plasmon band:

$$E_\pi = 4.80\,eV + \frac{0.7\,eV \cdot nm^2}{d_{NT}^2}. \tag{1.1}$$

The substitution of a six-membered ring by a five-membered one also leads to a curvature in a graphitic structure. Furthermore, high energetic particles like neutrons can induce so-called Stone-Thrower-Wales defects (Fujimori et al., 2012; Stone and Wales, 1986), that is two six-membered rings transform into a heptagon and a pentagon Figure 1.4, which results in a curvature.

Carbonaceous matter, produced by means of laser ablation, mostly consists of randomly distributed aromatic sub-units (graphene-layers), and aliphatic areas in-between (Figure 1.6), so-called arophatics (Micelotta et al., 2012). The aromatic regions are not always plane, but tend to be strongly curved and are similar to fragments of fullerenes.

1.3 Aims of the Thesis

In this thesis, I want to investigate the irradiation-induced restructuring processes that affect fullerene-like soot, as UV-processed carbonaceous matter is a promising candidate for the role of the carrier of the interstellar extinction bump at $217.5\,nm$ ($4.6\,\mu m^{-1}$). Especially, I aim at finding a morphological link between the $217\,nm$

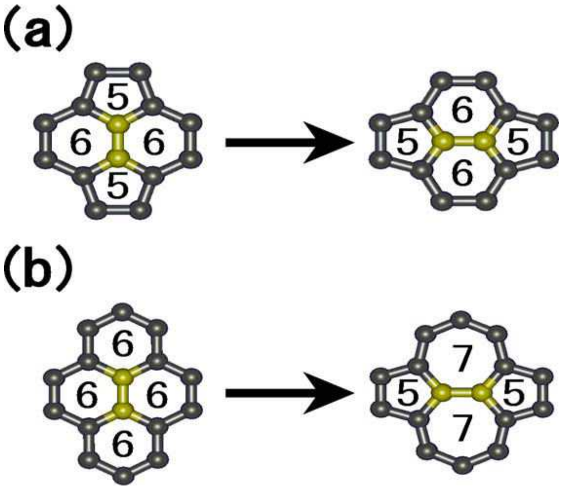

Figure 1.4: The upper image illustrates the Stone-Wales transformation. The lower one shows the formation of a Stone-Thrower-Wales defect. Taken from Fujimori et al. (2012).

bump and morphological features. I investigate a wide range of photon energies, and different precursor materials that are composed of carbon, hydrogen and iron, which is already known to influence the chemistry of hydro-carbons and carbon nano-tubes.

As precursors for the irradiated carbonaceous dust, hydrogenated and hydrogen-free amorphous, fullerene-like carbonaceous dust is produced by means of laser ablation. Furthermore, in order to investigate the role of iron under the irradiation of carbonaceous dust, iron-containing carbonaceous dust is produced both under a hydrogen-free and hydrogen-bearing atmosphere.

The effects of a wide range of photon energies on these carbonaceous materials is investigated. Starting with low-energy photons from an ArF-laser ($6.4\,eV$) up to the $Ly\alpha$-line by means of deuterium ($7.4\,eV$) and hydrogen ($10.2\,eV$) lamps, we investigate the effect of the photons that dominate the interstellar medium. Then, I proceed to higher energy photons that are emitted by hot plasmas, young stars and supernovae, by means of a multi-harmonics laser ($20-60\,eV$) and synchrotron radiation ($500\,eV$ and wide range *white light*).

The materials and their changes are characterized mainly by spectroscopy covering a range from $0.5\,\mu m^{-1}$ to $7.5\,\mu m^{-1}$ ($0.5-9.5\,eV$). The morphological changes are analyzed via high resolution transmission electron microscopy (HRTEM). Furthermore, near edge X-ray absorption fine structure spectroscopy (NEXAFS) is also applied to observe the bonding situation in some of the samples. Finally, the findings are combined to find a link between the spectral and morphological changes in the light of the $217.5\,nm$ extinction bump.

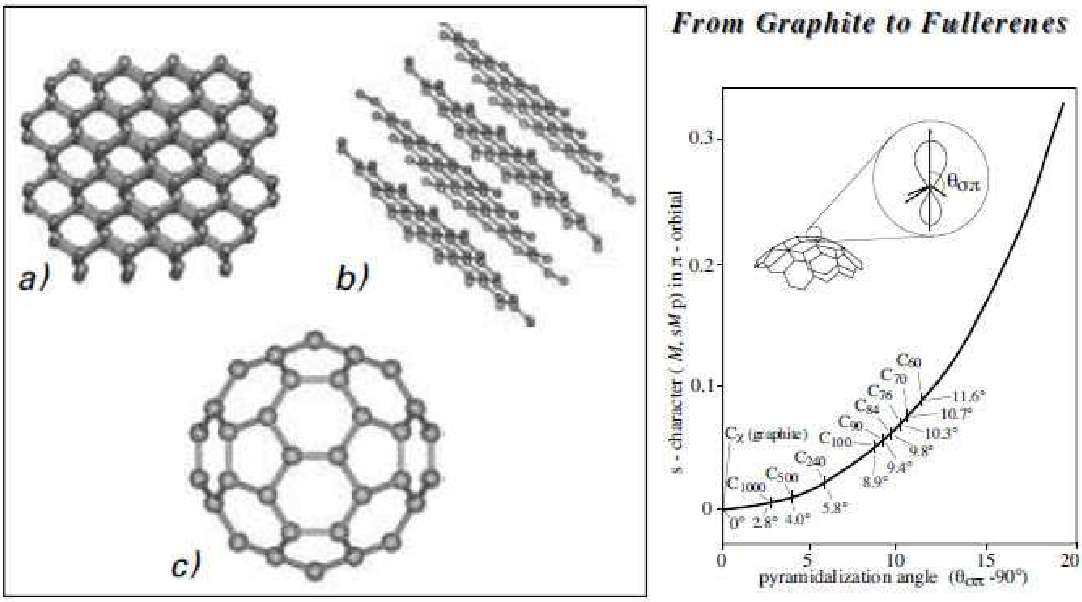

Figure 1.5: The left hand side shows three modifications of carbon: *a* diamond, *b* graphite and *c* a C_{60}-fullerene. The right hand side shows the relation between the size of a bucky ball, the pyramidic angle of the carbon atoms and its hybridization state. Both taken from Henning et al. (2004).

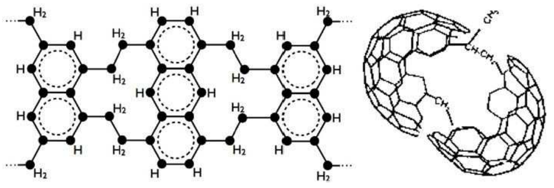

Figure 1.6: The image on the left, taken from Micelotta et al. (2012), shows a very regular and primitive instance of an arophatic structure: aromatic regions connected by bridging aliphatic regions. The image on the right, taken from Jäger et al. (2008b), shows two fullerene-fragments connected by sp^3-hybridized carbon chains — a more realistic version of a so-called arophatic structure.

In the following sections I will give a brief overview of the general processing and irradiation processing of carbonaceous materials. Thereupon, the analytical and experimental techniques as well as the setup will be explained in detail. This is followed by a presentation of the results and their interpretation. I will conclude with the astrophysical implications yielded by this work as well as with a summary and an outlook on how to expand the investigation of irradiation processing.

Chapter 2

Fundamentals

2.1 Laser Ablation

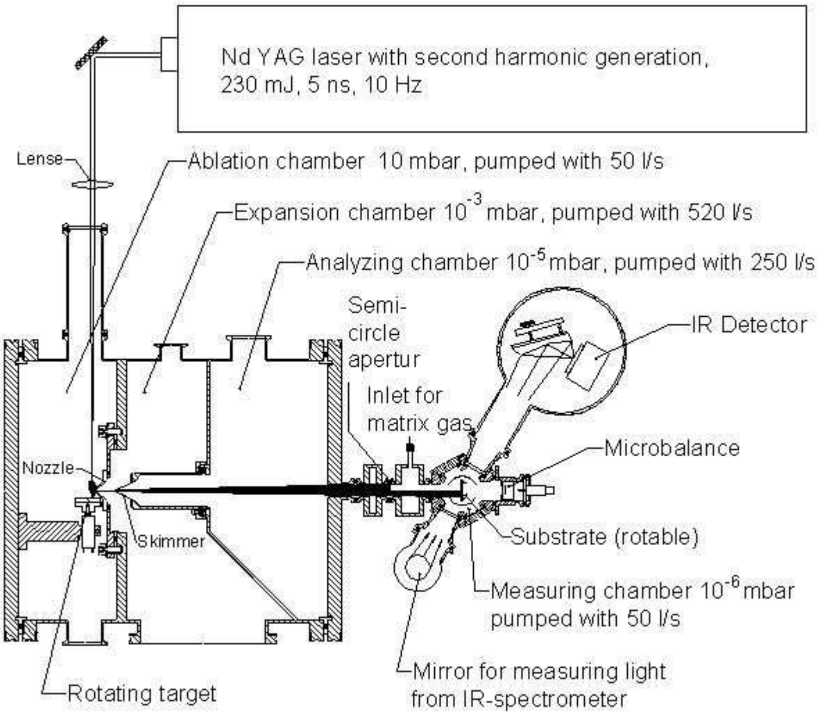

Figure 2.1: A sketch depicting the laser ablation set-up.

All samples have been produced using the method of laser ablation (Figure 2.1). With this technique a solid target is vaporized by a pulsed laser under a quenching gas atmosphere. Local super-saturation of the atmosphere causes particles to condense rapidly out of an inequilibrium regime. These particles are then rapidly extracted and cooled by supersonic expansion.

The laser ablation setup, shown in Figure 2.1, consists of four sections. The first section is a big chamber containing the rotating target and the gas inlet.

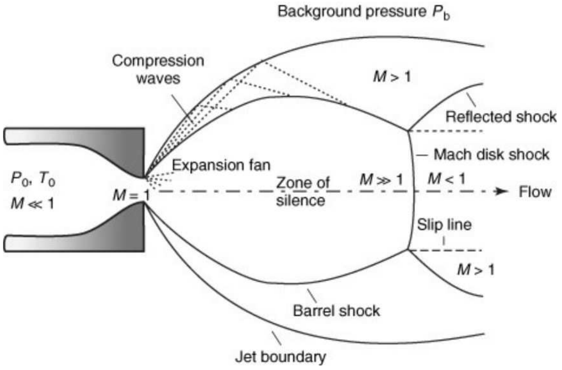

Figure 2.2: The image illustrates the pressure situation of a particle beam leaving a nozzle. The aim of the skimmer of the laserablation setup (Figure 2.1) is to extract the particle beam as long as it is in the zone of silence to prevent further coagulation. Taken from Scoles et al. (1988).

This chamber is connected by a nozzle to the second chamber. The target in the first chamber is vaporised to form a plasma plume by a laser beam (Nd:YAG, 532nm, 10Hz) coming from above, in an atmosphere of typically 1 to $10\,Torr$. The plasma is then quenched by the gas. The quenching results in the formation of particles, which condense as the atmosphere is rapidly saturated locally due to the cooling. The pressure difference to the second chamber whose pressure is well below 10^{-2}mbar, drags the particles through the nozzle with a gas stream. Passing through the nozzle they form a beam and are rapidly cooled by supersonic expansion. The second chamber serves to cool the particles and expand the particle beam to prevent further coagulation. This part of the setup itself is connected to the third chamber by a skimmer. The particle beam passes through that skimmer and is partially deposited on it. The skimmer helps to extract that part of the particle beam that is free from turbulences (Figure 2.2).

In the third chamber ($p \approx 10^{-7} \ldots 10^{-6}\,mbar$) the beam is cooled down for a second time by rapid expansion. In this chamber the particle beam can be collected on a substrate. But usually it only passes through that chamber which is connected by a gate valve and an aperture, which blocks half of the particle beam, to the fourth chamber, where the deposition on substrates usually takes place. The fourth chamber is pumped by an oil-free system and connected to an IR-spectrometer. Its pressure is the same as in the third chamber, so no significant cooling takes place.

The substrate is installed in such a way that half of the remaining particle beam covers the substrate and the other half covers a quartz microbalance located right behind the substrate, to monitor the deposition rate.

The energy density F is computed as (Gadallah et al., 2011)

$$F = \frac{E_{pulse}}{\pi r^2 \Delta t} \tag{2.1}$$

with E_{pulse} being the energy per pulse, πr^2 the spot size of the laser beam and Δt the duration of the pulse.

For iron-free samples prepared under helium-hydrogen atmosphere, the energy per pulse was $E_{pulse} = 50\,mJ$, for all other samples it was $E_{pulse} = 100\,mJ$. The typical spot size was about $2\,mm^2$, if unfocussed, and $1\,mm^2$, if focussed. With a pulse duration of 5ns, the power density is $0.5 \cdot 10^9\,Wcm^{-2}$ for $50\,mJ$-pulses, and $10^9\,Wcm^{-2}$ for $100\,mJ$-pulses. Iida and Yeung (1994) provide information about the temperature of the plasma with respect to the power density. However, it should be noted that the entire process is a non-equilibrium process, and in principle several kinds of temperature could be defined. According to Iida, the ionization temperature is around $25000\,K$ for the focussed $100\,mJ$-pulses and around $17000\,K$ for the $50\,mJ$-pulses. The respective vibrational temperature is slightly below $7000\,K$ and around $5000\,K$ respectively. Therefore, it is most reasonable to use the power density instead of any temperature to characterize the plasma.

2.2 Interaction of Photons with Matter

In this section the basics of the interaction between photons, electrons and bulk matter shall be described briefly.

2.2.1 Irradiation in General

Photons, depending on their energy, have a wide variety of effects on bulk material, molecules and atoms. IR photons cause the constituents of a bond to vibrate. More energetic photons in the visible and UV range manage to interact with the outer electrons of atoms and the corresponding bonds in molecules. In atoms the energy is sufficient to excite outer electrons into higher states and to even ionize them. The same happens in molecules, too, with the additional effect that UV photons suffice to break bonds in atoms. The even higher energy of X-photons interacts with electrons closer to the core, lifting them into higher states or emitting them altogether from their parent-atom.

Preparations

In order to avoid unwanted interactions with ambient dirt, oxygen and water, UV-irradiated samples are kept under vacuum during the processing. Below roughly 190nm, the photon source, too, needs to be kept under vacuum, as the photons are stopped by the ambient air not reaching the sample, and form ozone, oxides of nitrogen and other hazardous substances that can both chemically affect the sample and harm the experimenter and the equipment.

It is furthermore advisable to remove the ambient dirt having contaminated the samples before exposing them to UV photons. The contaminants might polymerize or react with the actual sample. Slow and careful heating is usually employed to remove any water and organic contaminants, while keeping the temperature sufficiently low to avoid thermal effects such as annealing and chemically reacting. Another method to remove ambient contaminants such as water is to place the sample under a sufficiently high vacuum for a long amount of time.

2.2.2 Penetration Depth

The penetration depth L_p is a quantity that describes, how far a photon beam can penetrate a material until its remaining intensity reaches a certain value. Here, the penetration depth shall be defined as the path a photon beam has to travel where its intensity has decreased to $\frac{1}{e}$:

$$I(x) = I_0 \exp\left(-\kappa \rho x\right) \tag{2.2}$$

$$I(L_p) = \frac{I_0}{e} = I_0 \exp\left(-\kappa \rho L_p\right) \tag{2.3}$$

$$L_p = \frac{1}{\kappa \rho} \tag{2.4}$$

Here, κ is the mass absorption coefficient and ρ is the density of the material. Since κ is wavelength-dependent, L_p is, too. Table 2.1 shows the dependence of the mass absorption coefficient of carbon and iron respectively in the XUV and X-ray range.

The penetration depth for electrons from ca. 10 to $200\,eV$ is typically in the range of 1 to $4\,nm$, according to Carette et al. (1977).

Carbon-Photon Interaction

In this section we will briefly cover the general effects that photons and electrons have on matter illustrated by the example of carbon. We will start with the effect photons have on matter and how they make atoms emit electrons. Then we will

	Carbon	**Iron**
λ	κ	κ
121.5	$2.96 \cdot 10^5$	$1.06 \cdot 10^5$
58.4	$6.03 \cdot 10^5$	$1.11 \cdot 10^5$
40.7	$3.01 \cdot 10^5$	$7.92 \cdot 10^4$
25.1	$1.02 \cdot 10^5$	$3.88 \cdot 10^5$
9.3	$1.33 \cdot 10^4$	$4.53 \cdot 10^4$
4.0	$4.21 \cdot 10^4$	$1.30 \cdot 10^4$
2.4	$1.29 \cdot 10^4$	$4.35 \cdot 10^3$

Table 2.1: The table shows the mass absorption coeffcients κ in cm^2g^{-1} of carbon and of iron. The wavelength λ is given in nanometer. Data taken from Henke et al. (1993).

describe how electrons of low energy (around $200\,eV$ and less) can interact with matter and distribute their energy.

Low Energy Photons Low energy photons with $E \lesssim 10\,eV$ have sufficient energy to break the chemical bonds in AC and HAC (Table 2.3).

Medium Energy Photons In the energy range $10\,eV \leq E \ll 288\,eV$ the photons are able to expel the electrons from both the $2s$ and $2p$-shell of the carbon atom. The electrons leave the atom with a kinetic energy roughly equal to the difference of the binding energy (Table 2.4) and the energy of the incident photon. The binding energy varies somewhat with its chemical environment, known as chemical shift in the field of photo-electron spectroscopy, according to Hüfner (2003). Soft X-rays and extreme ultra-violet photons are able to double-ionize carbon (Aresu et al., 2011).

High Energy Photons Photons with an energy higher than 288eV are able to expel electrons from $1s$. The emitted electrons posses a kinetic energy equal to the difference between the incident photon and their binding energy (Table 2.4).

Emission of Photons of Higher Energy When an electron is expelled from its atom, it leaves a vacancy in its original shell. This vacancy is filled by an electron from an outer shell that plummets into the vacancy. By filling the vacancy with a higher-level electron, the atoms assumes a less energetic level and emits a photon. Its energy is the difference of the binding energy of the vacancy and the electron moving there. The photons emitted from a carbon atom having one of its electrons removed, have an energy of roughly $270\,eV$ for a $2s$ or $2p$-electron plummeting into $1s$.

Penetration depths of different materials

in nm, numbers in parentheses correspond to VUV-irradiated samples

E_{phot} $[eV]$	ν_{phot} $[\mu m^{-1}]$	λ_{phot} $[nm]$	**AC**	**HAC**	**FeAC**	**FeHAC**
7.5	6	167	140 (50)	196 (68)	11 (4)	2 (1)
9.5	7.5	130	89 (31)	143 (48)	8 (3)	2 (1)

			Carbon	**Iron**
10.2	8	121	15	12
21.2	17	58	7	11
30.5	25	40	14	16
49.3	40	25	43	32
511	400	2.5	340	294

Table 2.2: This table shows the penetration depth for the materials analyzed in this thesis. The values for the range $\lambda > 120\,nm$ were derived from the measurements in this thesis. The other values were derived from the data of Henke et al. (1993). The huge variations between $9.5\,eV$ and $10.2\,eV$ are mainly due to differently-chosen densities. For AC, HAC and FeAC as well as FeHAC the established densities of around $1.7\,gcm^{-3}$ were used. Furthermore, photons of $10\,eV$ can still be absorbed by molecular bonds. Therefore the choice of the reference material plays a huge role for lower energies. Since the bonding situation becomes less and less important the higher the photon energies become, the values of the pure materials were chosen.

Bond	$H-C$	$C-C$	$C=C$	$C\equiv C$	$C=O$
Energy in eV	4.3	3.6	6.4	8.7	7.8

Table 2.3: Bond dissociation energies according to Neufingerl (2006) and converted into electron-volts per bond.

Auger Electrons When high level electrons fill the vacancies of shells close to the core, the emitted photons can expel electrons from other outer shells. This effect is known as Auger effect. If an electron of carbon's $2s$ or $2p$ plummets into a vacant $1s$, the emitted photon is able to expel $2s$ or $2p$-electrons from the same atom. The energy of the photon is fully absorbed by this ejected, secondary electron. Carette et al. (1977) write that the Auger yield typically dominates over the fluorescence yield.

Electron	**Binding Energy in eV**
1s	288.23
2s	16.59
2p	11.26

Table 2.4: Binding energies of the carbon atom. Taken from Thomas (1997).

Inverse Photoemission The inverse photoemission is, in simple terms, the time-reverse of the photoelectric effect. An electron of energies comparable to the electron transitions in a solid enters the solid and emits a photon while it occupies an unoccupied state. The energy of the emitted photon is the sum of the kinetic energy of the electron and the binding energy of the now occupied state. As Dose (1983) states, the probability of the inverse photo-emission is several order of magnitude small than its counter-part, the photo-electric effect.

Electron Collision As was shown for the first time in the Franck-Hertz-experiment (Franck and Hertz, 1914), electrons colliding with atoms can transfer their kinetic energy unto bound electrons and excite them. However, this is only possible for well-defined energies. Upon relaxation the electron emits a photon according to the energy difference of the levels it occupied.

Electrons also emit photons when they are moving towards an atom. When they experience a Coulomb field, e.g. by spontaneously induced dipole moments, they are decelerated. The change of velocity causes the electron to emit a photon accordingly. (Carette et al., 1977)

Interaction of Photons and Electrons with Carbonaceous Matter

In this section we will briefly cover some well-observed and well-understood interactions of photons and electrons with carbonaceous matter, i.e. organic compounds and graphite.

Dehydrogenation Hydrogenated amorphous matter or hydrocarbons in general can be dehydrogenated by photons of suitable energy (Dupuy, 1975; Gadallah et al., 2012) and electrons (Damany et al., 1974; Dupuy, 1975) and annealing (Mennella et al., 1995; Blanco et al., 1993).

In Damany et al. (1974) it is shown how, for example, methane reacts to different incident photons:

$$E \leq 12\,eV \quad CH_4 + h\nu \rightarrow CH_4^+ + e^- \tag{2.5}$$

$$E \sim 13.5\,eV \quad CH_4 + h\nu \rightarrow CH_3^+ + H^- \tag{2.6}$$

$$E \sim 14.3\,eV \quad CH_4 + h\nu \rightarrow CH_3^+ + H + e^- \tag{2.7}$$

$$E \sim 15.2\,eV \quad CH_4 + h\nu \rightarrow CH_2^+ + H_2 + e^- \tag{2.8}$$

Polymerisation Polymerisation is a consequence of dehydrogenation, which leaves a carbon atom with a free electron. The electrons are capable of forming bonds with unbound electrons of atoms nearby. Thus, two adjacent hydrogen-bearing structures may lose hydrogen and form a bond with the available electrons. (Dupuy, 1975)

Graphitization Graphitization is quite often a direct consequence of dehydrogenation and a special case of polymerisation, where aromatic structures are formed.
In the UV-spectrum graphitization can be recognized as an increase of the $\pi \rightarrow \pi^{\star}$-transition band. Gadallah et al. (2011) showed that graphitization takes place under UV-irradiation, as well as thermal annealing (Gadallah et al., 2013). Even proton bombardment of carbon under an ice-layer with much higher energies can lead to graphitization as Sabri et al. (2015) have shown. How ever this might have been due to annealing effects, because the protons can trigger exothermic chemical reactions between the ice and the carbon.

Scission Hydrogen is removed from the carbon atoms by breaking their bonds to these atoms. Similarly, photons and electrons are capable of breaking σ- and π-bonds. This is of particular interest if a σ-bond that solely connects two bigger structures, breaks. This can lead to the scission of a structure, if there is no immediate recombination. (Dupuy, 1975)

2.2.3 Previous Processing Experiments of Carbonaceous Materials

In this section I want to give a short and incomplete overview over previously-performed irradiation experiments with both photons and electrons.

Ugarte (1993) exposed amorphous carbon to an electron beam and observed the formation of carbon onions. He described that upon irradiation the graphitic substructures broke apart and disorder increases, but within a few ten seconds of processing the order of the graphene layers increased to form onion-like fullerenes.

In 1996 Mennella et al. (1996) were among the first to investigate the UV-spectrum of UV-irradiated hydrogenated carbonaceous materials. They found that upon irradiation with a hydrogen discharge lamp a band around $215\,nm \pm 2\,nm$ emerged (Figure 2.4). Later on, Gadallah et al. (2011) performed a similar experiment where he irradiated hydrogenated and non-hydrogenated amorphous carbonaceous materials. He investigated the spectral range from the VUV to IR and its morphology too. He found a band emerging at around $217\,nm$ (Figure 2.3). Furthermore he observed graphitisation and dehydrogenation. Dartois

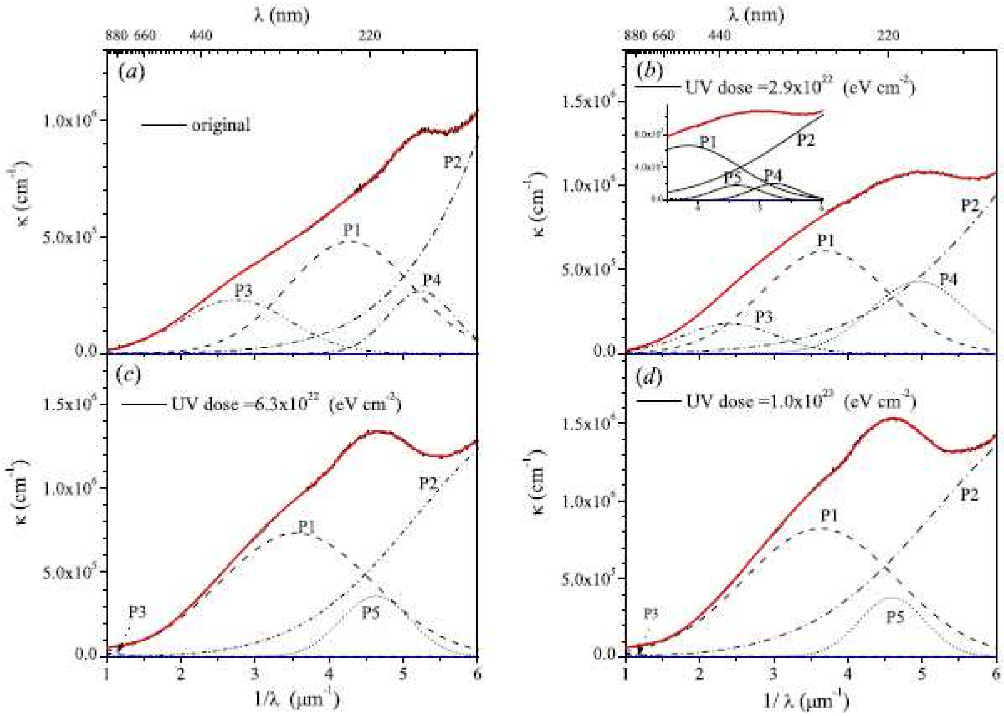

Figure 2.3: The figure shows the result of Gadallah's processing experiments with a deuterium lamp. The abscissa shows the wavenumber in μm^{-1}, the ordinate shows the mass absorption coefficient in $cm^2 g^{-1}$. Using DUV-irradiation he gave rise to a band at $4.6\,\mu m^{-1}$. Taken from Gadallah et al. (2011).

et al. (2004) irradiated solid methane to find that the substance partially dehydrogenated and formed a network of aliphatic and aromatic sites.

Miyajima et al. (2008) treated their amorphous carbon with photons in the VIS and NIR range. They found that their material increased its sp^2-content, meaning it graphitized. Henley et al. (2008) irradiated multi-walled carbon nanotubes with photons of $5\,eV$ from a pulsed laser and observed that the nanotubes were damaged and their distinctive absorption band vanished. Narayan and Bhaumik (2015) irradiated amorphous carbon with nanosecond pulses, too, and found that their material formed nano-diamonds. Again, the high doses disrupted the sp^2-sites and changed their bonding situation to sp^3 carbon.

2.3 Analytical Methods

In this section, a brief introduction to the analytical methods employed to investigate the samples, shall be given. The first two subsections deal with the topic of spectroscopy. Firstly, the general concept of absorption will be presented, based

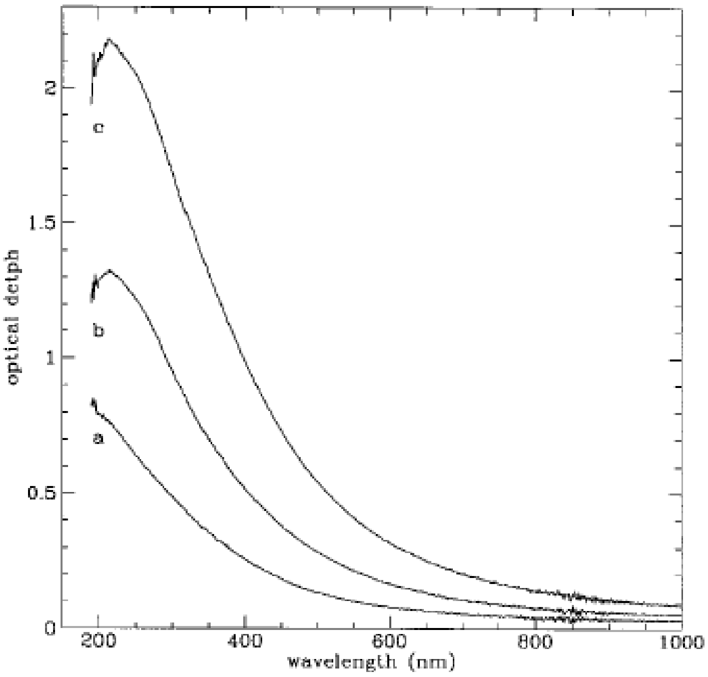

Figure 2.4: The figure shows the result of Mennella's processing experiments with a hydrogen lamp. Using HUV-irradiation he gave rise to a band at 215 nm. Curve a shows the untreated sample, b shows the sample after a dose of $10^{22}\,eVcm^{-2}$ and c after $4 \cdot 10^{22}\,eVcm^{-2}$. Taken from Mennella et al. (1996).

on Bohren and Huffman (2004). Hence, the techniques to measure and determine the absorption, i.e. spectroscopy, are presented — along with the mechanisms that cause absorption. From there, I present another way of investigating the electronic and bonding situation in materials: NEXAFS.

We then proceed to the imaging techniques, the high resolution transmission electron microscopy (HRTEM) to conclude this subsection.

Along with the fundamentals of the techniques, there is each a subsection that discusses the technical details of the analysis and interpretation of the measurements.

2.3.1 Mass Absorption Coefficient

When electromagnetic waves propagate through a medium, they experience both a change in their propagation velocity and their intensity. When electromagnetic waves with an initial intensity of I_0 travel through a medium of the thickness x, they loose energy. The remaining intensity of the photons decreases to $I(x)$. The initial and final intensities are related by the transmission T:

$$T(x) = \frac{I(x)}{I_0} \Leftrightarrow I(x) = I_0 \cdot T(x) \tag{2.9}$$

The transmission depends on both the medium the photons traverse and the length of the path they travel through the medium. This is reflected in

$$I(x) = I_0 \cdot \exp(-\alpha x) \tag{2.10}$$

$$T(x) = \frac{I(x)}{I_0} = \exp(-\alpha x) \tag{2.11}$$

Here, x is the path length in the medium and α is the material-specific extinction coefficient. Furthermore, α is also wavelength-dependent. This results in

$$\alpha \cdot x = -\ln T \tag{2.12}$$

This extinction coefficient α relies on two primary effects: absorption α_{abs} and scattering α_{sca}. The absorption is independent of the size of the particles the photons encounter. Yet, the scattering contribution depends on the sizes of the particles. Both quantities are, however, wavelength-dependent. Llamas-Jansa (2006) did scattering simulations of carbonaceous materials and concluded that for particles up to $20\,nm$ in size the scattering only contributes up to 6% of the extinction in the UV/VIS/VUV-range. Since the particles which were produced for this thesis were in the same range, the scattering contribution is neglected, and I set $\alpha = \alpha_{abs}$.

A quantity derived from the absorption coefficient is the mass absorption coefficient κ. The mass absorption coefficient is defined as $\kappa = \alpha/\rho$. Here, ρ is the density of the medium the electromagnetic wave traverses. Thus Equation 2.10 is transformed into

$$I(x) = I_0 \exp(-\kappa\sigma(x)) \tag{2.13}$$

$$\sigma(x) = \rho \cdot x \tag{2.14}$$

Here, $\sigma(x)$ denotes the column density, i.e. mass per area of a slab of material with the density ρ and the thickness x.

2.3.2 UV/VIS- and VUV-Spectroscopy

UV/VIS-spectroscopy and VUV-spectroscopy are used to gather information about the electronic structure of a material by exciting electronic transitions between bonds.

For the UV/VIS-spectroscopy a Perkin-Elmer *Lambda 19* spectrometer was used. For the VUV-spectroscopy a VUV-spectrometer by the Laserzentrum Hannover was used.

Bonds

When atoms bind to form molecules, the first bond to form is the σ-bond, the second and third one, if they exist, are π-bonds. The electrons of a σ-bond are distributed symmetrically around the axis between both atoms involved. They can be formed by overlapping s-orbitals or any other (hybrid-)orbitals which are symmetric around the axis between both atoms. The electrons for a π-bond are contributed from p- or sp^x-hybrid orbitals. π-bonds are formed between orbitals that are oriented perpendicular to the axis connecting both atoms. The n- or non-binding orbitals are occupied by electrons that are not involved in any bond whatsoever. For every binding orbit (except for n), there exists another orbital that, if occupied, counter-acts the bond, so-called anti-bonding orbitals. These orbitals are named according to their binding counter-parts, but are denoted by a superscript star e.g. $\sigma^\star$. The values have been taken from (Chemistry), unless noted otherwise.

There are four electronic transitions of carbon that are of particular interest. These are graphically illustrated in Figure 2.5

- $\sigma \rightarrow \sigma^\star$: $60\,nm < \lambda < 100\,nm$ (Jäger, 1999)
- $\pi \rightarrow \pi^\star$: $180\,nm < \lambda < 260\,nm$ (Jäger, 1999)
- $n \rightarrow \pi^\star$: $200\,nm < \lambda < 700\,nm$
- $n \rightarrow \sigma^\star$: $150\,nm < \lambda < 250\,nm$

The electrons of the binding orbitals and the non-binding orbitals can absorb energy and can be excited into one of the higher states. Non-binding electrons can be excited into any orbital, the binding ones can only be excited into their anti-binding counter-part.

UV/VIS- and VUV-spectroscopy measures these transitions. Hence, one can determine which kind of bonds exists within a sample and thus conclude whether chemical reactions have taken place, or distinguish the allotropes of a material, as all the transitions are broad but specific.

Furthermore, some carbonaceous samples do show a band at around $3\,\mu m^{-1}$ which is attributed to plasmons of large graphene layers by Jäger et al. (2008b).

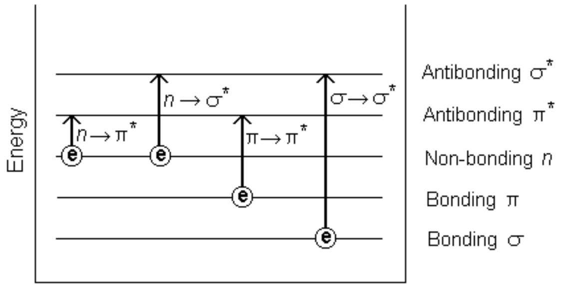

Figure 2.5: The graphic illustrates the electronic transitions that are found in carbon-based compounds. Taken from Chemistry.

Ambient Contaminants

Whenever the amorphous carbonaceous samples are exposed to air, they adsorb mostly water and oxygen from the air due to their porous and fluffy structure which has an enormous surface. Both water and oxygen can be detected easily in the IR. Adsorbed water shows bands around $3300\,cm^{-1}$ (NIST:Water) and oxygen bound to carbon has an absorption band around $1720\,cm^{-1}$ (Jäger, 1999) in the IR. In the UV-region the features are not very distinct. However, in some samples there appears a band with a relatively stable position around $5.23\,\mu m^{-1}$.

Deconvolution

Deconvolution is the process of unfolding a data set into its basal components, i.e. $\pi \rightarrow \pi^\star$- and $\sigma \rightarrow \sigma^\star$-transition bands. An example is shown in Figure 2.6. Since that task is not trivial, a custom programme has been written with SCILAB to ensure physically reasonable fitting.

The output of the fitting routine is the central wavenumber and FWHM for every basal component. Furthermore, it yields the amplitude of every basal component in relation to the normalized spectrum. The programme normalizes the data point with the highest absorption value of the spectrum of the unirradiated sample to 1. The same scaling factor is applied to the spectrum of the irradiated sample.

Due to the statistical and random nature of amorphous carbonaceous materials, the bands are considered to be of Gaussian shape. However, as the spectral range covers only the nearest infrared, visible and UV down to roughly 120nm, the deconvolution is somewhat ambiguous. The deconvolution process used here, consists of two sub-processes. The first part consists of a Monte-Carlo-method (MCM): Some ten to a hundred thousand sets of parameters consisting of central positions, widths and amplitudes are generated by a somewhat intelligent random number-generator: For each set the central wavenumbers are chosen at random

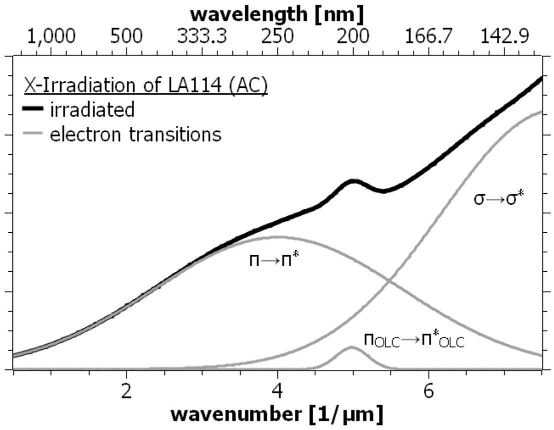

Figure 2.6: The plot shows the deconvoluted spectrum of the irradiated sample LA114 (AC, X). The basal components are plotted in grey. They are labeled with their kind of transition.

within specified limits. The programme then goes through the spectrum from long to short wavelengths, as the data in the red part of the spectrum leave less ambiguities for interpretation than in the blue part. Each band is then assembled step by step. First a reasonable amplitude is determined by the programme computing the difference between the target spectrum and the current, incomplete fit (residual spectrum) at the current central wavelength. This amplitude is then decreased by up to 20 percent. Thereupon the FWHM is determined from the residual spectrum by looking into the red direction and finding the first wavenumber where the value is half of the chosen amplitude. The thus created band is added to the incomplete fit and the processes repeated until all $n = 3 \ldots 5$ bands are added.

This method always leads to FWHMs that are too wide. If the Monte-Carlo-algorithm were the only process of this routine, randomly decreasing the FWHM as well is necessary to yield better fits. However, the amount of sets evaluated is by far too small to find a presentable fit. In order to take care of that, a second process follows the MCM. After the evaluation of all sets, the ten best sets are chosen and further processed by a hill descent or downhill simplex. The parameters were always varied in the same order. If the spectra were more complicated, the order of variation during each run should be varied randomly, to minimize the chance of being stuck at a local minimum. However, doing a descent on ten shots was in most cases sufficient to yield several physically reasonable fits. An example of the output for a sample can be seen in Figure A.1.

As most samples experienced the emergence of other bands, the number of bands to be fitted was increased by one for the processed samples. Here, two approaches were taken. As a bottom-up approach the entire routine was repeated with one more band, set at $5\,\mu m^{-1}$. The second approach used the ten finished sets of parameters that the whole routine produced for the unirradiated sample, as initial sets and added another narrow band at $5\,\mu m^{-1}$. These sets were then re-processed by the hill descent.

The bottom-up sets were less unambiguous than the ones created from the unprocessed samples. The latter ones tended to show continuity to a certain degree. However, for samples whose pre- and post-irradiation spectra differed enormously, the bottom-up approach yielded better results.

The choice of the band shape might cause errors and additional physically unreasonable bands. However, mixtures of Lorenzian and Gaussian Curves as in Equation 2.15 were considered, but having adding another parameter might deliver problems in other places and increases computation time.

$$S_{\nu_0}^{x}(\nu) = x \cdot A \exp\left(-\frac{4\ln 2 \cdot (\nu - \nu_0)^2}{FWHM^2}\right) + \frac{(1-x)\cdot A}{1 + \frac{4(\nu-\nu_0)^2}{FWHM^2}} \quad x \in [0,1] \tag{2.15}$$

As the spectra cover only the range from $0.5\,\mu m^{-1}$ to $7.5\,\mu m^{-1}$, the deconvolution becomes more ambiguous for bands in the blue part of the spectrum. The typical center of the $\sigma \rightarrow \sigma^{\star}$, usually around $9\,\mu m^{-1}$, lies outside of the recorded spectra. Thus, theoretically, this transition band could be fitted to any wavelength around $9\,\mu m^{-1}$, only the FWHM and amplitude would need to be adjusted. The programme chooses any suitable set of parameters that minimize the difference between the targeted and fitted spectrum. Thus, we cannot derive any solid statements about the $\sigma \rightarrow \sigma^{\star}$-band.

The deconvolution sometimes yields a band around $6\,\mu m^{-1}$, that cannot be assigned to any physically reasonable transition. This band is an artefact that might be caused by the wide reach of a band around $20\,\mu m^{-1}$ (Gavilan et al., 2016). Similar to the lack of knowledge about the $\sigma \rightarrow \sigma^{\star}$ transition, the even greater lack of information about this band, makes it very difficult to determine the parameters of this band. Any attempt to define this band for the deconvolution has a great effect on the $\sigma \rightarrow \sigma^{\star}$ transition. Its effect on the $\pi \rightarrow \pi^{\star}$-transition is less significant, as the red flank of this artefact band might coincide with the red flank of the $20\,\mu m^{-1}$-band. However, the blue flank of the artefact band does not coincide with the red flank of the huge band, and necessarily leads to a red-shift of the $\sigma \rightarrow \sigma^{\star}$, or an increased width or amplitude. What happens exactly, we cannot tell, as the parameters for the $\sigma \rightarrow \sigma^{\star}$-band are already somewhat arbitrary. In other instances a band around $6\,\mu m^{-1}$ might just be a compensate for an inappropriately chosen σ-band.

Whenever another physically unreasonable band appears, mostly in the red parts of the spectra, being shallow and broad, it can be explained in so far, as a Lorenzian curve might have been a better choice than the Gaussian one.

But apparently there is no scientific consensus on what kind of function to choose: Gavilan et al. (2016) uses a Lorenzian curve for the reddest band only and Gaussians for the others, Gadallah (2010) only used Lorenzian curves, Llamas-Jansa (2006) only used Gaussian curves. I have decided in favour of Gaussian curves, to avoid additional fit parameters that would require an explanation about the distribution of distribution functions.

Another practical problem arises with the samples themselves: Whenever the penetration depth of the irradiating photons is significantly smaller than the sample thickness, the spectral features of processed and unprocessed or differently processed areas of the sample overlap and merge into broad bands.

2.3.3 NEXAFS

NEXAFS — near edge X-ray absorption fine structure — is another useful technique for the investigation of the bonds in matter. This spectroscopic technique employs X-rays in the energy range around the absorption edges of a certain material. An incident photon interacts with one of the electrons close to the core and, if the energy is sufficient, ejects it. This is seen as the absorption edge.

In VUV-spectroscopy binding electrons are excited into anti-binding orbitals by absorbing the incident photons. In the case of NEXAFS something similar happens: electrons from close to the core are excited into anti-bonding orbitals. NEXAFS does not use transmission measurements, but the emission of secondary electrons. When the core-electrons are excited into an anti-bonding orbital, they create a vacancy that is immediately filled by another electron from an outer shell. By plummeting, the electrons release photons which in turn eject the outer electrons. This current can be measured and is directly proportional to the absorbance. The absorption edge itself is not relevant for the interpretation and needs to subtracted. The resulting spectrum shows the fine structure of the transitions from the core-electrons to the anti-binding orbitals.

The probing depth of NEXAFS is usually around $10\,nm$ (Kovačević et al., 2009).

NEXAFS is frequently employed to compute the sp^2-content of carbonaceous materials.Narayan and Scholvin (2005) propose the following method:

$$\frac{(I_\pi/I_\sigma)_s}{(I_\pi/I_\sigma)_r} = \frac{3x}{4-x} \tag{2.16}$$

Here, x is the atomic fraction of sp^2-carbon. I_π denotes the area of all π-related bands between roughly $284 - 289\,eV$, I_σ denotes the area of the σ-related bands between $290\,eV$ and $305\,eV$. The index r refers to a reference material whose sp^2-content is one hundred percent, s refers to the sample to be investigated.

But as long as there is no proper NEXAFS measurement of a material consisting of 100% sp^2-hybridized carbon, Equation 2.16 cannot be applied correctly, as Jäger (1999) stated. In this thesis I will use a simpler approach. The ratio of the areas of the sp^2- and sp^3-related bands will be compared directly to the ratio of a sample with known sp^2/sp^3-ratio.

The spectra $S(E)$ of the electron yield were deconvoluted with the following formula

$$S(E) = Step(E) + \sum_i G_i(E) \tag{2.17}$$

$$Step(E) = \frac{k}{2}\left(\frac{2}{\pi}\arctan\left(f(E - E_0)\right) + 1\right) + h - \alpha E \cdot \Theta(E - E_0) \tag{2.18}$$

$$G_i(E) = \frac{a_i}{1 + \gamma_i \left(E - E_{0,i}\right)^2} \vee a_i \exp\left(-\gamma \left(E - E_{0,i}\right)^2\right) \tag{2.19}$$

The term $\frac{k}{2}\left(\frac{2}{\pi}\arctan\left(f(E - E_0)\right) + 1\right) + h$ represents the step function, whose centre E_0 was fixed to $E_0 = 290\,eV$. f characterizes the sharpness of the step, k is the step size and h is its offset.

The term $-\alpha E \cdot \Theta(E - E_0)$ denotes the decrease after the step, α is the decrease ratio and $\Theta(x)$ is the Heaviside-function which is 1 for $x > 0$ and zero otherwise.

As for the bands $\sum_i G_i(E)$, the fits used both Gaussian and Lorentzian curves — whichever matched best. In any case, $E_{0,i}$ denotes the central energy of the band, a_i is its respective strength and γ is a measure for the band's FWHM. The proper choice of the step-function is crucial. Any band in the proximity of the step depends highly on whether it is supported by the step or based on the zero-line, as its position relative to the step can alter its integral strength by a factor of roughly 2. As already mentioned, the step was centred around $290.0\,eV$. The slope was determined by matching it with the spectrum's slope at $320\,eV$ to $330\,eV$. For the fitting itself two slightly different techniques were applied:

For the samples measured by Dr. Kovacevic, a MCM was used to find proper start parameters. The process is similar, but uses fewer heuristics, to the one applied for the UV-spectra. Out of 300,000 sets, the seven best were chosen. These were then cloned with deliberate errors, i.e. some bands were randomly removed, and added to the seven ones chosen. These 28 spectra then underwent downhill simplex procedures. Finally, the most reasonable deconvolutions were kept.

For the reference spectra an initial manual fit was done by mimicking the semi-intelligent MCM applied to the UV-spectra. At this point the parameters of the NEXAFS spectrum were practically fully determined. In order to keep the parameters and simultaneously improve the fit, another MCM was applied instead of a gradient descent. The MCM searched a confined parameter space around the manually-found parameters.

2.3.4 High Resolution Transmission Electron Microscopy

High resolution transmission electron microscopy (HRTEM) is an imaging technique employed to view structures on a nanometer scale. It is able to resolve samples at a resolution of less than an Ångström.

Unlike other types of microscopy or spectroscopy, HRTEM does not produce images based on absorption or the topology of a sample's surface or its atomic composition. The HRTEM uses phase contrasts. When a nearly plane electron wave propagates through a medium it is subject to scattering and absorption. This results in both an amplitude contrast as well as phase contrast. For the HRTEM the phase contrast is the more important one. This phase contrast is, however, disturbed by imperfections of the optical system and the roughness of the investigated sample. In order to overcome these problems, the samples are usually investigated with a slightly defocused electron beam, e.g. using the Scherzer focus. The image is then reconstructed by having the electron wave interfere with an undisturbed electron wave. The interference pattern is then turned into a comprehensible image via Fourier transformation. (Reimer and Kohl, 2008) Graphene layers are usually observable as black lines in electron microscopy images (Wang, 2000).

Interpretation of HRTEM Images

Since the materials present were mostly carbon and to a lesser extent hydrogen and iron, the images can be understood as mostly topographical.

In order to characterize the samples three parameters were chosen to characterize the samples: fiber length, curvature and complexity. To derive numerical indices for these quantities, the structures had to be separated and collected numerically. As a first attempt, a programme was written to automatically cluster and analyze the structure. This programme used information on the contrast to find the paths representing the graphitic layers and separate them. Each layer was then represented by a collection of 2D data points. Another sub-programme

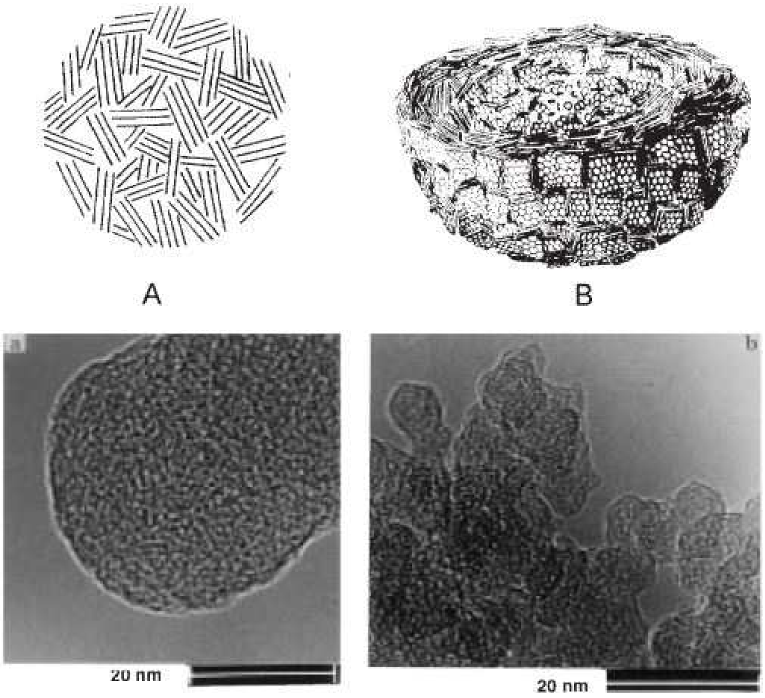

Figure 2.7: The left hand side *A* shows carbon grains consisting of unoriented graphitic nanocrystals, the right hand side shows concentrically oriented carbon layers in a onion-like grain. The upper row shows schematic illustrations, the lower one shows corresponding HRTEM-images. Taken from Henning and Salama (1998).

then vectorized each list of data points using a blend of genetic and evolutionary algorithms. Thus, the original path, whose width was several pixels, could be transformed into a one pixel-wide and ordered path. In theory and with some carefully chosen images, the programme worked well and reliably, but the computation time was enormous. Furthermore, the contrast of most of the images could not be adjusted sufficiently well to allow the programme to run properly. Hence, it was decided to trace all structures manually. This of course is a source for selection bias, as clear and unobstructed structures were naturally preferred by the selector. However, the selection of structures, hence called paths, is still a good measure for tendencies.

The paths are collections of data points. Using a polygonal approach their length was determined. But one runs into problems here: Partially obscured paths cannot be traced in their full length. Other structures might, due to post-processing of the images, appear to be split into several paths. Whenever it seemed reasonable, such paths were connected. Furthermore, upon irradiation the structures became more inter-connected. Hence single paths could not be determined, but sub-structures were chosen instead. Thus all statements on the fiber-length should be viewed in the light of being sub-structures rather. Furthermore, the average lengths of the chosen paths of an analyzed area is higher than the actual average length of the layers there due to the selection bias for longer paths.

The curvature, defined as the reciprocal of a radius, of the paths was computed by fitting a circle to every consecutive set of four data points and averaging the resulting curvatures. The complexity was defined as the standard deviation of the curvature within each path. Thus the complexity is able to distinguish between primitives, like circular arcs and straight lines, and anything else.

As an additional quantity describing the material, the straight to bent-ratio was defined as the ratio of bent structures, like circles and everything irregular, to rather straight paths.

Chapter 3

Experiments

3.1 Targets

Two kinds of targets have been used. For the iron-free samples commercial graphite pellets have been used, which had been made of cut graphite electrodes.

For the iron-containing samples, graphite powder with a grain size of less than 20 micron was mixed with iron powder with a grain size of less than 10 microns. The powders were blended in a planetary mill for thirty minutes and then pressed into a pellet. Two different blends were used, one with an atomic ratio of $C/Fe = 15/1$ and one with $C/Fe = 5/1$. Whenever the ratio is of importance, the ratio will be appended to the material name as 5 or 15 respectively.

3.2 Sample Production

All of the samples were produced with the laser ablation set-up as described in section 2.1. The parameters for the production of the different samples are listed in Table 3.1.

All of the samples, except for the ones for NEXAFS, were deposited on CaF_2-substrates.

3.3 Carbon-Iron Grains

The original intent for the incorporation of iron was the idea that carbon onions with an iron-core might be a suitable candidate for the 217 nm interstellar extinction bump.

First attempts to incorporate iron were made with small powdered iron oxalate mixed with carbon powder. Atomic ratios for iron to carbon of 1:1000 and 1:100

species		atmosphere	laser power
amorphous carbon	**AC**	$8-10\,Torr\ He$	$1\,W$
hydrogenated amorphous carbon	**HAC**	$4-6\,Torr\ He : H_2$ (5:0.5 - 5:3)	$0.5\,W$
iron-containing amorphous carbon	**FeAC**	$8-10\,Torr\ He$	$1\,W$
iron-containing hydrogenated amorphous carbon	**FeHAC**	$4-6\,Torr\ He : H_2$ (5:0.5 - 5:3)	$0.5\,W$

Table 3.1: The table displays the parameters used for the laser-ablation-based production of the samples. Even though the values vary a bit, it did not have a significant effect on the deposits.

were tried initially. The HRTEM images did not show any iron inclusions. For reasons of safety, as the ablation of oxalate with carbon might create carbon monoxide, no higher ratios of iron oxalate were used. Thus, the attempts with iron oxalate were abandoned.

Another attempt was made with an iron-containing carbonaceous powder that had been produced by Dr. Alexandrescu of Bucarest by laser-pyrolytic decomposition of iron-pentacarbonyl. Due to the shortage of the material, attempts with this material, called FC14, were soon ceased.

Instead, iron-powder with a particle size of less than 10 micrometer was mixed with similarly small carbon powder.

The carbon and iron mixtures were ablated under both a helium atmosphere and a helium-hydrogen atmosphere.

The presence of iron in the samples was confirmed by HRTEM studies.

In order to estimate the final iron-content of the ablated samples, it was decided to measure their density, for HRTEM had already revealed that the major part of the iron does not chemically react with the carbon.

According to Equation 3.1

$$\nu = \frac{n_{AC}}{n_{Fe}} = \frac{1 - \frac{\rho_p}{\rho_{Fe}}}{\frac{\rho_p}{\rho_{AC}} - 1} \tag{3.1}$$

the iron-content can be estimated. The density ρ_{AC} denotes that of the carbon matrix surrounding the iron granules. ρ_p refers to the density of the iron-containing sample itself.

To get both densities, pure graphite targets and FeC15, respectively, were ablated under a helium atmosphere of 10 Torr. The material stuck on the skimmer, was brushed off and collected, and repeatedly handmilled with mortar and pestle, and

pressed to pellets at $2.5\,GPa$. Finally, their density was derived from the volume and mass of the pellets made. For the AC material, the density was computed as $\rho_{AC} = 1.16\,gcm^{-3}$, for the ablated FeC15 $\rho_p = 1.37\,gcm^{-3}$. Assuming that ρ_{AC} is the same in both samples, the initial ratio of the FeC15 pellet $\nu = 15$ increases to ≈ 20, meaning that the iron content decreased.
Since the density of iron is significantly higher than that of any carbonaceous material, it is less affected by the gas flow dragging the formed particles through the nozzle. Thus, this result seems quite reasonable.

3.4 Processing

The samples were processed in five different ways. In every case the samples were exposed to air prior to the irradiation processes. There the samples might be contaminated by the adsorption of molecules in the air, especially water. Due to the construction of the set-ups it was impossible to clean the samples by any other means than keeping them under vacuum prior to the processing for some hours.

3.4.1 ArF-Laser: 193nm

For what will be called ArF-irradiation or simply ArF respectively, an ArF-laser was employed. The samples were placed into a portable vacuum chamber on a sample holder with a piece of clean paper behind it. The chamber was then evacuated to below $10^{-5}\,mbar$, decoupled and sealed, and transferred to the laser. The laser irradiated the sample through a CaF_2-window. The laser emitted photons of $193\,nm$ at a rate of $200\,Hz$ and an energy per pulse of $2\,mJ$. The spot size was $3\,mm \times 6\,mm$.

The piece of paper darkened during the irradiation, thus the processed spot could easily be identified afterwards, as the sample itself did not change visibly under the processing. The samples irradiated with the ArF-laser, are shown in Table 3.2. The photon-output of the ArF-laser will hence be abbreviated as *ArF*.

Id	**Species**	**Dose** $[eVcm^{-2}]$	**Thickness** $[nm]$
LA9	FeAC	$6 \cdot 10^{22}$	7
LA10	FeAC	$16.0 \cdot 10^{22}$	10
LA14	FeHAC	$6.0 \cdot 10^{22}$	3
LA16	FeHAC	$9.4 \cdot 10^{22}$	3

Table 3.2: The samples irradiated with ArF at the Institut for Solid State Physics of the FSU Jena.

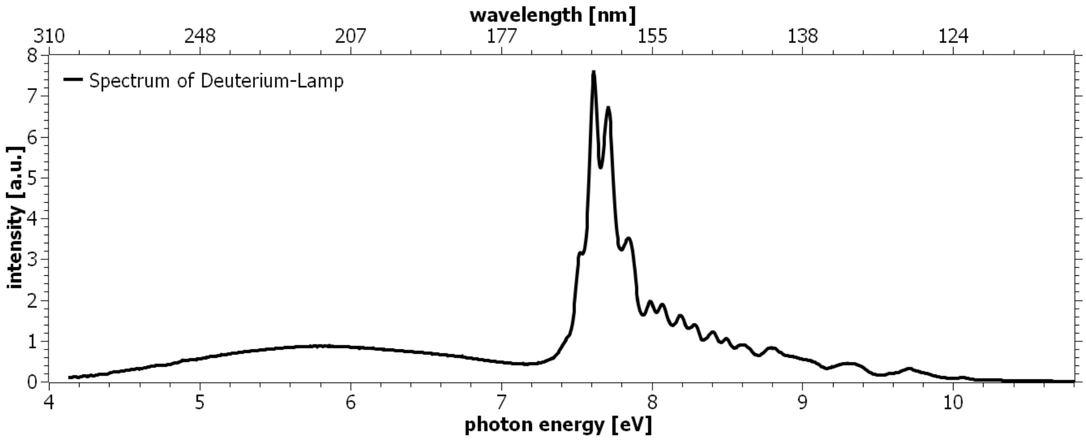

Figure 3.1: The graph shows the spectral distribution of the deuterium-lamp (DUV).

3.4.2 Deuterium Lamp: 167nm

For the DUV-irradiation, the deuterium-lamp of the VUV-spectrometer used for the analysis, was employed to process the samples. The output of the D_2-lamp is shown in Figure 3.1. The spectrum is dominated by a molecular transition $D_2(B \rightarrow X)$ (Benilan et al., 2011) at around $167\,nm$. In order to align the samples, the lamp was switched on under the ambient atmosphere. Although the higher energetic photons emitted by the deuterium lamp, can cause chemical reactions, the samples are not affected by being irradiated under ambient atmosphere, because all of the photons are absorbed by air and only the photons in the visible pass through to the sample. Still, the time of alignment was kept very short at around twenty seconds. The chamber where the sample was placed, was then immediately closed and evacuated. The pressure inside the chamber was kept below $10^{-5} mbar$. The spot of the lamp was around 1 or $2\,mm$ in diameter.

The photo-flux was determined by measuring the photo-current according to Fulvio et al. (2014). Instead of a gold substrate, both a copper and a platinum plate were used instead. The irradiated area was about $1\,mm^2$. The first irradiations were performed with the same lamp Kamel Gadallah used during his thesis. The then present energy of this lamp was fairly low and was subsequently replaced with a new one. The output of both his and the new lamp are shown in Table 3.3.

The function of the quantum yield $Y(E)$ of copper (Figure 3.2) can be approx-

	Gadallah's lamp		**new lamp**
years	2010	2014	2015-2017
Platinum	$3\,\mu A$	$0.255\,\mu A$	$0.89\,\mu A$
Copper	$(1.719\,\mu A)$	$0.146\,\mu A$	$0.510\,\mu A$

Table 3.3: The currents of the first lamp were measured by Gadallah with a platinum lid. Five years later the same lamp has been measured again, both with a platinum lid and a copper plate. The value in parentheses represents the photo-current Gadallah would have measured, if he had used a copper plate. The new lamp delivered almost a third of the energy the lamp used by Gadallah delivered.

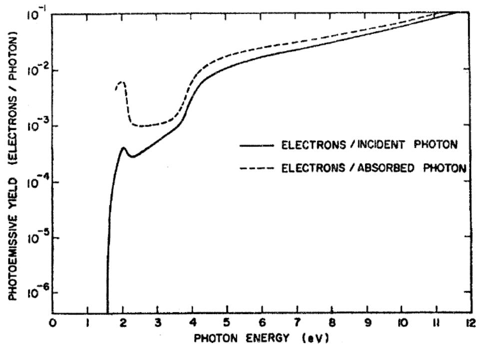

Figure 3.2: Quantum Yield of Copper. Taken from Berglund and Spicer (1964)

imated by

$$Y \approx 0.01 \cdot e^{(E-5\,eV)\frac{\ln 10}{7}} \quad E > 5\,eV \tag{3.2}$$

$$Y \approx 0 \quad E < 5\,eV \tag{3.3}$$

Multiplying the spectrum of the D_2-lamp (Figure 3.1) with the quantum yield, it yields a relative electron distribution. Integrating the distribution yields the relative photo-current, which, when scaled with the actual current, finally yields the actual photon distribution. Assuming a spot size of $1\,mm^2$, the total power delivered by the photons is about $4.135 \cdot 10^{20}\,eVcm^{-2}h^{-1}$ which is distributed in the different energy bands as presented in Table 3.4. The bands were chosen with respect to the different carbon-carbon bonds they can break. The A-band breaks any bond up to a triple bond, the B-band only breaks double and single bonds and the C-band only breaks single bonds.

During the measurement of the photo-current for the irradiation of LA39, the lamp yielded a current of $580\,nA$, thus its power increased to $4.7 \cdot 10^{20}\,eVcm^{-2}h^{-1}$. This is probably due to deuterium being released from the walls and especially from the metal parts inside the lamp.

The samples irradiated with the deuterium lamp are listed in Table 3.5. The photon-output of the deuterium-lamp will hence be abbreviated as DUV — deuterium-

	A-band	B-band	C-band
range	$E > 8.69\,eV$	$8.69\,eV > E > 6.36\,eV$	$E < 6.36\,eV$
	$\lambda < 142\,nm$	$142\,nm < \lambda < 195\,nm$	$\lambda > 195\,nm$
power	$3.1 \cdot 10^{19}$	$2.5 \cdot 10^{20}$	$1.3 \cdot 10^{20}$
fraction	7.5%	60.5%	31.5%

Table 3.4: The distribution of the photon and energy fluxes of the D_2-lamp in $eV cm^{-2} h^{-1}$).

Id	**Species**	**Dose** $[eV cm^{-2}]$	**Thickness** $[nm]$
LA25	FeAC5	$4 \cdot 10^{21}$	3
LA28	FeHAC5	$11 \cdot 10^{21}$	1.3
LA96	AC	$29 \cdot 10^{21}$	75
LA97	HAC	$24 \cdot 10^{21}$	70
LA98	FeAC	$31 \cdot 10^{21}$	14
LA99	FeHAC	$21 \cdot 10^{21}$	2
LA107	AC	$3.2 \cdot 10^{21}$	45
LA110	HAC	$40 \cdot 10^{21}$	351

Table 3.5: The samples irradiated with DUV at the Astrophysical Institute of the FSU Jena.

lamp UV-photons.

3.4.3 Hydrogen Lamp: 122nm

For the HUV-irradiation, an open-cylce hydrogen-lamp was employed (Warneck, 1962).

The irradiation took place in a small portable chamber. The chamber contained a retractable rod which carried both a copper plate and a gold-coated quartz plate to measure the photo-flux of the lamp.

The hydrogen lamp was run at a pressure of $0.6\,mbar$ identically to Fulvio et al. (2014). The hydrogen was excited by a microwave cavity at an input power of $100\,W$. After placing the sample inside the chamber, the evacuation started. Each sample had been kept in there for 16 hours before the irradiation started. Thereupon, the hydrogen lamp was started and the sample shielded from the irradiation with both the copper and gold plate to measure and adjust the flux. After the completion of the measurement, the photo-cathodes were retracted and the sample placed at the same position where the cathodes were priorly.

The photon-flux was measured according to Fulvio et al. (2014). But since there was no way of blocking one of the major bands, two materials, copper and gold, had to be used to determine the energy distribution by solving a set of two

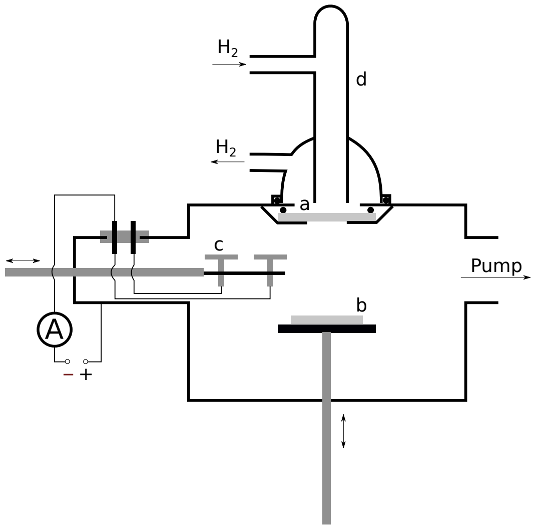

Figure 3.3: The image shows a sketch of the set-up used for the HUV-irradiation. a is an MgF_2-window, b is the sample on the sample holder, c are the two photo-cathodes and d is the hydrogen lamp.

equations (Equation 3.4 and Equation 3.5).

$$I_{Cu} = \Phi^{167} \cdot A_{Cu} \cdot Y^{167}_{Cu} + \Phi^{122} \cdot A_{Cu} \cdot Y^{122}_{Cu} \tag{3.4}$$

$$I_{Au} = \Phi^{167} \cdot A_{Au} \cdot Y^{167}_{Au} + \Phi^{122} \cdot A_{Au} \cdot Y^{122}_{Au} \tag{3.5}$$

This approach, however, was not viable as it requires a high accuracy for the quantum yield values. Uncertainties in the range of 20% proved to be a problem (Cairns and Samson, 1966; Fulvio et al., 2014; Mennella et al., 2006) .

According to Westley et al. (1995), 97% of the output of the hydrogen lamp is emitted as $Ly\alpha$ under the condition employed here, yet Fulvio et al. (2014) found that the amount of 160 nm photons was considerably higher. Still, we can determine the flux Φ as:

$$\Phi = \frac{I_{phot,metal}}{Y^{122nm}_{metal} \cdot A_{metal}} \tag{3.6}$$

Here, $I_{phot,metal}$ is the photo-current of the respective photo-cathode, Y^{122nm}_{metal} is the respective quantum efficiency at 122 nm, which is 0.055 for copper and 0.022 for gold. A_{metal} is the area of the respective photo-cathode. With an uncertainty of 20% for the quantum efficiencies, the flux of $L\alpha$ ranges between $\Phi_{Cu} = 3.5 \ldots 5.3 \cdot 10^{13}\, eVcm^{-2}s^{-1}$ and $\Phi_{Cu} = 1.8 \ldots 2.8 \cdot 10^{13}\, eVcm^{-2}s^{-1}$. We can therefore assume that the flux is $\Phi \approx 3 \cdot 10^{13}\, eVcm^{-2}s^{-1}$.

The samples irradiated with the hydrogen lamp are listed in Table 3.6. The photon-output of the hydrogen-lamp will hence be abbreviated as HUV — hydrogen-

Id	**Species**	**Dose** $[eVcm^{-2}]$	**Thickness** $[nm]$
LA116	AC	$1.05 \cdot 10^{17}$	18
LA117	AC	$2.1 \cdot 10^{17}$	17
LA103	FeAC	$0.53 \cdot 10^{17}$	8

Table 3.6: The samples irradiated with HUV at the Institute for Solid State Physics of the FSU Jena.

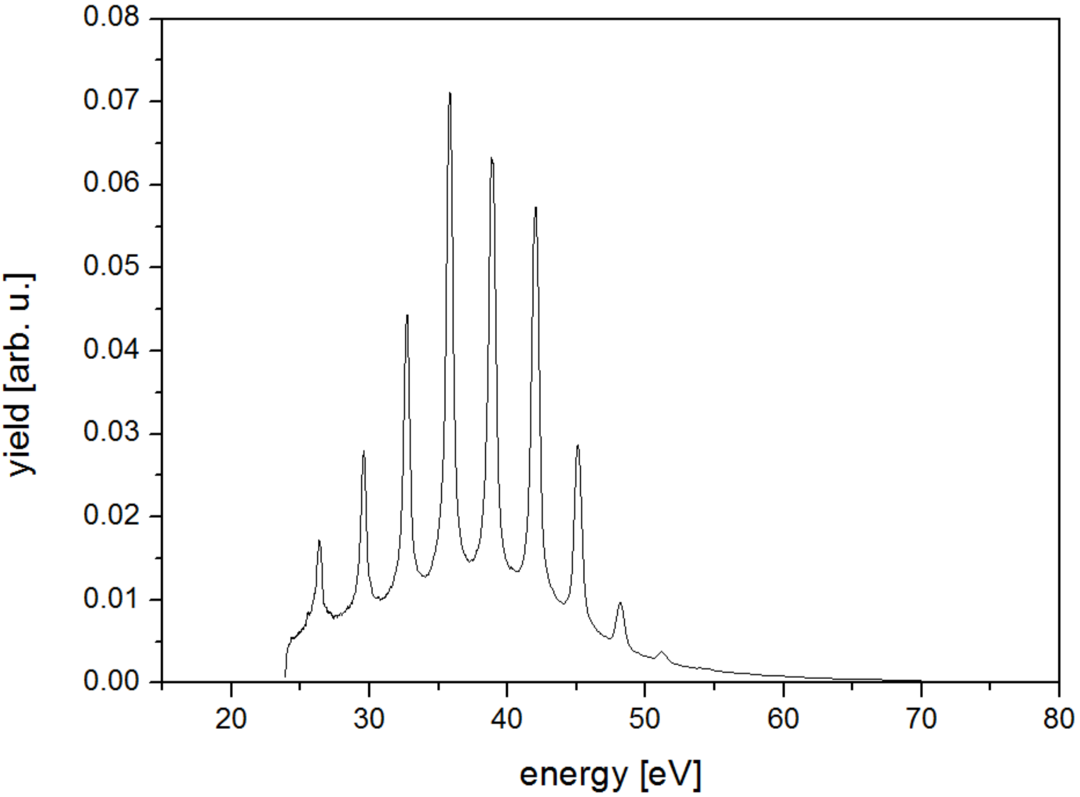

Figure 3.4: The graph shows the spectral distribution of the XUV-laser. The spectrum was provided by Dr. Michael Zürch.

lamp UV-photons.

3.4.4 Multi-Harmonics Laser: 90-30nm

For the XUV-irradiation, a multi-harmonics laser at the IOQ of the FSU Jena was used. The laser was operated by Dr. Michael Zürch and Frederik Tuitje under the supervision of Prof. Dr. Christian Spielmann.

The sample was placed inside a vacuum chamber and irradiated under a pressure of about $10^{-5}\,mbar$. The energy of the beam was measured every hour.

The multi-harmonic laser creates time-compressed pulses from the output of a continuous infrared-laser. The time-compressed pulses thus have a high intensity and interact with a medium where higher order processes take place creating photons of multiples of their original frequency. The output then passes through an aluminium filter to eliminate all photons of a wavelength longer than $87\,nm$ (Bohren and Huffman, 2004). A description of the basic processes can be found in Li et al. (1989).

Id	**Species**	**Dose** $[eV cm^{-2}]$	**Thickness** $[nm]$
LA43	FeHAC	$9.3 \cdot 10^{16}$	2.4
LA59	AC	$12 \cdot 10^{16}$	222
LA60	HAC	$81 \cdot 10^{16}$	85
LA63	AC	10^{16}	> 500
LA64	HAC	10^{16}	> 500
LA67	FeAC	10^{16}	> 500
LA102	FeAC	$25 \cdot 10^{16}$	17
LA104	FeHAC	$24 \cdot 10^{16}$	9
LA108	HAC	$37 \cdot 10^{16}$	135
LA115	AC	$3.4 \cdot 10^{19}$	17

Table 3.7: The samples irradiated with XUV at the Institute for Optics and Quantum Electronics of the FSU Jena.

The samples irradiated with the multi-harmonics laser are listed in Table 3.7. The photon-output, which is illustrated in Figure 3.4 of this laser will hence be abbreviated as *XUV* — extreme-UV (commonly abbreviated as EUV and XUV) photons.

3.4.5 Synchrotron: 2.5nm

The samples were irradiated at the SEXTANT beam-line at the synchrotron facility SOLEIL in France. The substrates with the carbonaceous deposits were cut to a suitable size, stuck to a sample holder and placed under vacuum, below $10^{-5}\,mbar$. During the course of several hours, the sample was irradiated by $500\,eV$ photons. On a rectangular area of $2\,mm \times 2\,mm$, a grid of small spots of $100\,\mu m \times 100\,\mu m$, spaced by $100\,\mu m$ in both dimensions, was irradiated.

Id	**Species**	**Dose** $[eV cm^{-2}]$	**Thickness** $[nm]$
LA112	HAC	$1.9 \cdot 10^{21}$	538
LA113	FeAC	$1.9 \cdot 10^{21}$	21
LA114	AC	$1.9 \cdot 10^{21}$	334

Table 3.8: The samples irradiated with $500\,eV$ at SOLEIL.

The samples irradiated with the synchrotron soft X-rays of $500\,eV$ are listed in Table 3.8. The photon-output of the synchrotron will hence be abbreviated as

X as in (soft) X-rays.

3.4.6 NEXAFS

In a collaboration with Dr. Eva Kovacevic, three samples were prepared and sent to her in order to have them irradiated at the BESSY synchrotron in Berlin and analyzed with NEXAFS.

The samples for the NEXAFS analysis were produced with laser-ablation, but deposited on gold-covered silicon substrates. In the case of LA23, laser-ablation-produced bulk material and one drop of the suspension was placed on the substrate.

The irradiation was done at the Berlin synchrotron with white light of an energy range from $2\,eV$ to $17000\,eV$. The irradiation lasted for 30 seconds and was performed under ultra high vacuum. Both the irradiations and the NEXAFS measurements were carried out by Dr. Eva Kovacevic.

Id	**Species**
LA23	FeAC
LA37	AC
LA38	HAC

Table 3.9: The samples irradiated with white light at BESSY.

The samples irradiated with the white light are listed in Table 3.9.

Chapter 4

Results

In this chapter I will present the experimental findings. This section starts with the results of the iron-incorporation. I will then cover the VUV/UV/VIS-spectroscopy of the irradiated samples. The samples are ordered according to the photon-energy with which they were irradiated starting with the lowest photon energy. This section concludes with the results of the NEXAFS measurements.

4.1 Carbon and Iron

In this small section, the incorporation of iron into carbonaceous materials is illuminated. I will focus on the morphological features of the thus-produced iron-carbon-particles and how they were formed. Next, I will give a brief account about how to control the features and sample composition coarsely. Finally, I will discuss the possibilities of deconvolving the spectra of iron-containing material.

4.1.1 Morphology of Iron-Containing Samples

Since laser-ablation is a high temperature process according to Jäger et al. (2008b) and easily reaches temperatures above $4000\,K$, both carbon and iron are easily evaporated. The average pressure in the laser ablation chamber is in the range of $5-13\,mbar$ $(4-10\,Torr)$. At such a pressure carbon would condense first at around $1700\,K$ followed by iron at roughly $1550\,K$. But because the generation of a plasma plume by means of a laser pulse is a non-equilibrium process, the local pressures in the plasma plume deviate. In fact, above $10\,mbar$ the condensation temperature of iron exceeds that of carbon. The carbon atoms are most likely present as small clusters of C_3 (Krasnokutski and Huisken, 2014) and larger clusters. Still, the small carbon grains can dissolve in the iron. Upon cooling, exsolution takes place (Nesse, 2000), forming several graphene layers around the iron (Figure 4.2,Figure 4.3).

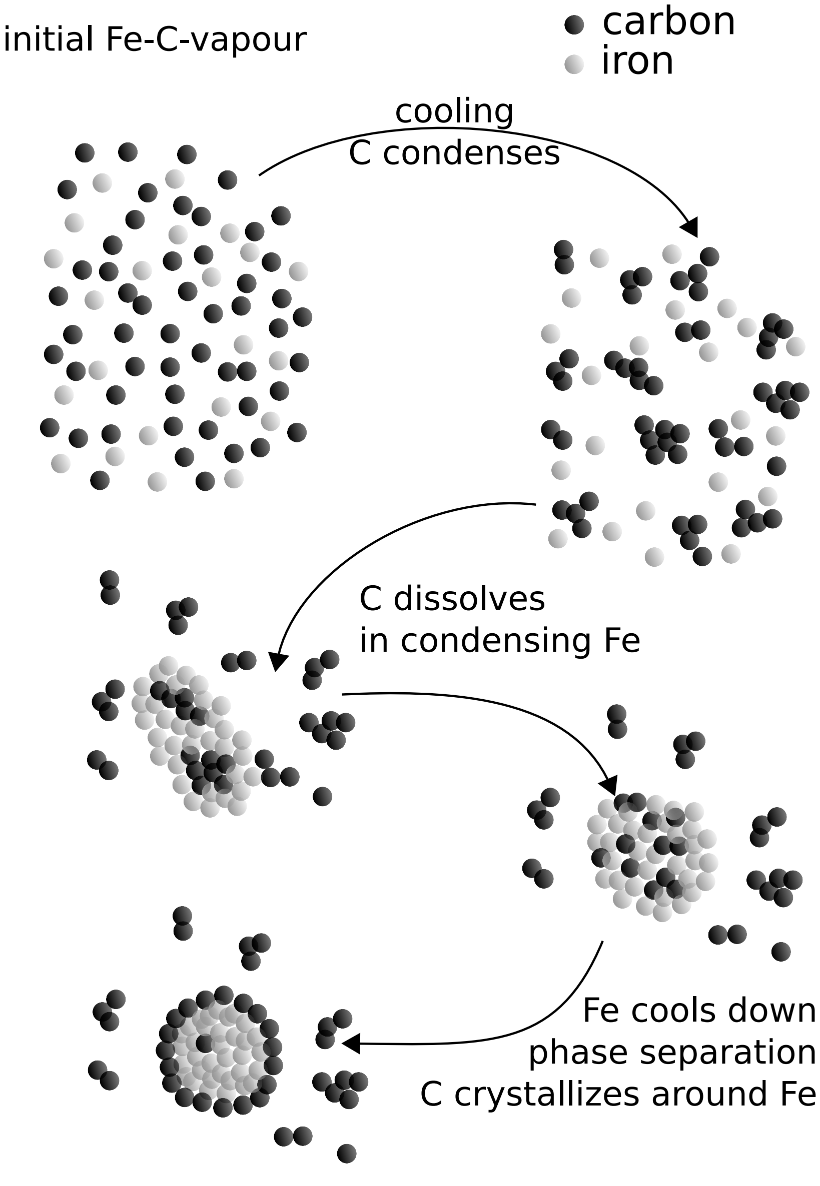

Figure 4.1: This graphic illustrates the formation of the carbon shells around the iron granules. After the carbon-iron mixture has been evaporated, carbon condenses and forms small aggregates. The iron condenses, too, forming nanoparticles. The carbon nanoparticles then dissolve in the iron nanoparticles. Further cooling leads to phase transitions of the iron which forces the dissolved excess carbon out. The condensing carbon crystallizes as one or several graphene layers around the iron core.

Thus iron-core carbon-onions are produced. The process of formation is illustrated in Figure 4.1. According to Galakhov et al. (2011); Galakhov et al. (2010), the graphene shells around these particles carry many Stone-Thrower-Wales defects.

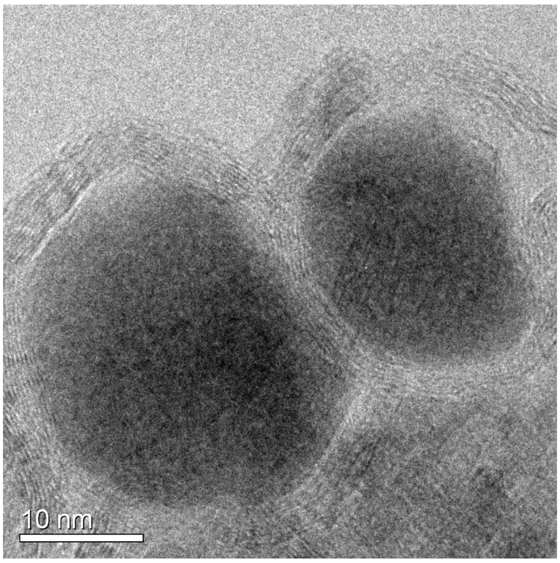

Figure 4.2: The HRTEM image shows two iron granules of a size of 20 to 30 nm. The graphitic shell around them is clearly visible and consists of around 10 layers. The sample was made from laser-ablated FC14 which was diluted with carbon powder.

The amount of soluble carbon is proportional to the mass of the solvent. Assuming that the iron granules are spherical with a radius r_{FeG}, we can conclude that we should expect thicker carbon layers d_{CS} around bigger granules. In the case, that the thickness is expected to be smaller than the radius, we can approximate:

$$m_{FeG} = V_{FeG}\rho = \frac{4}{3}\pi r_{FeG}^3 \rho \tag{4.1}$$

$$m_{CS} \propto m_{FeG} \rightarrow m_{CS} \propto r_{FeG}^3 \tag{4.2}$$

$$m_{CS} \approx 4\pi r_{FeG}^2 \cdot d_{CS} \quad d_{CS} < r_{FeG} \tag{4.3}$$

$$d_{CS} \approx \frac{m_{CS}}{4\pi r_{FeG}^2} \tag{4.4}$$

$$\rightarrow d_{CS} \propto \frac{r_{FeG}^3}{r_{FeG}^2} = r_{FeG} \tag{4.5}$$

Comparing Figure 4.2, Figure 4.3 and Figure 4.4, one will notice that smaller iron nanoparticles carry smaller shells.

The minimum size of iron granules found in the FC14-sample was about 10 nm in diameter. The other samples produced with FeC15 and FeC5, yielded smaller sizes of 2 to 6 nm (Figure 4.5). Still, bigger granules were formed every now and

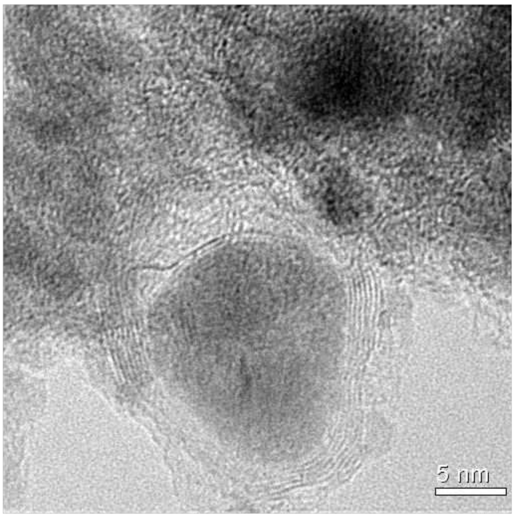

Figure 4.3: The HRTEM image shows a pear shaped iron granule with a dimension of roughly $15\,nm$. The graphitic shell is clearly visible and consists of around 6 layers. The sample was made from laser-ablated FC14 which was diluted with carbon powder.

then, but the majority of iron particles was rather small, in a range of $2-6\,nm$ (Figure 4.6).

We cannot exclude the presence of smaller particles. But since the HRTEM is sensitive to the amount of matter in the column the electron wave propagates through, smaller iron particles are difficult to detect. Furthermore, their graphene shells, if fully present at all, were hardly detectable.

Furthermore, we found that the iron did not react with contaminants like oxygen or water in the atmosphere. We would have expected iron-oxides or iron-hydroxides to form (Figure 4.1.1), in case it did react with one of the possible contaminants. We did not find any bands in the IR other than those related to carbon-compounds.

This result comes to no surprise as the excess carbon reacts with all possible contaminants to form volatile carbon dioxide and monoxide.

Additionally, lattice fringes could be observed in many iron particles (Figure 4.7) with distances of 0.204 Å— hinting at α-iron particles.

Position of IR-features of $Fe_xO_yH_z$		
haematite $\alpha - Fe_2O_3$	15.5, 19, 21.5	μm
magnetite $Fe(II)Fe(III)_2O_4$	17.5	μm
goethite $\alpha - Fe(III)O(OH)$	11, 12.5, 15, 16.5, 21	μm

Table 4.1: Absorption features of iron-containing minerals. Taken from Salisbury et al. (1992).

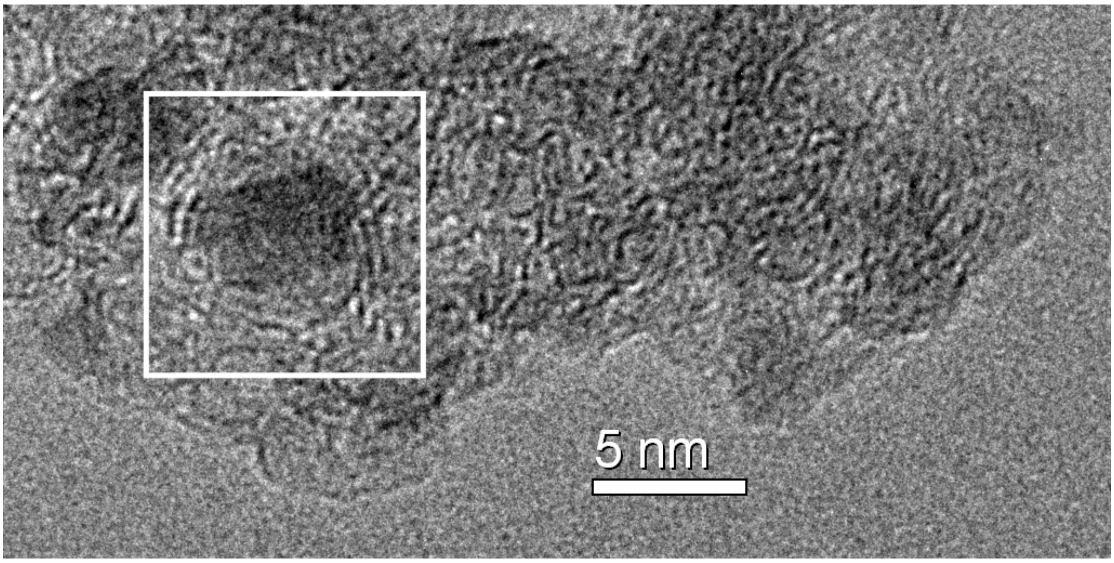

Figure 4.4: This HRTEM image of LA26 shows a nearly spherical iron particle of $5\,nm$ in diameter (boxed). The shell is visible and it consists of three layers. LA26 has been made from FeC15 powder.

4.1.2 The Influence of Hydrogen

As it can be seen in Figure 4.8, those iron-carbon-samples that were ablated under a composite atmosphere of helium and hydrogen, have a significantly higher mass absorption coefficient than those ablated under a pure helium atmosphere.

As the plasmon band of iron is still invisible, the major fraction of the ablated material should be carbon. However, a generally higher iron content for the ablation under a hydrogen-containing atmosphere is reasonable: The laser power was set to $100\,mJ$-pulses to make sure, that AC material was produced. Simultaneously, a sufficiently high laser power might favour the formation of volatile carbon species if hydrogen is present. These gas-phase species, e.g. methane, do not stick to any substrate and thus do not contribute to the deposited layer of carbonaceous material. When the carbon-iron mixture is evaporated, carbon vapour and iron vapour are formed. Some of the evaporated carbon dissolves in the iron, some of the evaporated carbon will form amorphous carbon, if there is no hydrogen present. The pure carbon particles are more likely to be extracted by the skimmer and nozzle because these nanoparticles will be easily carried to the nozzle by the gas flow because they are lighter and have a lower density. The iron particles are less likely to follow the gas flow, as they are too heavy and too dense. When hydrogen is present, that part of the carbon that would otherwise form the AC-matrix, reacts with the hydrogen forming volatile species. This increases the iron content by depleting the amount of carbon that could stick to the substrate.

This allows us, at least in theory, to control the iron content of the material in

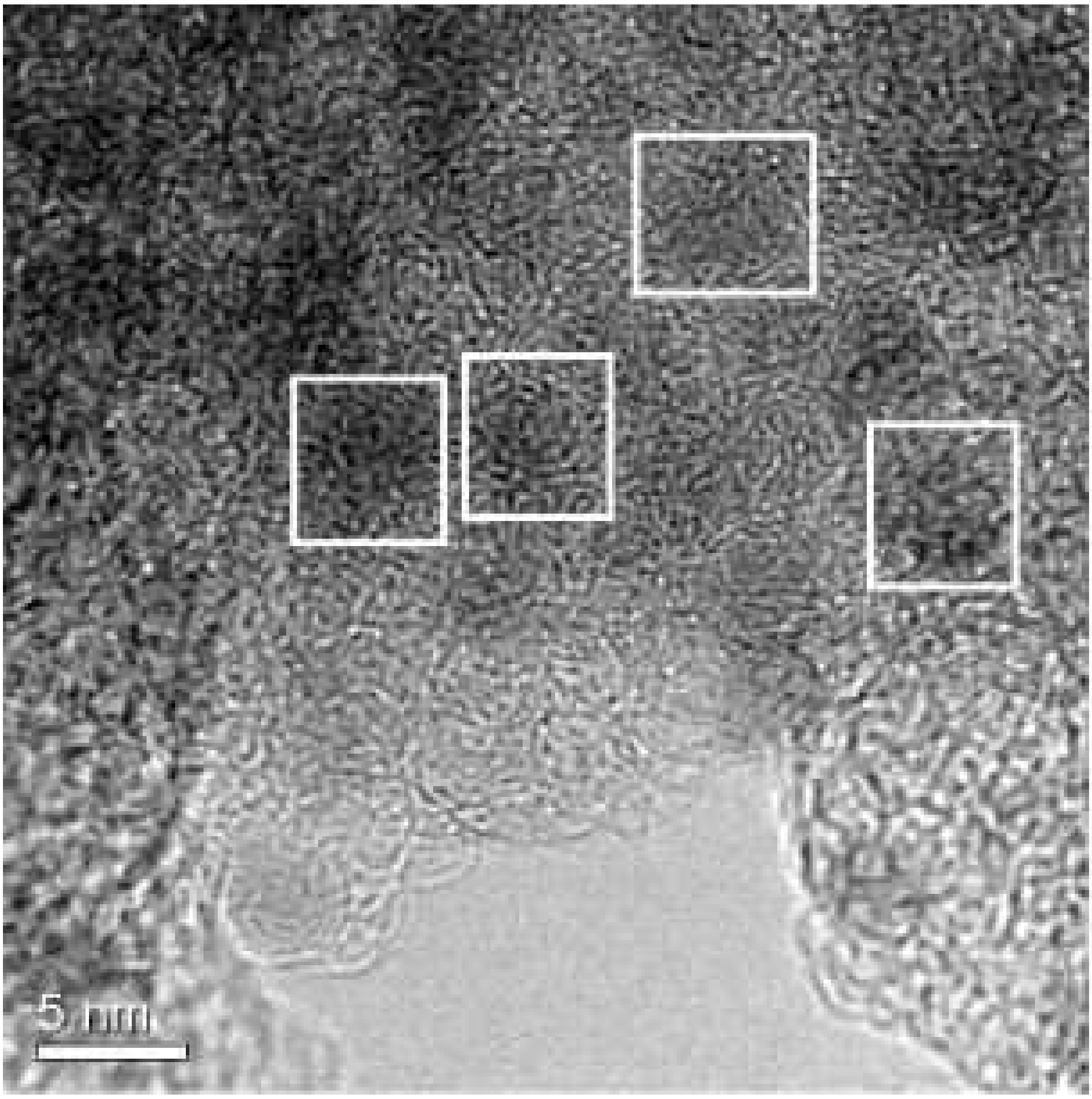

Figure 4.5: This HRTEM image of LA14 shows nearly spherical iron particles of 5 nm in diameter (boxed). The shell is visible and it consists of three layers. LA14 has been made from FeC15 powder.

certain range. Laser power on the other hand, as a way of manipulating the iron content, might have an influence as well. However, three samples were prepared with different laser powers ranging from 100 mJ to 250 mJ per pulse. Neither spectroscopically nor with the HRTEM did they show any significant differences.

The overall gas pressure of the atmosphere might look like a suitable parameter to control the size of the iron particles, as a higher pressure increases the gas drag on the iron-containing particles. However, this would affect the morphology of the excess carbon and the amount of available carbon would increase, too.

The addition of hydrogen, however, looks like a promising candidate to increase the iron content and, simultaneously depleting the excess carbon. With that

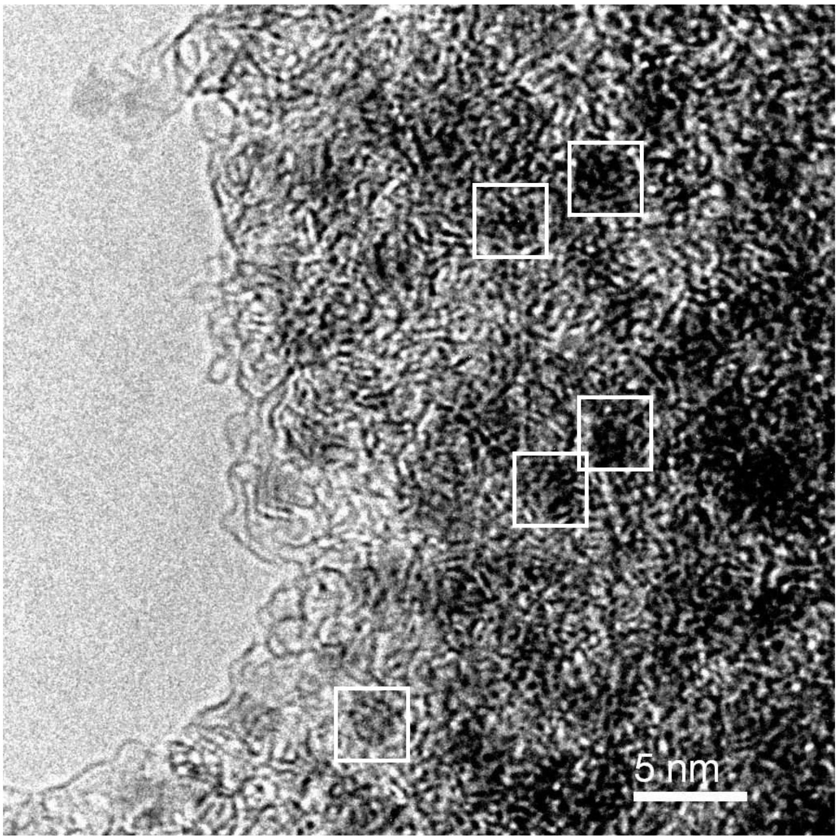

Figure 4.6: This HRTEM image of LA67 shows a graphitic region with many bent layers. On the right hand side of the image iron nanoparticles smaller than 5 nm can be seen. They have been boxed for clarity. LA67 has been made from FeC15 powder.

possibility, the overall pressure might then be used to influence the iron-carbon particle size.

There is one trait of the condensate, we already know, we can only control within certain limits: the number of graphene layers around the iron-core (subsection 4.1.1).

4.1.3 Deconvolution of the Spectra of the Iron-Containing Samples

In the π-band region, instead of only one broad band for the carbon, the iron-containing samples require more than that. Firstly, the plasmon peak of iron is set at $3.3\,\mu m^{-1}$ (Ordal et al., 1983). Secondly, the amorphous matrix materials around the iron granules has its own band, which will be fixed at $3.3\,\mu m^{-1}$, and, thirdly there is graphene layer around each sufficiently big iron granule. As the centres of the bands are relatively close to each other, the fitting routine might run into difficulties.

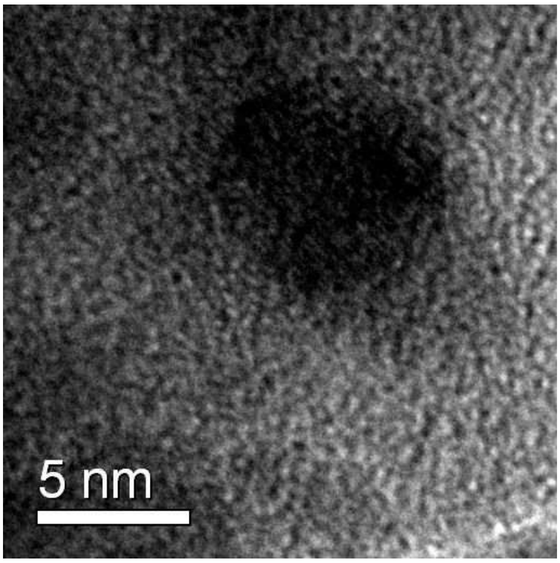

Figure 4.7: The HRTEM image shows an iron particle. The iron particle's lattice fringes are clearly visible, indicating that the iron is pure α-iron and in a crystalline state.

As an example we present the deconvolution of LA28 (FeHAC5):

The first attempt (Figure 4.9) was done as if no iron were present — one band in the π-region and one in the σ-region. The result for the unirradiated sample is unsatisfying, but the bands lie in a range that is physically reasonable. The fit of the irradiated spectrum looks much better, although the fit did not catch the shoulder at $5\,\mu m^{-1}$. Interestingly, the fitting routine yielded ten similar, if not nearly identical solutions, that all managed to find the iron plasmon by itself. However, the π-band lies beyond $5\,\mu m^{-1}$ which might be physically reasonable with respect to bent structures (Rance et al., 2010), but, compared with the deconvolution of other samples, it is improbable.

The second attempt used three bands (Figure 4.10): one for the iron plasmon and each one for the π- and σ-band of carbon. Although the resulting fit looks acceptable, the band position of the π-transition band is unphysical lying beyond $5\,\mu m^{-1}$ and being extremely strong as well. The fit of the unirradiated sample needs improvement, whereas the fit of the irradiated sample is relatively good. However, it did not manage to get the shoulder at $5\,\mu m^{-1}$. The band at $2.7\,\mu m^{-1}$ might be interpreted as graphite plasmons.

Figure 4.11 shows the third attempt with three bands to be placed in the π-region. Although both fits do look acceptable, it components are questionable. A huge band arises beyond $6\,\mu m^{-1}$ which is neither π- nor σ-band. Here we face the problem of a lack of information and missing boundary conditions. If we knew the parameters of the σ-band, we could inhibit the use of this band that is

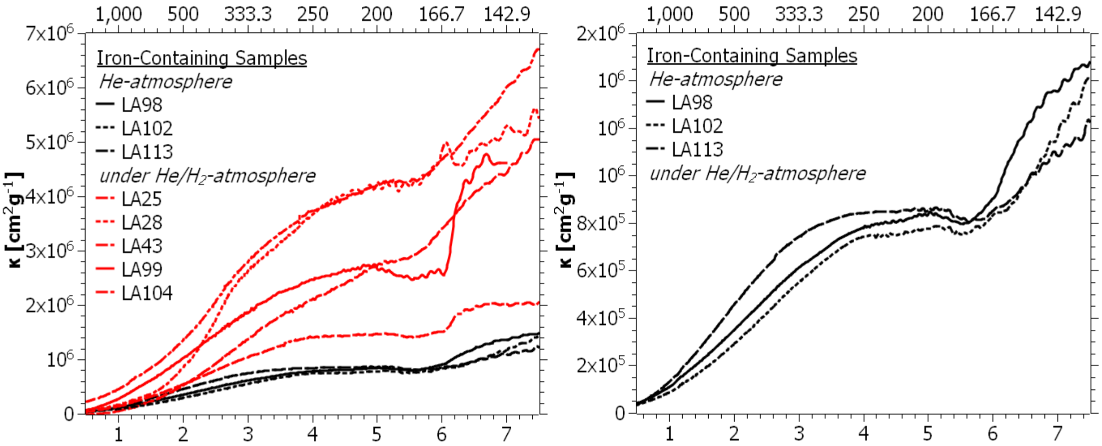

Figure 4.8: The graph on the left shows the UV-spectra of several different samples that incorporate iron. In this plot the samples that were produced under a pure helium atmosphere, are plotted with black curves, whereas those that were produced in a hydrogen-helium atmosphere are plotted in red. In order to enhance the clarity, because the mass absorption coefficient of the sample produced under a hydrogen-containing atmosphere, is higher than for those produced without hydrogen, the iron-carbon samples that were produced under a pure helium atmosphere without any hydrogen, are shown again on the right side in more detail.

neither-π-nor-σ-band, by the programme. The red-slope of the σ-band determines the blue-side boundaries of the π-bands, the position and strength of the plasmon band determines the red-side boundaries. Since the programme starts off with a Monte-Carlo method, the parameters of the plasmon band (except for the central wavenumber) and the σ-band are chosen randomly. Hence, everything in between is subject to a random process which optimizes without knowing any physics.

Therefore, the deconvolution of iron-containing samples will be limited to only those that are thin and contain relatively little iron.

Finally, fitting the processed material is easier than fitting the unprocessed material. This implies that the processed material is more uniform, which should come to no surprise.

4.2 Similarity among Unprocessed Precursors

The abundance of elements in the ISM is usually determined by absorption. If one can observe some features like distinct spectral bands or lines or the general shape of a band, conclusions about the absorbing species can be drawn. Unfortunately, neither carbon nor iron have very distinct features in the VUV/UV/VIS-region.

When it comes to rather general and non-distinct absorption spectra that can be fitted by soot-spectra, could the soot not be replaced by iron-containing soot?

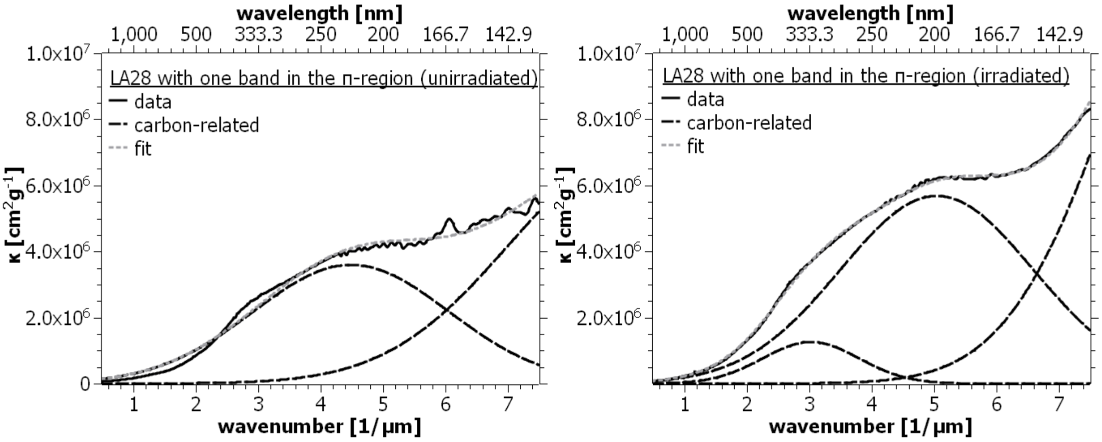

Figure 4.9: The absorption spectrum of LA28 fitted with one π-band for carbon without a plasmon band. The left hand side shows the unirradiated sample, the right one the irradiated sample. For the right one another band was automatically added to account for resulting structural changes.

This is the question that shall be followed in this section.

The general shape of the absorption curve of carbonaceous matter can be fitted to the observations from space (Duley and Hu, 2012). While Gadallah (2010) could fit his measured absorption spectra well to the interstellar absorption, the amount of matter that was necessary, was too much.

Next, we are going to compare the shapes of the unprocessed materials, because we want to see whether FeAC could, within limitations, serve as a substitute for HAC and AC in space, and thus reduce the amount of carbon that is required to account for the absorption.

To compare the shapes of the curves, we will apply a correlation coefficient and use it as a measure for similarity. The correlation coefficient C is defined as

$$C = \frac{\sum_i^n (x_i - \bar{x}) \cdot (y_i - \bar{y})}{\sqrt{\sum_i^n (x_i - \bar{x})^2 \cdot \sum_i^n (y_i - \bar{y})^2}} \tag{4.6}$$

Here, x_i and y_i are the mass absorption coefficient at the wavenumber ν_i, $\bar{x}$ and $\bar{y}$ are the averaged values of the mass absorption coefficient within the range of interest.

But since the correlation coefficients will be quite close to one, it is useful to define a measure of dissimilarity D as

$$D = 1000 \cdot (1 - C) \tag{4.7}$$

The bigger D is, the more differ two curves.

As range of interest $\nu = 1\,\mu m^{-1} \ldots 6\,\mu m^{-1}$ is chosen.

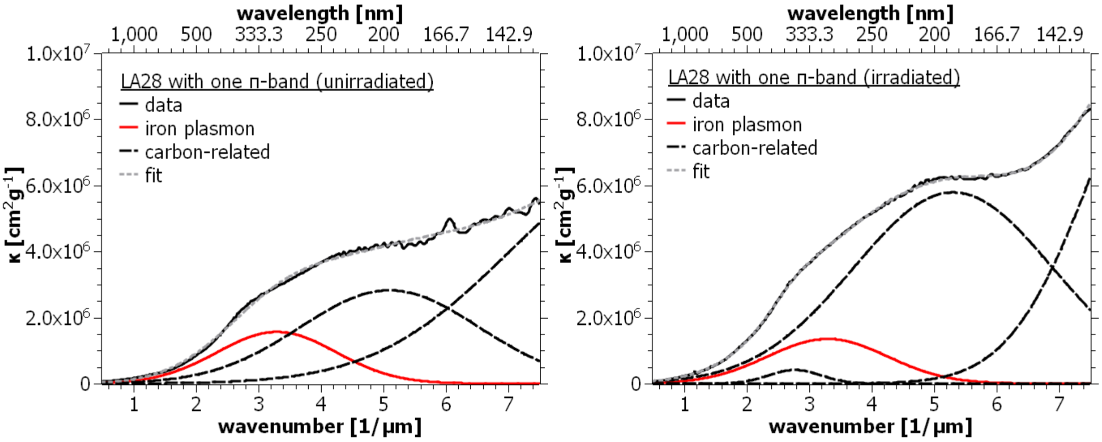

Figure 4.10: The absorption spectrum of LA28 fitted with one π-band for carbon and a plasmon band. The left hand side shows the unirradiated sample, the right one the irradiated sample. For the right one another band was automatically added to account for resulting structural changes.

	LA96	LA107	LA114	LA115	LA116	LA117
LA59	8.6	9.1	11.5	0.9	10.2	2.3
LA96		1.9	2.5	10.0	1.8	13.6
LA107			2.6	11.1	1.5	15.4
LA114				11.4	1.2	16.7
LA115					11.1	2.3
LA116						17.2

Table 4.2: This table shows the dissimilarity D among the unprocessed AC-samples.

AC-Samples

The most uniform samples were the AC samples. Table 4.2 gives an overview about the dissimilarity among them.

The biggest D that can be found is 17. We will consider this value as threshold; two samples whose D is bigger than 17, can be considered to be composed of different materials.

AC and FeAC-Samples

We will now compare AC-samples with FeAC-samples to see whether the materials could be distinguished on the shape of their mass absorption curves alone. The dissimilarities are displayed in Table 4.3.

Although the dissimilarity, especially in the case of LA113, sometimes exceeds 17, in many cases the iron-containing samples are quite similar to those without iron. As a consequence, replacing iron-free soot with iron-containing carbonaceous

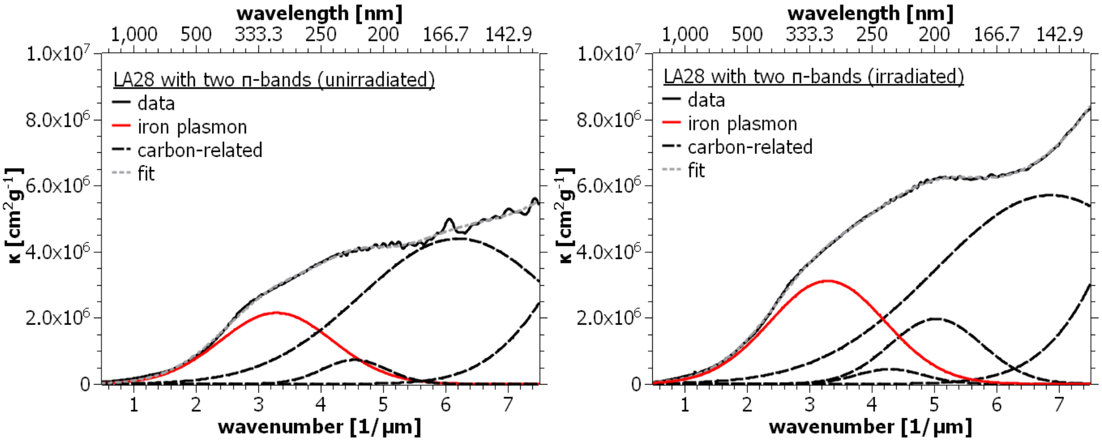

Figure 4.11: The absorption spectrum of LA28 fitted with two π-bands for carbon and a plasmon band. The left hand side shows the unirradiated sample, the right one the irradiated sample. For the right one another band was automatically added to account for resulting structural changes.

	LA25	LA28	LA43	LA99	LA98	LA103	LA113
LA59	4.3	7.1	4.6	24.3	19.4	26.8	71.3
LA96	3.9	7.7	22.2	10.6	5.4	10.8	36.2
LA107	3.3	6.7	22.4	8.0	3.4	8.4	34.2
LA114	6.6	11.8	29.1	9.8	5.0	12.4	27.8
LA115	6.8	10.6	6.8	26.8	22.0	30.8	72.0
LA116	3.6	7.0	26.4	6.0	2.6	7.6	29.1
LA117	10.6	15.2	4.5	38.1	30.1	40.3	85.1

Table 4.3: This table shows the dissimilarity D among between unprocessed AC-samples and iron-containing samples.

materials might be a viable way to reduce the amount of carbon needed to fit absorption spectra. This can also account for the depletion of iron.

4.3 ArF-Laser: 193nm (ArF)

As extension and continuation of my master's thesis, the ArF-irradiations were continued with iron-containing material.
The doses the samples were exposed to, were kept in the range of Habing's dose (Habing, 1968; Mennella et al., 1996).

Similar to previous experiments (Walter, 2013), the irradiated spot was not marked by any changes visible to the naked eye. To avoid the problem of identifying the spot, a piece of paper was kept behind the sample with its silhouette marked. The irradiation caused the paper to darken, thus the irradiated spot could be identified without any problems.

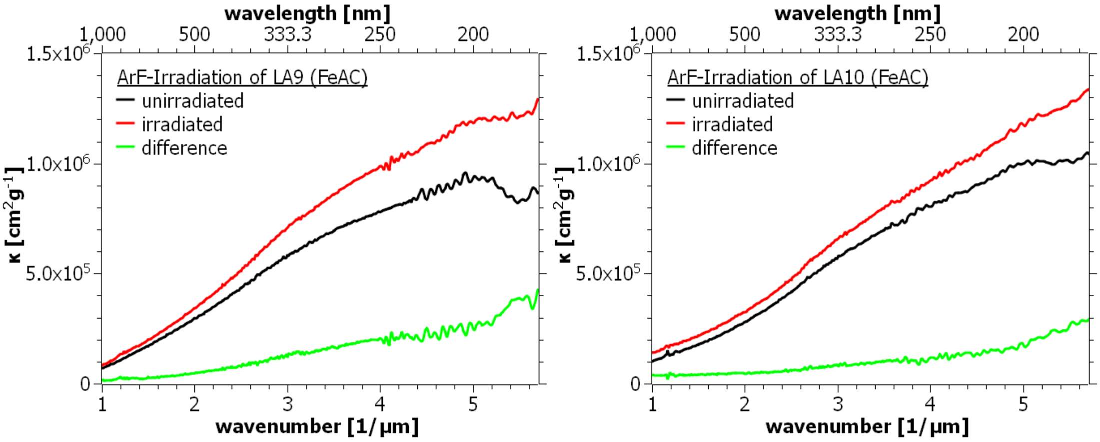

Figure 4.12: LA9 ($6 \cdot 10^{22}\, eV cm^{-2}$) and LA10 ($16 \cdot 10^{22}\, eV cm^{-2}$), iron-containing AC samples irradiated with ArF photons at the IFK.

The iron-containing AC samples LA9 and LA10 (Figure 4.12) did not change significantly in the VIS. The $\sigma \rightarrow \sigma^{\star}$-transition band increased in strength, the $\pi \rightarrow \pi^{\star}$-band increased much less. This behaviour can be understood as the establishment of some new bonds, mostly single bonds. These could stem from the additional aliphatic connections, that formed upon irradiation, between adjacent graphene layers. Only very few new π-bonds formed.

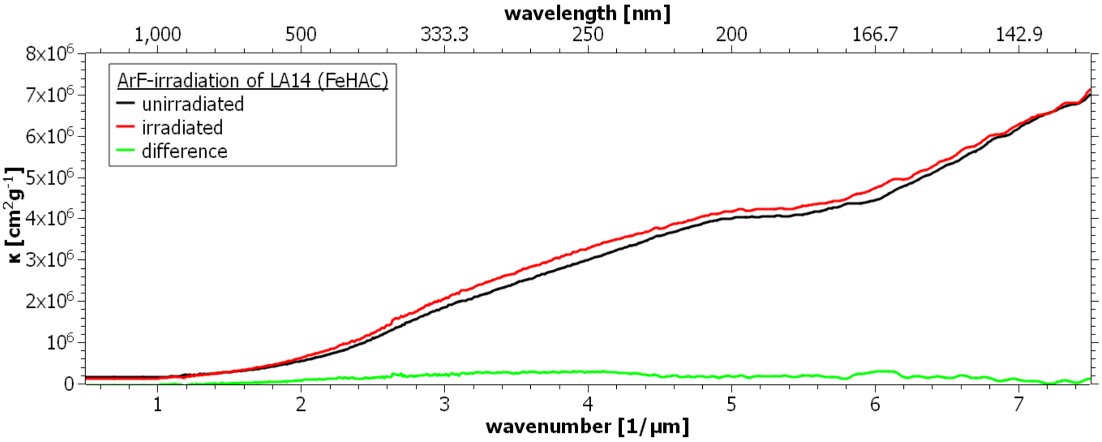

Figure 4.13: LA14 ($6 \cdot 10^{22}\, eV cm^{-2}$), an iron-containing HAC sample irradiated with ArF photons at the IFK.

The FeHAC-samples were irradiated with similar doses. The difference of the mass absorption coefficient of the FeHAC and FeAC samples is identical in absolute terms. The sample LA14 (Figure 4.13) showed nearly no change at all, the other two samples, LA16 (Figure 4.14) and LA17 (Figure 4.15), showed a slightly bigger relative increase. However, the changes were the same: Mostly new σ-bands were formed.

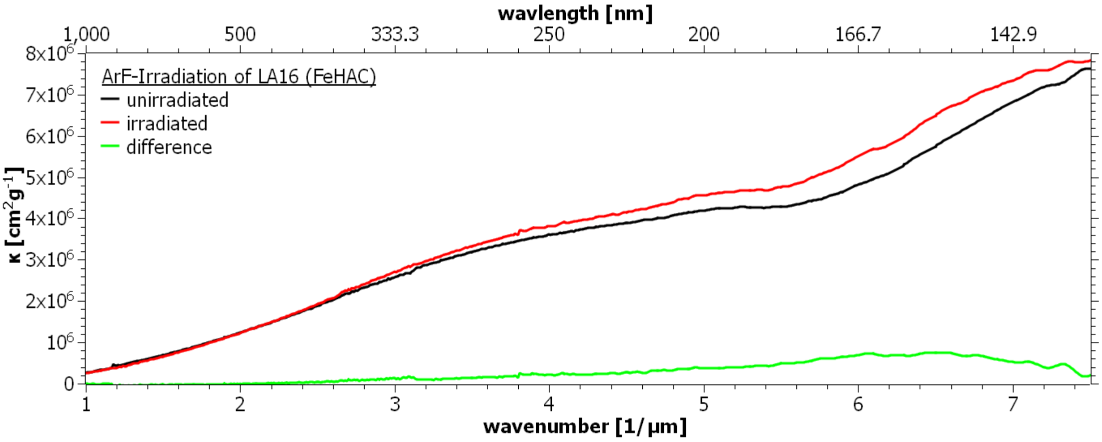

Figure 4.14: LA16 ($9.4 \cdot 10^{22}\, eV cm^{-2}$), an iron-containing HAC sample irradiated with ArF photons at the IFK.

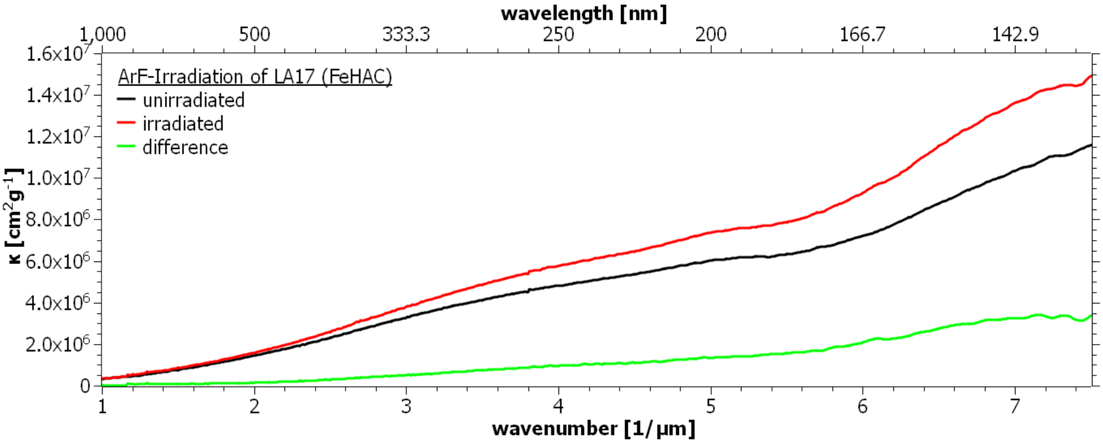

Figure 4.15: LA17 ($6 \cdot 10^{22}\, eV cm^{-2}$), an iron-containing HAC sample irradiated with ArF photons at the IFK.

The photons of the ArF-laser at $193\, nm$, or $6.4\, eV$, do not introduce major changes to the irradiated iron-containing samples. Even though the doses applied were in the order of magnitude of Habing's dose ($3 \cdot 10^{23} eV cm^{-2}$), major graphitization did not take place. The only major change that could be observed was the formation of more single bonds between the carbon atoms — illustrated in Figure 4.16 — and a slight increase in the strength of the π-band. The energy of the photons is sufficient to break $H{-}C$ and $C{-}C$, and nominally also $C{=}C$ according to Table 2.3. Thus, these photons cannot be expected to cause major changes in the material aside from dehydrogenation and the subsequent formation of new single bonds between adjacent graphitic regions, some graphitization. Graphitic areas can be considered to be mostly unaffected by the ArF-photons. However, another effect is acting as well: intense heating. With a pulse duration of $8\, ns$, a pulse energy of $2\, mJ$ and area of $A = 18\, mm^2$, the available power density F

becomes $1.4\,MWcm^{-2}$ which is three order of magnitude below the energy density used in the laser ablation. The transmission of the calcium fluoride window is $T \approx 0.8$ for $193\,nm$, reducing the power density to $F = 1.1\,MWcm^{-2}$. The layers have thicknesses in the range equivalent to around 10 nanometers. Neglecting heat transfer, we can estimate an upper limit for the temperature rise the layer experiences upon irradiation. For LA10, which has a thickness corresponding to $10\,nm$, the mass absorption coefficient at $193\,nm$ is $\kappa \approx 10^6\,cm^2g^{-1}$. With a density of $\rho = 1.3\,gcm^{-3}$, the transmission becomes $T = 0.27$. This yields a power density of $0.8\,MWcm^{-2}$. Using Stefan-Boltzmann's law (Boltzmann, 1884), the maximum temperature T_m of the material can be estimated, assuming that the material's thermal emission equals the incoming laser power:

$$P_{laser} + \sigma A T_0^4 = \sigma A T_m \tag{4.8}$$

$$T_m = \sqrt[4]{\frac{P_{laser}}{\sigma A} + T_0^4} \tag{4.9}$$

$$\tag{4.10}$$

Here, P_{laser} is the power of the laser beam inciding on the sample and $T_0 = 293\,K$ is room temperature. The maximum equilibrium temperature is about $19000\,K$ (though probably lower due to heat conduction). It is thus quite likely that at least some areas heat up considerably, even though only for short periods. The intense short-time heating produces high pressures which can transform some of the sites of carbon into sp^3 sites, as has already been shown by Narayan and Bhaumik (2015). Furthermore, this process might even, in principle, evaporate parts of the material: When I did irradiation experiments on AC and HAC samples with a fluorine excimer laser ($\lambda = 157\,nm$, pulsed) at the IPHT in Jena with Dr. Thomas Zeuner in February 2013 as follow-up of my master's thesis, the laser, even though with a lower power density, managed to evaporate the sample within a minute.

Finally, both processes seem to be competing: The heating causes the transformation of the material into sp^3-sites, whereas its dissipating heat anneals the material favouring graphitization and the photons — with respect to their wavelength — break sp^3 sites allowing them to re-arrange and dehydrogenate the material.

4.4 Deuterium-Lamp: 167nm (DUV)

The $167\,nm$-photons of the deuterium-lamp, referred to as DUV, are mostly produced by molecular emissions of deuterium — analogous to Cottin et al. (2003); Mennella et al. (2006). Unlike the ArF-photons, the DUV-photons are capable of

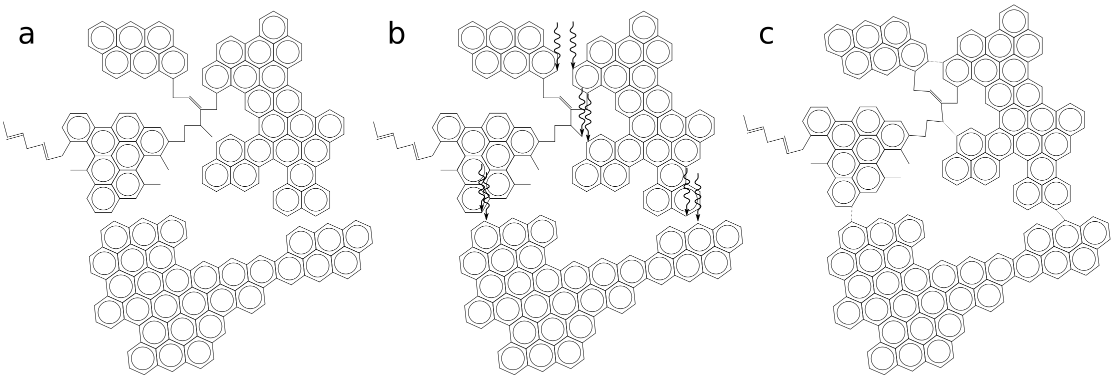

Figure 4.16: The illustration shows the principle of the formation of σ-bonds in soot. The images do not show the hydrogen bound to the carbon, for reasons of clarity. Graphitization, which naturally occurs too, has been omitted as well for reasons of clarity. The untreated material (a) is irradiated by photons (b), looses hydrogen and forms new single bonds between adjacent aromatic layers. The newly formed bonds are depicted as dotted lines in (c).

breaking double bonds in carbonaceous matter.

The output of the deuterium lamp is a portion of the general photon-field of photo-dominated regions (Tielens, 2006).

4.4.1 Iron-Free Material

AC: LA96, LA107

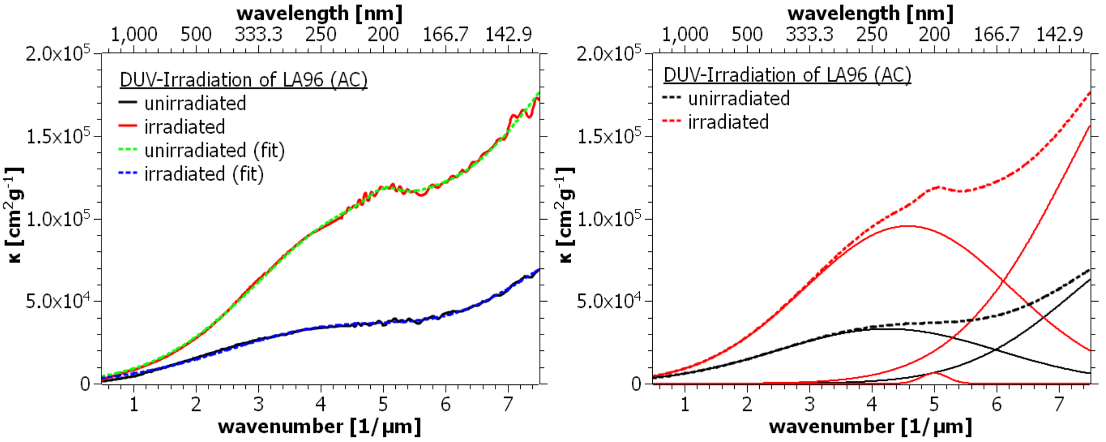

Figure 4.17: LA96 ($29 \cdot 10^{21}\, eV cm^{-2}$), an iron-free AC sample irradiated with DUV photons at the AIU.

LA96 is relatively thin ($75\, nm$) with respect to the penetration depth of DUV in AC ($140\, nm$). The sample was significantly graphitized by the irradiation, as shown by the rise of the mass absorption coefficient in the VIS and UV-range.

This is related to the increase of the $\pi \rightarrow \pi^\star$-absorption. Since the $\sigma \rightarrow \sigma^\star$-band increased, too, it can be safely assumed that the number of bonds in general has increased significantly. Furthermore, a new band emerged at $5.01\,\mu m^{-1}$. This band is not very distinct, but every successful deconvolution created a band at that position.

LA107, a very thin AC sample ($45\,nm$), has been irradiated with a tenth of the dose of LA96. The reasoning behind that attempt was to diminish the effect of lower energy photons: The lower energy photons do have a deeper penetration depth than the higher energy ones. By decreasing the sample thickness, the overall interaction of the higher energy photons increases relative to the lower energy ones. LA107 shows a plasmon peak which shifts to the blue upon irradiation and becomes stronger. Accordingly, the π-band narrows and becomes stronger, which is a sign for graphitization. However, the degree of additional graphitization is smaller than in LA96. Furthermore, a new band at $4.93\,\mu m^{-1}$ emerged.

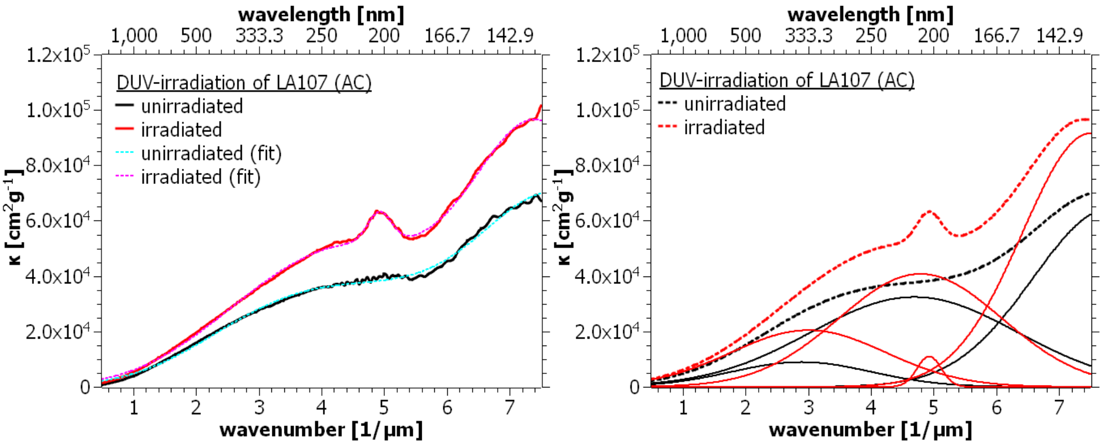

Figure 4.18: LA107 ($3.2 \cdot 10^{21}\,eV\,cm^{-2}$), an iron-free AC sample irradiated with DUV photons at the AIU.

A useful measure to describe how a layer of material is processed by photons with a broad distribution of energies, is the range of domination. The range of domination (ROD) is related to the penetration depth and describes at which depth which kind of processing dominates with respect to the photon energies. Assuming that the distribution of photons in the output of a source is relatively broad, the output spectrum can be divided into different bands of different energies according to which bonds they can break. In Table 3.4 the output of the deuterium lamp has been divided into three bands: The C-band contains all photons that can break single bonds, but no double bonds, the B-band contains all photons that can break double bonds, but not triple bonds and the A-band contains all those that can break triple bonds. If the effects of different photons on the material would not compete with each other, the range of domination would be their penetration depth. However, the number of photons in each band must be taken into account, too. The probability p of a photon whose penetration depth is L, of being absorbed along a small path δx is $p = \exp(-\delta x/L)$. The penetration depth decreases as the photon energy increases in the UV/VIS-range, thus higher energy photons are more likely to be absorbed. However, consider a distribution of photons of two energies with penetration depths $L_1 < L_2$ and their respective energies $E_1 > E_2$. The amount of E_1-photons is n_1, that of E_2 is n_2. The eventually absorbed amount of photons N_i along a path δx is of importance. Thus $N_i = n_i \int_0^{\delta x} \exp(-x/L_i)\, dx$. Hence, the ratio N_1/N_2 at every location determines what kind of processing takes place. But there is another factor that needs to be considered: the effect itself. The effect caused by E_1 might be very different from E_2 and more significant. The inability to quantify the processing in a single number like the *relative biological effectiveness* in the context of radio-activity makes the concept of ROD difficult to use. Without similar quantities like a relative processing effectiveness, the ROD-concept delivers only fuzzy ranges or transition zones.

In the context of this fuzziness, the effect of 167 nm-photons cannot be completely isolated from that of higher or lower energy photons, but the contributions of the other bands can be reduced. Since the ratio D of photons that have been absorbed along a path of length x

$$D(x) = \frac{N_1}{N_2} \cdot \frac{1 - e^{-x/L_1}}{1 - e^{-x/L_2}} \tag{4.11}$$

is monotone with respect to x, it can be derived that for thin layers ($x \to 0$) the photons with the shorter penetration depth will be more dominant than in thicker samples.

HAC: LA97, LA110

As already observed in the DUV-irradiation experiments, the hydrogen-containing carbon sample LA97 graphitized as well upon irradiation, as the $\pi \to \pi^\star$-band grew significantly. Similar to LA96, a new band emerged at 5.04 μm^{-1}. But here, the band is more pronounced and is, relative to its other bands, twice as strong as in the AC-sample LA96.

The hydrogen content of is higher than LA110 (Figure 4.20) than that of LA97. LA110 is thicker (351 nm) than LA97 (70 nm). Therefore the material experienced graphitization as dominant process. Unfortunately, it was so much, that the transmission beyond 6 μm^{-1} decreased so much, increasing the signal-to-

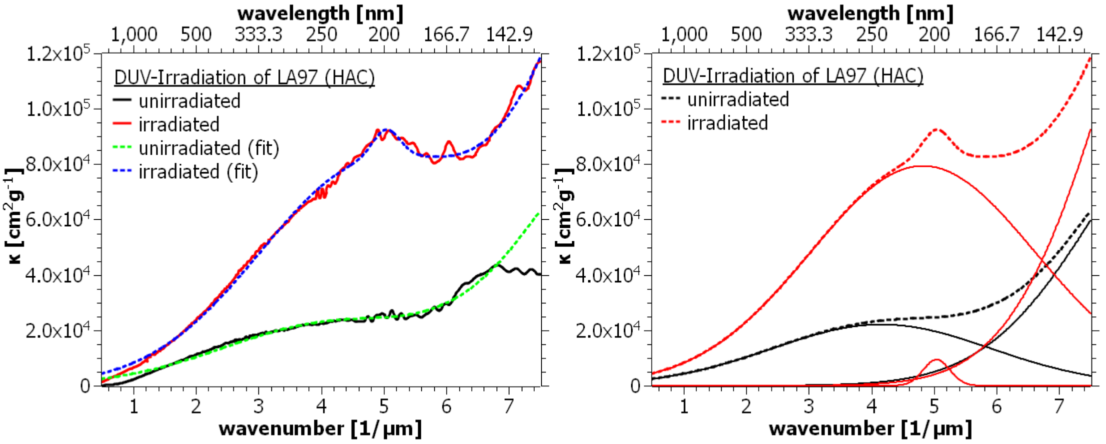

Figure 4.19: LA97 ($24 \cdot 10^{21}\, eV cm^{-2}$), an iron-free HAC sample irradiated with DUV photons at the AIU.

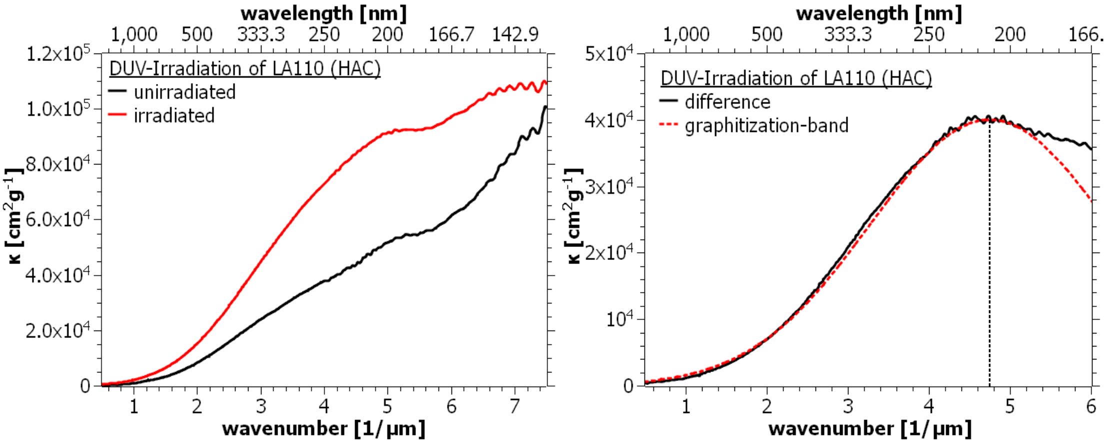

Figure 4.20: LA110 ($40 \cdot 10^{21}\, eV cm^{-2}$), an iron-free HAC sample irradiated with DUV photons at the AIU.

noise ratio, that the absorption values become unreliable. However, it can be safely assumed that the absorption values there are considerably higher than computed from the data that is basically the dark current of the spectrometer — this is the trade-off that has to be paid, when the lower energy photons shall be the dominant ones.

Hence, a proper deconvolution is not possible. What can be done instead, is to compute the difference between both spectra and consider only the reliable part. The finding is quite interesting: the difference is, at least in the reliable region, Gaussian-shaped. We can interpret this difference directly. The removal of hydrogen only decreases the number of σ-bonds. A secondary, but subsequent effect is the formation of new bonds between the carbon atoms. When aromatic units form, the $\pi \rightarrow \pi^{\star}$-band increases. What we see here as difference are in fact the newly formed graphitic sub-units — simply added to the already existing ones. The centre of the Gaussian curve is at $4.75\,\mu m^{-1}$. In terms of nanotube diameter we should expect, according to Rance et al. (2010), a diameter of $0.8\,nm$ or a curvature of $1.24\,nm^{-1}$ with a significant standard deviation.

4.4.2 Iron-Containing Material

FeAC: LA98

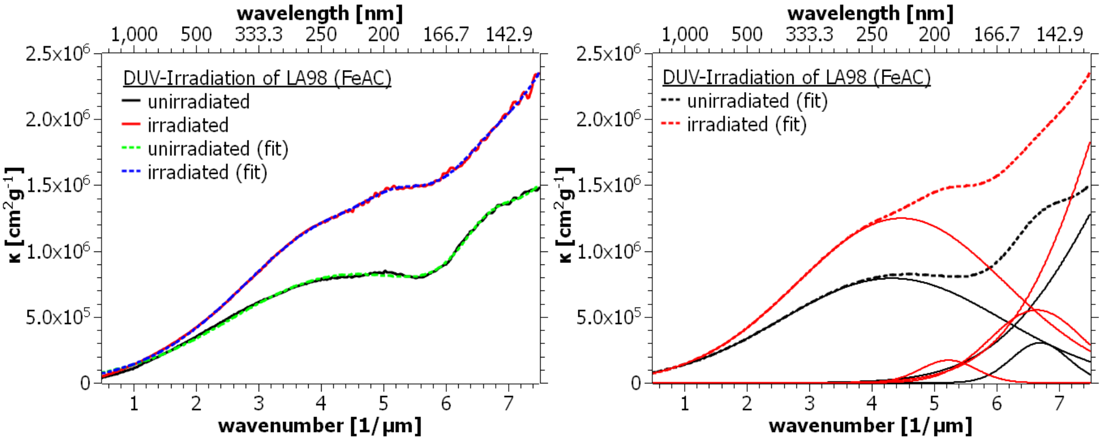

Figure 4.21: LA98 ($31 \cdot 10^{21}\,eV cm^{-2}$), an iron-contaning AC sample irradiated with DUV photons at the AIU.

In LA98 (Figure 4.21), a rather thick sample, graphitization took place, too. It was necessary to add a physically-meaningless band at roughly $6.7\,\mu m^{-1}$ to achieve a good deconvolution. This additional band is a consequence and necessity of the limited range the spectrometer can measure. The $\sigma \rightarrow \sigma^{\star}$-band grows about the same ratio as the $\pi \rightarrow \pi^{\star}$-band does. This indicates that whatever new bonds were formed, they were probably aromatic.

A new band emerges as well, at least according to the deconvolution. The position of the band at $5.23\,\mu m^{-1}$ coincides with oxygen's $n \rightarrow \sigma^{\star}$-transition, but its width seems unusually wide compared to other samples showing a clear oxygen bump like LA114 (Figure 4.35, Table 4.8). Furthermore, most of the samples lost their oxygen during the irradiation as it can be seen in Table 4.6 . Since, this additional band is visible as a mere shoulder in the spectrum, its position is somewhat dependent on the exact parameters of the neighbouring transition bands. Even though this small $\pi \rightarrow \pi^{\star}$-band is too far in the blue for the corresponding band that was given rise to in the other samples, it might be that this shoulder is a distorted representation of the curvature-related band. This would not be too surprising as the FeAC-samples are amorphous and fullerene-like matrices that contain graphene-covered iron-granules. The matrix is expected to behave the same way under processing as the layer of LA96. If one compared the mass absorption coefficient of LA96 before and after with LA98, one would find, that the increase of the $\pi \rightarrow \pi^{\star}$-band is in both samples close to $10^5 cm^2 g^{-1}$. The increase of the mass absorption coefficient of LA98 is slightly lower, as there is less material left to graphitize, than in LA96, which, in relation to its original value, increased tremendously.

FeHAC: LA99, LA25, LA28

LA99 displays mainly a rise of the $\pi \rightarrow \pi^{\star}$-band, meaning that further graphitization has taken place. The σ-band did not experience a significant rise. This indicates that the amount of new inter-aromatic connections did not rise. However, bonds that already existed were turned into aromatic bonds. To understand what has happened here, one needs to consider the conditions of production: This sample has, due to the addition of hydrogen to the quenching gas atmosphere, a generally high iron content. As a consequence, the amount of graphitic sites is generally high. This causes greater constraints for the re-arrangement of the affected atoms and consequently favours its own growth.

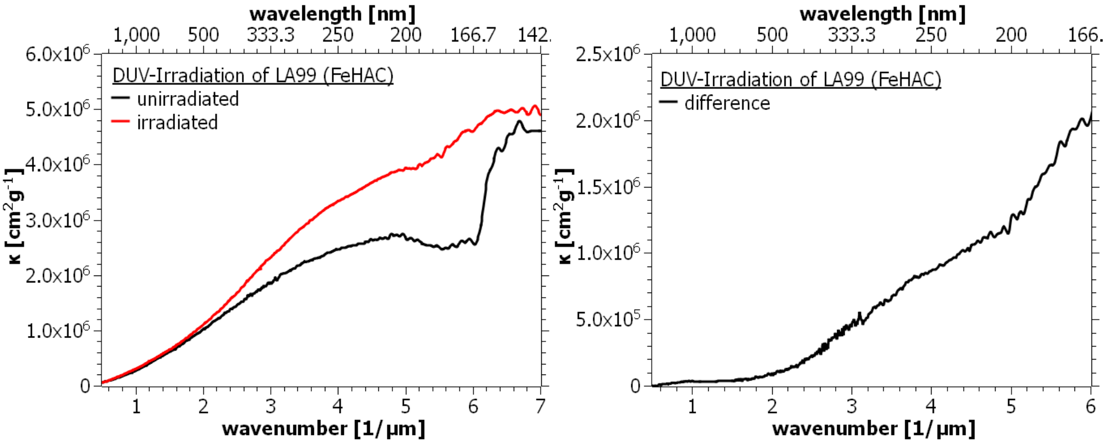

Figure 4.22: LA99 ($21 \cdot 10^{21}\, eV cm^{-2}$), an iron-contaning HAC sample irradiated with DUV photons at the AIU.

The DUV-irradiation did not only expose the samples to 166nm radiation, but also to photons of lower wavelength. A new band emerged at roughly $5\,\mu m^{-1}$. Independently from the thickness of the irradiated sample, the strength of the band seems to be stable with a maximum mass absorption coefficient of $10^4 cm^2 g^{-1}$ throughout the samples where this band can be seen clearly.

	unprocessed			*processed*		
Band	ν_0 $[\mu m^{-1}]$	FWHM $[\mu m^{-1}]$	rel. Ampl. [1]	ν_0 $[\mu m^{-1}]$	FWHM $[\mu m^{-1}]$	rel. Ampl. [1]
DUV: AC						
LA96						
$\pi \rightarrow \pi^\star$	4.26	4.16	0.48	4.59	3.89	1.39
$(\pi \rightarrow \pi^\star)_{OLC}$				5.01	0.50	0.09
$\sigma \rightarrow \sigma^\star$	8.95	4.07	1.31	9.04	4.32	3.24
LA107						
graphite plasmon	2.89	2.62	0.13	3.00	2.90	0.30
$\pi \rightarrow \pi^\star$	4.69	3.88	0.47	4.79	3.06	0.59
$(\pi \rightarrow \pi^\star)_{OLC}$				4.93	0.45	0.16
$\sigma \rightarrow \sigma^\star$	7.85	2.98	0.93	7.51	2.57	1.32
DUV: HAC						
LA97						
$\pi \rightarrow \pi^\star$	4.16	4.12	0.51	4.82	4.22	1.82
$(\pi \rightarrow \pi^\star)_{OLC}$				5.04	0.50	0.22
$\sigma \rightarrow \sigma^\star$	9.34	4.15	2.37	9.45	3.76	4.49
DUV: FeAC						
LA98						
$\pi \rightarrow \pi^\star$	4.33	4.18	0.54	4.48	3.92	0.84
$(\pi \rightarrow \pi^\star)_{OLC}$				5.23	1.04	0.11
additive	6.7	1.06	0.21	6.65	1.76	0.37
$\sigma \rightarrow \sigma^\star$	9.34	3.90	1.61	9.29	3.51	2.55

Table 4.4: This table shows the fit parameter the deconvolution has delivered for the DUV-irradiated samples.

4.5 Hydrogen Lamp: 122nm (HUV)

Hydrogen, the most abundant element in space, occurs, according to Draine (2011) in the interstellar medium mostly as ground state atomic hydrogen. Upon shocks (Schlemmer et al., 2015) it is mostly $Ly\alpha$-photons ($122\,nm$) that are emitted when the hydrogen atoms relax into the ground state again. Furthermore, the stellar radiation field of young stars is often dominated by $Ly\alpha$-photons (van Dishoeck et al., 2006). Due to its omnipresence and ability to dissociate many primitive and simple molecules, the hydrogen lamp irradiation, among all other experiments in this thesis, comes closest to the processing of interstellar dust with respect to photo-dominated regions and hydrogen clouds.

In the previous series of experiments both photons of molecular emission at $167\,nm$ and the $Ly\alpha$-line were present, the hydrogen lamp provides photons whose major constituents are photons of $\lambda = 122\,nm$. Hence, it will be easier to isolate the effects caused by higher energy photons from those of the molecular emission.

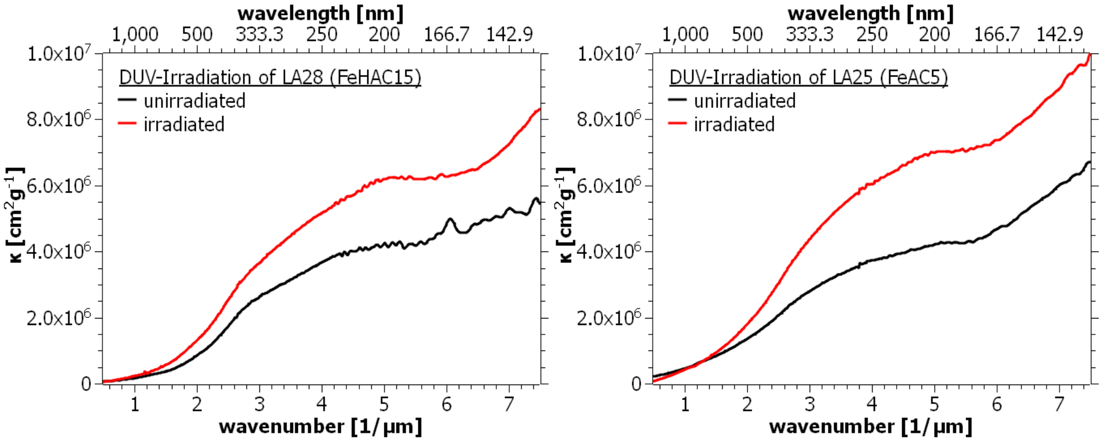

Figure 4.23: LA28 (right, $11 \cdot 10^{21}\, eV cm^{-2}$) and LA25(left, $4 \cdot 10^{21}\, eV cm^{-2}$): Both samples show an increase in graphitization. Although there is no distinct new band, a shoulder has formed at roughly $5\, \mu m^{-1}$.

4.5.1 Iron-Free Materials

AC: LA116, LA117

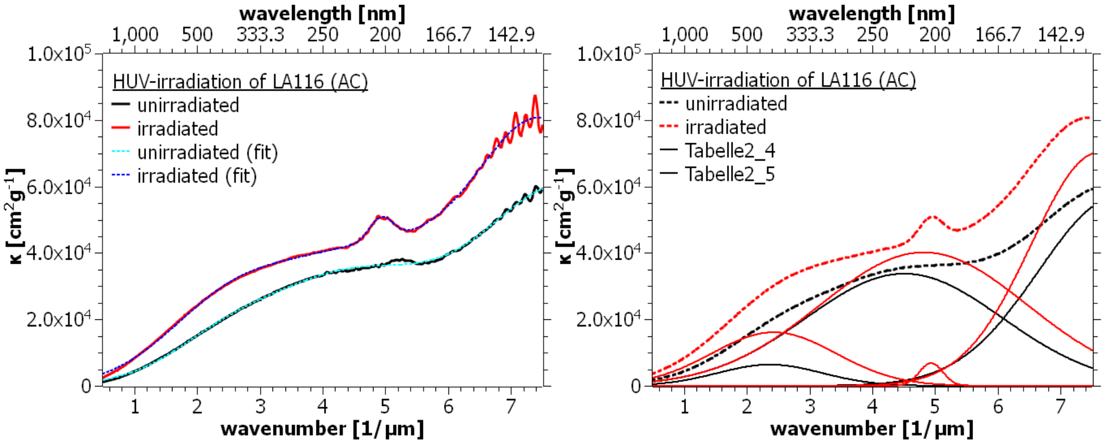

Figure 4.24: LA116 ($1.05 \cdot 10^{17}\, eV cm^{-2}$), an iron-free AC sample irradiated with HUV photons at the IFK.

For both samples, LA116 (Figure 4.24) and LA117 (Figure 4.25), the behaviour upon irradiation was similar. Both samples experienced graphitization: the mass absorption coefficient in the π-band region increased by increasing both the amount of π-bonds and by increasing the the strength of the plasmon band. Furthermore the absorption coefficient of the $\sigma \rightarrow \sigma^{\star}$-band rises, too. That means that new connections between the aromatic sites were formed. For LA117, whose dose was bigger, the graphitization was more prominent than for LA116. A clear and distinct band formed at about $5\, \mu m^{-1}$.

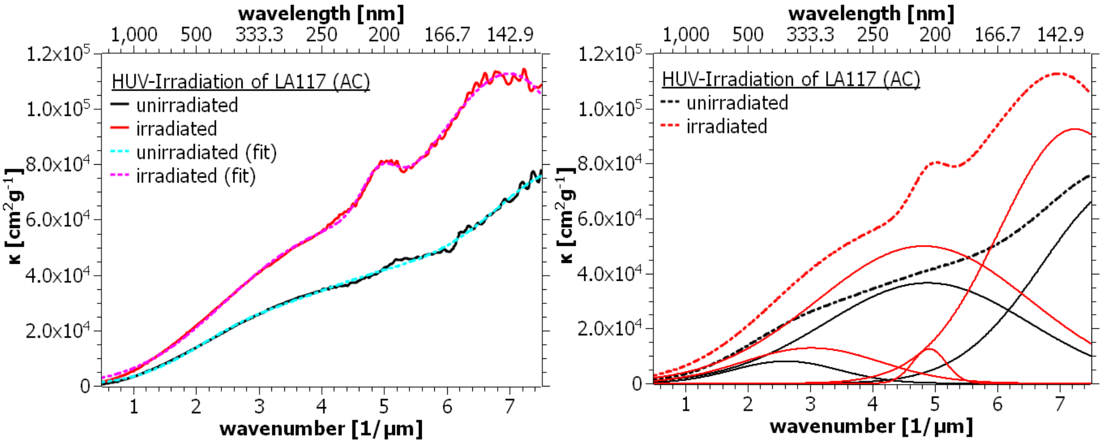

Figure 4.25: LA117 ($2.1 \cdot 10^{17}\, eV cm^{-2}$), an iron-free AC sample irradiated with HUV photons at the IFK.

Band	*unprocessed*			*processed*		
	ν_0 [μm^{-1}]	FWHM [μm^{-1}]	rel. Ampl. [1]	ν_0 [μm^{-1}]	FWHM [μm^{-1}]	rel. Ampl. [1]
HUV: AC						
LA116						
graphite plasmon	2.37	1.96	0.10	2.43	2.33	0.27
$\pi \rightarrow \pi^\star$	4.51	3.68	0.56	4.82	3.88	0.67
$(\pi \rightarrow \pi^\star)_{OLC}$				4.94	0.44	0.11
$\sigma \rightarrow \sigma^\star$	7.92	3.01	0.95	7.62	2.55	1.17
LA117						
graphite plasmon	2.61	2.00	0.10	3.03	2.60	0.17
$\pi \rightarrow \pi^\star$	4.89	3.82	0.47	4.83	4.01	0.64
$(\pi \rightarrow \pi^\star)_{OLC}$				4.92	0.63	0.16
$\sigma \rightarrow \sigma^\star$	8.09	3.17	0.93	7.25	2.83	1.19

Table 4.5: This table shows the fit parameter the deconvolution has delivered for the X-irradiated samples.

4.5.2 Iron-Containing Materials

FeAC: LA103

The iron-containing material behaves in a slightly different manner. LA103, an iron-containing AC-sample is displayed in Figure 4.26. Graphitization takes place. The formation of new single bonds is clearly visible, too. The newly formed band is strong ($\kappa \approx 10^5\, cm^2 g^{-1}$) when compared to the other two samples ($\kappa \approx 10^4\, cm^2 g^{-1}$). The central wavenumber of the band is located at $4.84\, \mu m^{-1}$.

DUV- and HUV-irradiations are similar with respect to the photon energies. However, their respective ratio of $10\, eV$ photons to $7.5\, eV$ photons is different. Figure 4.27 compares a DUV-treated and HUV-treated AC sample. Both samples

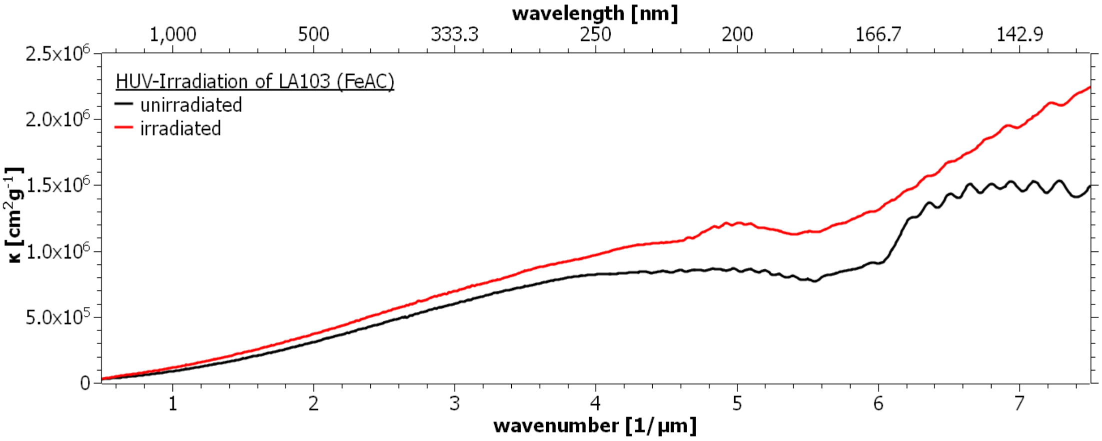

Figure 4.26: LA103 ($0.53 \cdot 10^{17}\, eV cm^{-2}$), an iron-containing AC sample irradiated with HUV photons at the IFK.

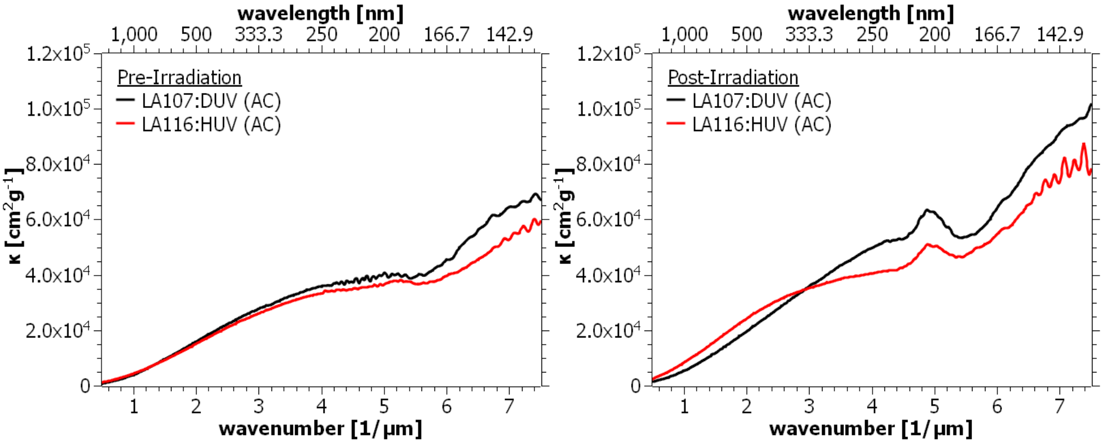

Figure 4.27: LA116 and LA107, thin iron-free AC sample irradiated with HUV and DUV photons respectively. The left side shows the unirradiated samples, the right side shows them after their respective irradiation.

show the emergence of a band at roughly $5\,\mu m^{-1}$ that are roughly equal in size and width. Graphitization seems to take place as well to a similar degree.

4.6 Multi-Harmonics Laser: 90-30nm (XUV)

The energy range that the multiharmonics laser covers ($20 - 60\,eV$) corresponds to the peak wavelengths of black bodies of temperatures from $30000\,K$ to more than $60000\,K$. O-stars have temperatures of the same range (Weidner and Vink, 2010). In fact any hot medium like the warm atomic and ionized medium and especially the hot ionized medium (Ferrière, 2001) is a source for photons of that range. Furthermore, photons in that energy range are emitted when the positively-charged ions of the simpler elements like C, N and O recombine (Tielens, 2006).

Furthermore, photons of this range are emitted by black holes and active galactic nuclei affecting their circum-nuclear gas (Green et al., 2015).

4.6.1 Iron-Free Materials

The deconvolution parameters of the iron-free samples can be found in Table 4.6.

AC: LA59, LA115

LA59 (Figure 4.28) was a quite thick sample ($222\,nm$) and thus its processing needs to be regarded as inhomogeneous. The irradiation caused it to become too opaque in the far UV, thus only the information up to $6\,\mu m^{-1}$ are reliable.

A strong increase and redshift of the $\pi \rightarrow \pi^{\star}$-transition band can be observed. Furthermore, the later opacity of sample indicates that the $\sigma \rightarrow \sigma^{\star}$ has grown a lot. This hints at a strong graphitization of the entire sample, as both new σ- and π-bands have formed. Additionally,a new band at approximately $4.89\,\mu m^{-1}$ emerged.

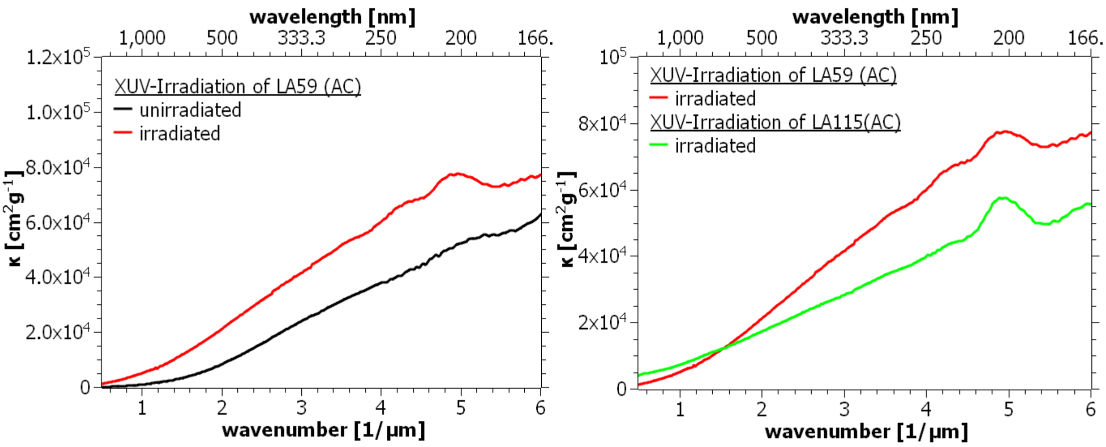

Figure 4.28: LA59 ($12 \cdot 10^{16}\, eV cm^{-2}$), an iron-free AC sample irradiated with XUV photons. The right graph shows LA59 before and after the irradiation. In the left graph, LA59 and LA115 are compared.

LA115 (Figure 4.29) is a thin sample of $17\,nm$ thickness and was used to determine whether the effect of secondary emission was of any importance.
The $\pi \rightarrow \pi^{\star}$ band has increased in strength moved further blue. Although this is not completely unreasonable, it is more physical to assume, that the $\pi \rightarrow \pi^{\star}$-band changed less than it did in the fit. The spectrum itself does not show any significant increase in the $\pi \rightarrow \pi^{\star}$-region, but in the $\sigma \rightarrow \sigma^{\star}$-region there is a significant increase, whose flanks were not clearly-defined and thus added to the

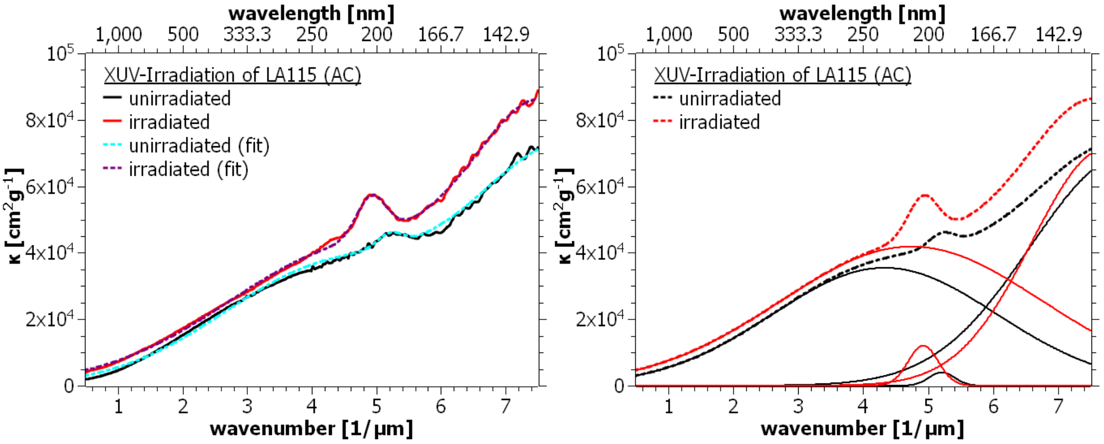

Figure 4.29: LA115 ($3.4 \cdot 10^{19}\, eV cm^{-2}$), an iron-free AC sample irradiated with XUV photons.

$\pi \rightarrow \pi^{\star}$-band by the fitting routine. The $n \rightarrow \sigma^{\star}$-transition of oxygen vanished upon irradiation. An additional band formed at $4.92\, \mu m^{-1}$.

HAC: LA60, LA108

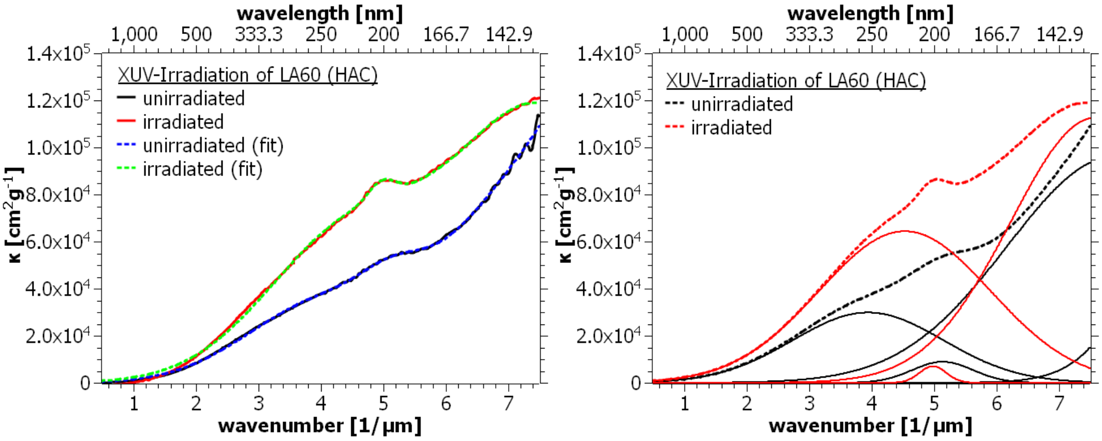

Figure 4.30: LA60 ($81 \cdot 10^{16}\, eV cm^{-2}$), an iron-free HAC sample irradiated with XUV photons.

The XUV-Irradiation of LA60 increased its absorbance in the region of the $\pi \rightarrow \pi^{\star}$-band, indicating graphitization. The $\pi \rightarrow \pi^{\star}$-transition band shifted further to the blue and became stronger and wider. The $\sigma \rightarrow \sigma^{\star}$-band shifted to the red and became narrower — according to the fit parameters (Table 4.6). The σ-band increased its strength a little bit, but this probably served to compensate for the narrowing of the band. Additionally, a distinct band at $4.99\, \mu m^{-1}$ emerged.

LA108 (Figure 4.31) became more graphitic, which means that the remaining aliphatic regions connected to form aromatic sites. The π-band region nearly

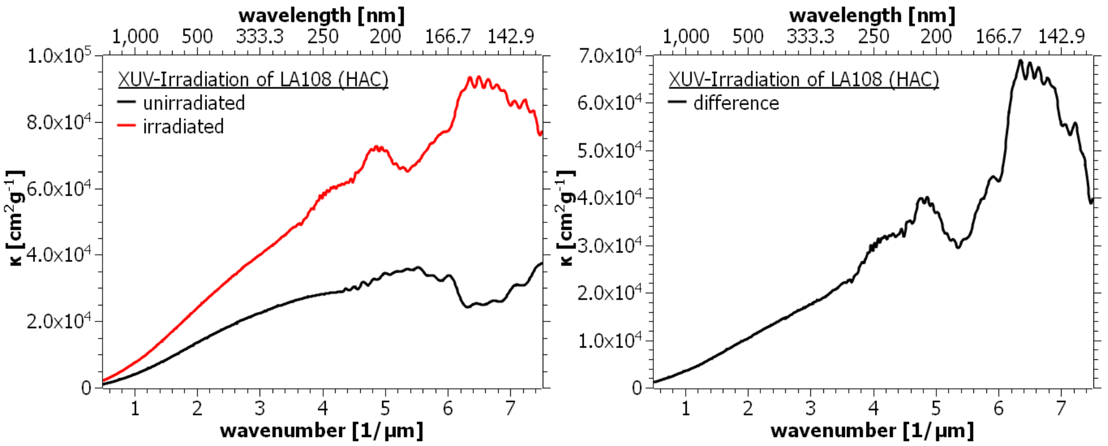

Figure 4.31: LA108 ($37 \cdot 10^{16}\, eV cm^{-2}$), an iron-free HAC sample irradiated with XUV photons.

doubles in strength. The σ-band seems to experience a red-shift but grows too, which is a sign that new connections are formed. Aside from the formation of a distinct band at roughly 5 inverse micron, a shoulder forms close to $4\, \mu m^{-1}$.

	unprocessed			*processed*		
Band	ν_0 $[\mu m^{-1}]$	FWHM $[\mu m^{-1}]$	rel. Ampl. [1]	ν_0 $[\mu m^{-1}]$	FWHM $[\mu m^{-1}]$	rel. Ampl. [1]
XUV: HAC						
LA60						
$\pi \rightarrow \pi^\star$	3.95	2.83	0.26	4.53	3.23	0.56
$O_2 : n \rightarrow \sigma^\star$	5.14	1.14	0.08			
$(\pi \rightarrow \pi^\star)_{OLC}$				4.99	0.50	0.06
$\sigma \rightarrow \sigma^\star$	7.90	4.95	0.84	7.59	3.21	0.99
XUV: AC						
LA115						
$\pi \rightarrow \pi^\star$	4.33	4.07	0.49	4.75	4.76	0.58
$O_2 : n \rightarrow \sigma^\star$	5.21	0.46	0.05			
$(\pi \rightarrow \pi^\star)_{OLC}$				4.92	0.54	0.17
$\sigma \rightarrow \sigma^\star$	8.06	3.49	0.96	7.75	2.71	0.99

Table 4.6: This table shows the deconvolution parameters of the samples that were irradiated with the multiharmonics laser ($20 - 60\, eV$) at the IOQ.

4.6.2 Iron-Containing Materials

FeAC: LA102

Sample LA102, a relatively thick sample with $17\, nm$, showed graphitization and the emergence of new bonds as well, seen by the simultaneous rise of the $\sigma \rightarrow \sigma^\star$-

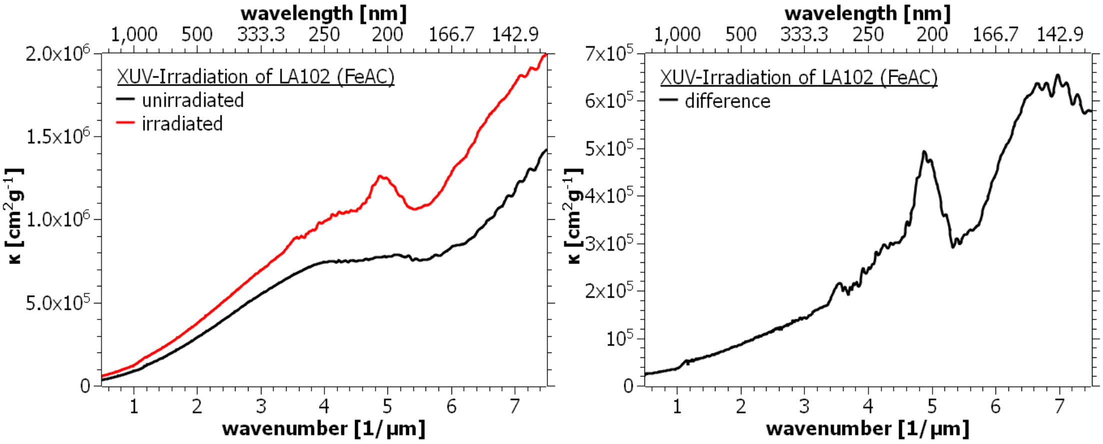

Figure 4.32: LA102 ($25 \cdot 10^{16}\, eV cm^{-2}$), an iron-containing AC sample irradiated with XUV photons.

band and the $\pi \rightarrow \pi^{\star}$-band. A band close to 5 per micron emerges as well. The irradiation apparently caused aliphatic regions to become aromatic.

FeHAC: LA43, LA104

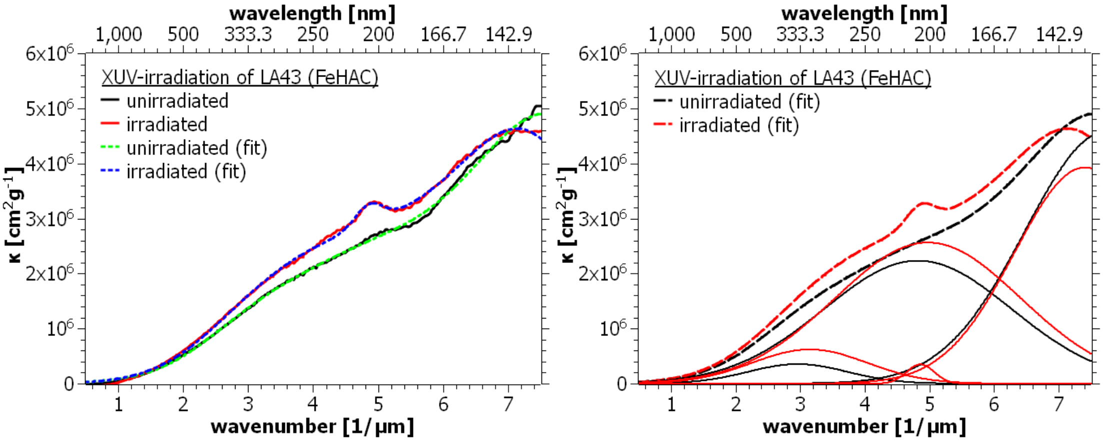

Figure 4.33: LA43 ($9.3 \cdot 10^{16}\, eV cm^{-2}$), an iron-containing HAC sample irradiated with XUV photons.

Upon irradiation a band emerged at $4.87\, \mu m^{-1}$ in LA43 (Figure 4.33, Table 4.7) at $4.86\, \mu m^{-1}$. The deconvolution revealed another peak around $3\, \mu m^{7}-1$, which could either be a graphite plasmon (Falke et al., 1995) or an iron plasmon (Ordal et al., 1983) — or a superposition of both that cannot be resolved. However, this plasmon grows in strength which indicates that its graphitic component increased. Accordingly, $\pi \rightarrow \pi^{\star}$-band shifted to higher wavenumbers and its amplitude became stronger, but it nearly kept its width which could be a side effect and artifact of the slightly red-shifted $\sigma \rightarrow \sigma^{\star}$-transition band. The $\sigma \rightarrow \sigma^{\star}$-transition band area did not change significantly, which indicates that only very few new bonds between the aromatic sub-units had been formed. It can be assumed that the processing mostly affected the already established bonds.

There are two possible, not mutually exclusive explanations for the low degree of additional graphitization: Firstly, iron-containing samples produced under a hydrogen atmosphere tend to have a lower carbon to iron-ratio, because some of the carbon has formed volatile compounds with the hydrogen and thus did not stick to the substrate. Secondly, iron-containing samples have a generally higher degree of graphitization to begin with, as there is graphitic carbon that has condensed around the iron granules. Apparently the graphitic areas are hardly affected by the irradiation and the photo-electrons emitted from the iron granules.

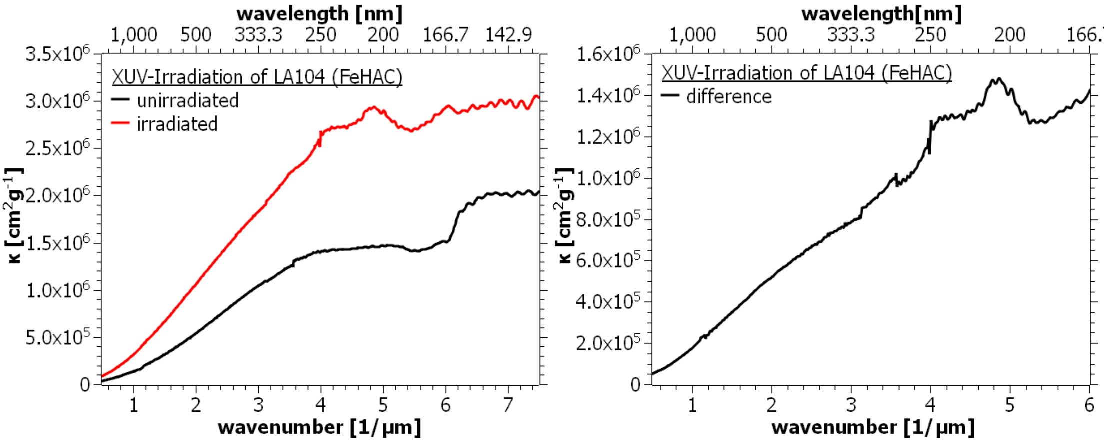

Figure 4.34: LA104 ($24 \cdot 10^{16}\, eV cm^{-2}$), an iron-containing HAC sample irradiated with XUV photons.

In LA104 (Figure 4.34), a relatively thick sample with $9\, nm$ with respect to the penetration depth of the XUV, graphitization took place. The absorption coefficient in the region of the π-band nearly doubled. A band near $5\, \mu m^{-1}$ emerged as well.

	unprocessed			*processed*		
Band	ν_0 $[\mu m^{-1}]$	FWHM $[\mu m^{-1}]$	rel. Ampl. [1]	ν_0 $[\mu m^{-1}]$	FWHM $[\mu m^{-1}]$	rel. Ampl. [1]
XUV: FeHAC						
LA43						
graphite-plasmon	2.96	1.81	0.07	3.15	2.10	0.12
$\pi \rightarrow \pi^\star$	4.82	3.42	0.44	4.98	3.38	0.51
$(\pi \rightarrow \pi^\star)_{OLC}$				4.86	0.50	0.07
$\sigma \rightarrow \sigma^\star$	7.75	2.99	0.91	7.40	2.57	0.78

Table 4.7: The table shows the deconvolution parameters of LA43.

Similar to DUV and HUV, the emergence of a new band at roughly $5\,\mu m^{-1}$ can be seen. The amplitude of the band is consistent with the amplitudes for comparable materials irradiated with DUV and HUV. Graphitization takes place too, if the sample is sufficiently thick.

4.7 Synchrotron: 2.5nm (X)

X-rays of $500\,eV$ are emitted by super hot plasma with temperatures above $10^6\,K$ and are associated with super novae and super novae remnants (Ferrière, 2001). Furthermore, soft X-rays with energies around $500\,eV$ are emitted by T Tauri stars (Güdel et al., 2007).

The samples were irradiated at the beam line SEXTANT of the French synchrotron SOLEIL. The samples were irradiated in a chequerboard-like manner: spots of $100\,\mu m \times 100\,\mu m$ were irradiated one-by-one. The spacing between the spots in both dimensions was $100\,\mu m$.

After the samples had been irradiated, they showed coloured spots on the substrate. These are due to the formation of F-centres in the CaF_2-substrate. Similar effects have occasionally been found after the irradiation with DUV. The effects of their formation are only of significance in the VIS, were they can be eliminated easily.

However, the chequerboard-like irradiation of the X-irradiated samples leads — although counter-intuitive — to a relatively uniformly processed sample. This is obvious with respect to depth, but not for the area between the obviously-irradiated spots. The penetration depth of $500\,eV$ is around $300\,nm$ for a compact material. The distance between the irradiated areas is $100\,\mu m$. However, the material is not compact, but very fluffy. According to previous investigations in the laboratory group of Dr. Jäger, the filling factor is significantly less than ten percent — even down to one percent. Thus the penetration depth of any secondary photons and electrons that are emitted orthogonally to the direction of incidence of the $500\,eV$-photons, can be multiplied by a factor of 100. This yields an effective penetration depth of up to 30 micron. Therefore we can assume, that the material is more uniformly processed than expected. This in turn justifies to spectroscopically measure an area larger than one irradiated spot without the need for corrections for the supposedly unprocessed areas.

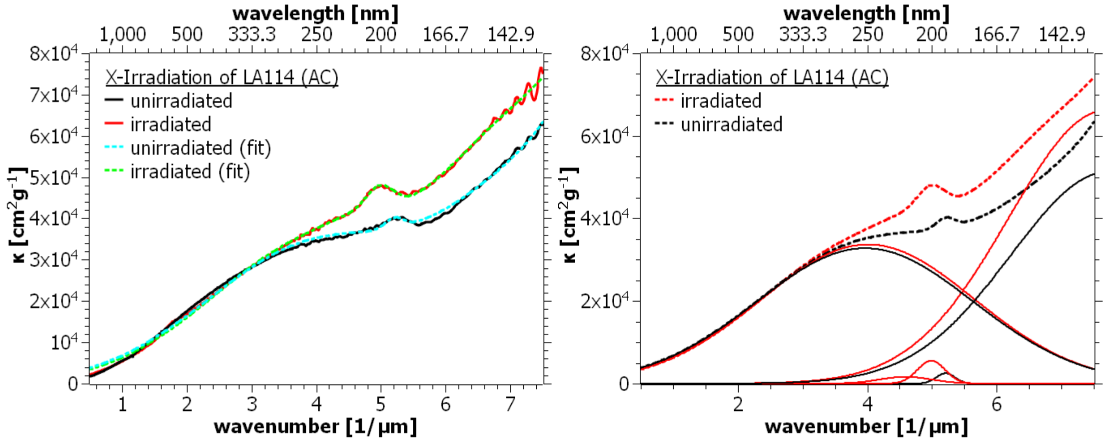

Figure 4.35: LA114 ($1.9 \cdot 10^{21}\, eV cm^{-2}$), an iron-free AC sample irradiated with X photons at SOLEIL.

4.7.1 Iron-Free Materials

AC: LA114

The $\pi \rightarrow \pi^\star$ is not significantly affected by the irradiation. A very small, but broad band around $4.6\, \mu m^{-1}$ is created by the fitting routine. However, it could be an artefact of the fitting routine. The $n \rightarrow \sigma^\star$-band caused by chemisorbed oxygen, vanishes or is at least masked. The $\sigma \rightarrow \sigma^\star$-transition becomes stronger, meaning the number of connections between the structural sub-units has increased. Additionally, a distinct band at $4.99\, \mu m^{-1}$ emerged.

HAC: LA112

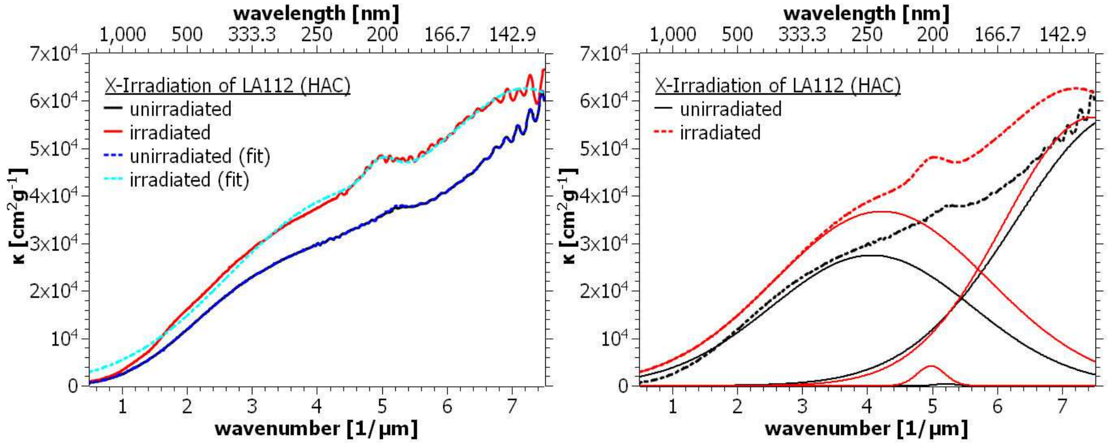

Figure 4.36: LA112 ($1.9 \cdot 10^{21}\, eV cm^{-2}$), an iron-free HAC sample irradiated with X photons at SOLEIL.

The $\pi \rightarrow \pi^\star$-band does not increase according to the fit parameter. However, the absorbance in that area clearly rises. The increase of the strength of that band is masked by the similarly increased $\sigma \to \sigma^\star$-band. Its increase can be explained by the loss of hydrogen and the sub-sequent connection of briefly unbound carbon atoms at the edges of the aromatic units and aliphatic regions. Some of the aliphatic regions seem to have furthermore turned into aromatic units or were integrated into the already-existing ones, as it can be seen by the shift of the $\pi \to \pi^\star$ transition band. Additionally, a distinct band has formed around $4.98\,\mu m^{-1}$.

	unprocessed			*processed*		
Band	ν_0 $[\mu m^{-1}]$	FWHM $[\mu m^{-1}]$	rel. Ampl. [1]	ν_0 $[\mu m^{-1}]$	FWHM $[\mu m^{-1}]$	rel. Ampl. [1]
X: AC						
LA114						
$\pi \to \pi^\star$	3.97	3.93	0.52	4.01	3.87	0.54
$O_2 : n \to \sigma^\star$	5.21	0.34	0.03			
$(\pi \to \pi^\star)_{OLC}$				4.99	0.50	0.09
$\sigma \to \sigma^\star$	7.74	3.58	0.81	7.69	3.54	1.06
X: HAC						
LA112						
$\pi \to \pi^\star$	4.07	3.63	0.44	4.23	3.88	0.59
$O_2 : n \to \sigma^\star$	5.21	0.34	0.01			
$(\pi \to \pi^\star)_{OLC}$				4.98	0.50	0.07
$\sigma \to \sigma^\star$	7.95	3.91	0.92	7.48	3.23	0.91

Table 4.8: This table shows the fit parameter the deconvolution has delivered for the X-irradiated samples.

In Figure 4.37, X-irradiated HAC and AC samples are compared. While both samples, when unprocessed, are quite different, the processing caused both samples to become similar. However, in the case of the HAC sample, the irradiation caused a more efficient graphitization than for the AC sample. This should come to no surprise, HACs in general have a more aliphatic character and thus offer more sites to be graphitized than samples that are already more aromatic. For both materials it should be noted that the $\sigma \to \sigma^\star$-bands have become stronger, too. That is caused by an increased number of (aliphatic) links between the aromatic sub-units. However, the increase of that band is more significant for the AC sample than for the HAC sample. This indicates that the new structures that formed in the HAC were preferably aromatic in nature. In the AC they can be considered to have a more aliphatic character. This difference can be explained by their configuration before the processing. The number of bonds of the carbon atoms with each other within the AC was already more determined than for the HAC. But, since the HAC lost hydrogen in the course of the process, more possible connections and partners became available, so that the carbon atoms can more easily bind to more than only one other atom, increasing the chance of creating new or expanding already existing aromatic structures.

Interestingly, both processes, although acting on different initial conditions, cause a distinct band around 4.95 μm^{-1} to emerge.

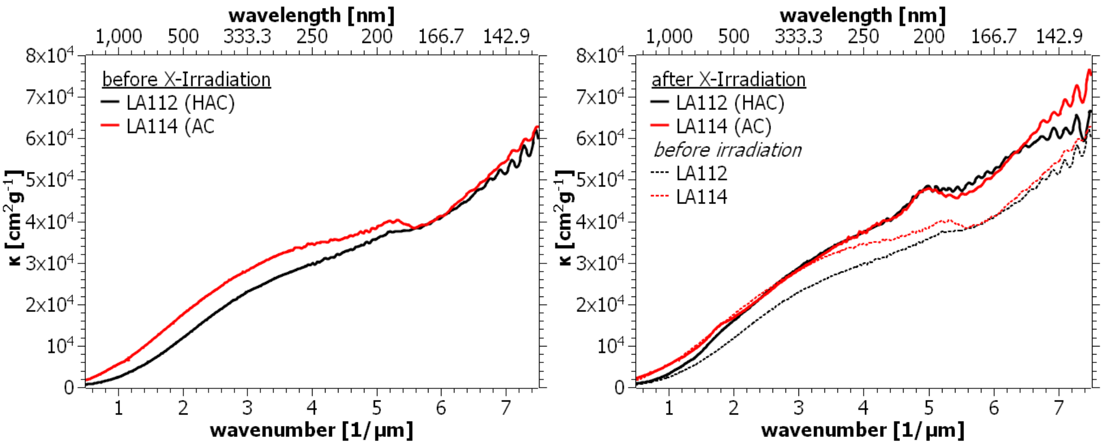

Figure 4.37: The right graph shows the absorption spectra of both LA112 and LA114 before the irradiation at SOLEIL. The thick curves on the right graph shows their spectra after the irradiation with 500 eV photons. The dashed lines are the spectra of the unprocessed samples for comparison.

4.7.2 Iron-Containing Materials

FeAC: LA113

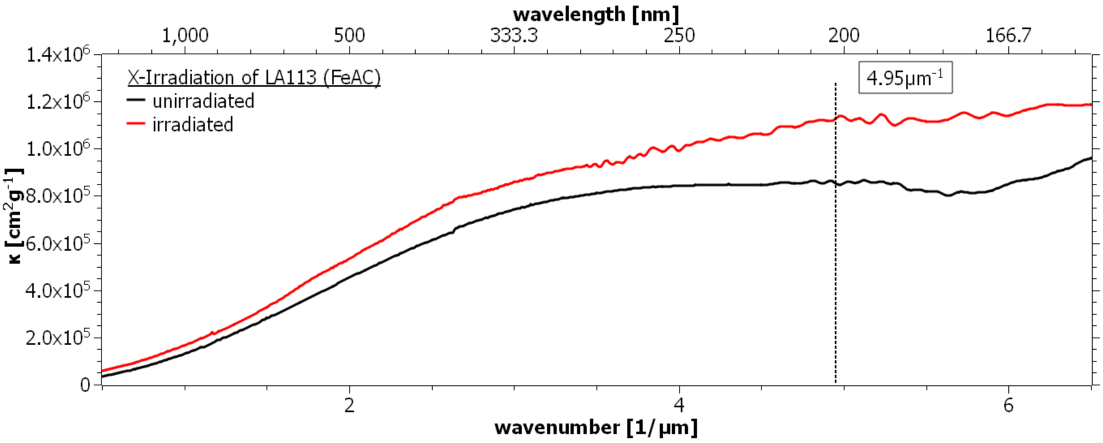

Figure 4.38: LA113 ($1.9 \cdot 10^{21}\, eV cm^{-2}$), an iron-containing sample irradiated with X photons.

Upon irradiation, LA113 (Figure 4.38) became very opaque in the region around the $\sigma \rightarrow \sigma^{\star}$-transition, leaving the spectrometer with a signal akin to noise.

Thus the information of the spectrum beyond roughly $6\,\mu m^{-1}$ was unreliable. This lack of information makes the deconvolution more ambiguous too. However, the absorbance of the $\sigma \rightarrow \sigma^\star$ has increased considerably, meaning that more links between the aromatic sub-units have formed. The increase of the $\pi \rightarrow \pi^\star$-band is one order of magnitude higher than for comparable iron-free samples. The big graphitic layers that have formed around the iron grains might act as catalysts and favour the addition of surrounding carbon atoms. Thus the graphitic carbon shells can grow.
Although masked by the increase of the other bands, a band around $4.95\,\mu m^{-1}$ emerges, too, but less pronounced than for comparable iron-free samples.

Similar to the other irradiation experiments with DUV, HUV and XUV, a band at roughly $5\,\mu m^{-1}$ emerges. The irradiated samples without iron did not show any significant graphitization. This is probably due to the long penetration depth of the X-photons. They reach further into the material, where they interact with the atoms and produce secondary energy photons and electrons. Then all lower energy photons that would usually cause graphitization have a higher chance of escaping the material without any interaction.

However, unlike sample LA43 (Figure 4.33), LA113 (Figure 4.38) graphitized significantly as the denser iron granules absorb energy more efficiently than carbon in that energetic region. Furthermore, the already increased amount of graphitic sites favours the formation of more graphitic sites.

4.8 NEXAFS

The irradiation of the following samples was performed by Dr. Eva Kovacevic at the BESSY synchrotron in Berlin. The samples were exposed to the so-called white light, meaning an unfiltered beam whose energy distribution ranges from $2\,eV$-photons to $15000\,eV$-photons. The irradiated spot of $1mm^2$ experienced a flux of $10.8 \cdot 10^{14}\,photons mm^{-2}s^{-1}$.

4.8.1 Reference Samples

One sample, prepared by Dr. Cornelia Jäger in the late 1990s (Jäger, 1999), was used as a reference. The sample, now referred to as CES38 (Figure 4.39), was produced by resistive heating of carbon electrodes under a He atmosphere of $100\,mbar$. For reasons of consistency and in accord with Narayan and Scholvin (2005), all bands whose center lies between $289\,eV$ and $310\,eV$, are considered sp^3-related, all those whose center lies below $289\,eV$ are considered sp^2-related —

Orbital	**Energy**	
$C1s_{(C=CH)} \rightarrow \pi^{\star}$	284.5-285.11	sp^2
$C1s_{(C=C)} \rightarrow \pi^{\star}$	285.28	sp^2
$C1s_{(C\equiv C)} \rightarrow \pi^{\star}\dagger$	285.9-286.0	sp^1
$C1s_{(C=O)} \rightarrow \pi^{\star}$	286.57-288.55	sp^2
$C1s_{(C-H)} \rightarrow \sigma^{\star}$	287.11-287.68	sp^3
$C1s_{(C-H)} \rightarrow \sigma^{\star}$	287.91-288.66	
$C1s_{(C-C)} \rightarrow \sigma^{\star}\ddagger$	289.3	
$C1s_{(C-C)} \rightarrow \sigma^{\star}$	291.0-293.3	

Table 4.9: The values and assignments of the bands found in NEXAFS spectra were mainly taken from Dhez et al. (2001). Those assignments marked with † were taken from Ravagnan et al. (2006) and Lenardi et al. (1999). ‡ marks Laikhtman et al. (2000).

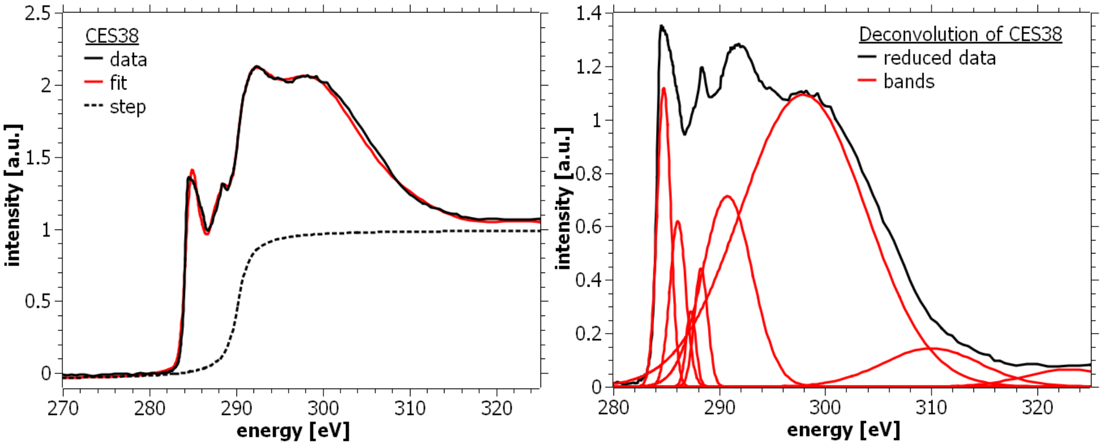

Figure 4.39: The graphs show the deconvolution of CES38, a carbonaceous sample produced by resistive heating of carbon electrodes under a 100 $mbar$ He atmosphere. Th left image shows the original data, its fit and the step-function used for the fit. The right hand image shows the original data reduced by the step, and the bands the fit consists of.

including sp^1 .

For the deconvolution of the reference sample, a manual fit followed by a Monte-Carlo-like exploration of the surrounding parameter space, was performed. The deconvolution parameter can be found in Table 4.10.

The sp^2/sp^3-ratio of CES38 has been measured by Dr. Jäger in the past, and determined to be 76%. The HRTEM analysis revealed that the internal structure of the grains was onion-like. An HRTEM image of CES38 is shown in Figure 4.40

4.8.2 Processed Samples

The decomposition of the NEXAFS samples is shown in Table 4.11.

Hybridization	**CES38**		
E (eV)	284.77		290.77
FWHM (eV)	1.50		5.53
A (arb. units)	1.78		4.15
	286.09		297.94
	1.76		13.89
	1.15	sp^3	16.04
	287.32		310.01
sp^2	1.07		10.96
	0.31		1.63
	288.28		323.04
	1.47		9.88
	0.69		0.68
$\sum I_{sp^2}$	3.93	$\sum I_{sp^3}$	22.5
$\frac{\sum I_{sp^2}}{\sum I_{sp^3}} =$	0.175		

Table 4.10: The table displays the deconvolution parameters of CES38, a sample produced by resistive heating of carbon electrodes under a $100\,mbar$ He atmosphere.

Generally speaking, the amount of sp^2-sites increases for all three samples. In the case of the iron-containing sample, the increase is remarkably strong, whereas the other two samples increase their relative amount of sp^2 only slightly. This is in accordance with the irradiation results of DUV, HUV, XUV and X, where the absolute increase of the π-band is two orders of magnitude higher than for the HAC and AC samples.

Upon white light irradiation the iron-containing AC sample LA23 (Figure 4.42) has released hydrogen and oxygen, and increased its aromaticity , as the sp^2-related band at 284.97 increases its strength and moves towards the position of the sp^2-band of the AC sample LA37 (Figure 4.44). The iron-free AC sample LA37 increases its aromaticity, too. The hydrogen-free sp^2-bands of all samples become wider, meaning The sp^2-bands in the HAC-material split into two bands. The original band at $284.88\,eV$ is caused by $C1s_{(C=CH)} \rightarrow \pi^\star$. This band remains, but loses strength to a pure sp^2-carbon band $C1s_{(C=C)} \rightarrow \pi^\star$. This is consistent with the dehydrogenation observed in the UV-spectra.

Due to exposure to air, all samples chemisorb oxygen and thus contain oxygen-bearing functional groups such as $C{=}O$ and $C{-}O{-}$. For all samples the amount of oxygen decreases upon white light irradiation. For LA23 (FeAC) the band at $288.29\,eV$ ($288.61\,eV$) decreases visibly in the spectrum. In the decomposition it keeps its strength, but becomes wider, which could be considered to be an artifact of the decomposition process. For LA37 (AC) the oxygen peak vanished. In

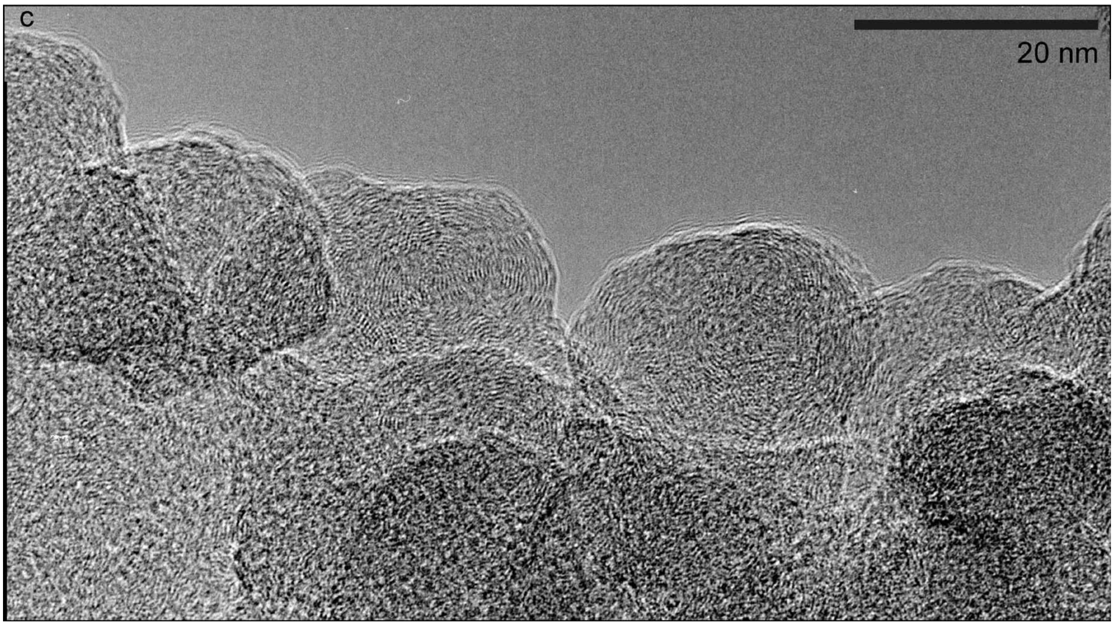

Figure 4.40: The image shows an HRTEM image of CES38, an onion-like material produced by resistive heating of carbon electrodes under a $100\,mbar\ He$ atmosphere. This material has an sp^2-content of 76%.

the HAC sample LA38 (Figure 4.45) the oxygen-related band cannot be identified clearly. The only candidate for oxygen could be the band at $288.7\,eV$ which vanishes upon irradiation. The NEXAFS spectrum around the oxygen edge, however, shows that the amount of oxygen decreases (Figure 4.43). This is consistent with the findings in the UV-spectra where the oxygen-band at $5.21\,\mu m^{-1}$ vanishes too.

We also see a rise in the strength of the sp^3-related, i.e. σ-bands, except for the iron-containing sample. This could be accounted for by the loss of oxygen. The increase of the sp^3-related area can partially be explained by the formation of bent graphene layers as depicted in Figure 4.41. The bent structure forces their non-binding p_z-orbitals into a position where the entire geometry tends to resemble a sp^3-configuration resulting in a higher s-character of the π-bond.

The sp^2-content was derived with the help of a highly aromatic reference sample, CES38. Unfortunately its sp^2-content is below 100%. Thus the method mentioned by Narayan and Scholvin (2005) cannot be applied. Instead the sp^2-content was estimated by scaling the samples' ratio of sp^2- and sp^3-bands with the sp^2-content of CES38. The actual values of the sp^2-content might therefore be slightly shifted.

The iron-containing sample shows the lowest sp^2-content of all three samples. But this should come to no surprise: The amount of already bent layers in LA23 is greater than in the other materials. The sp^2-character of the layers decreases, as the curvature increases. The sp^2-content after the irradiation has increased

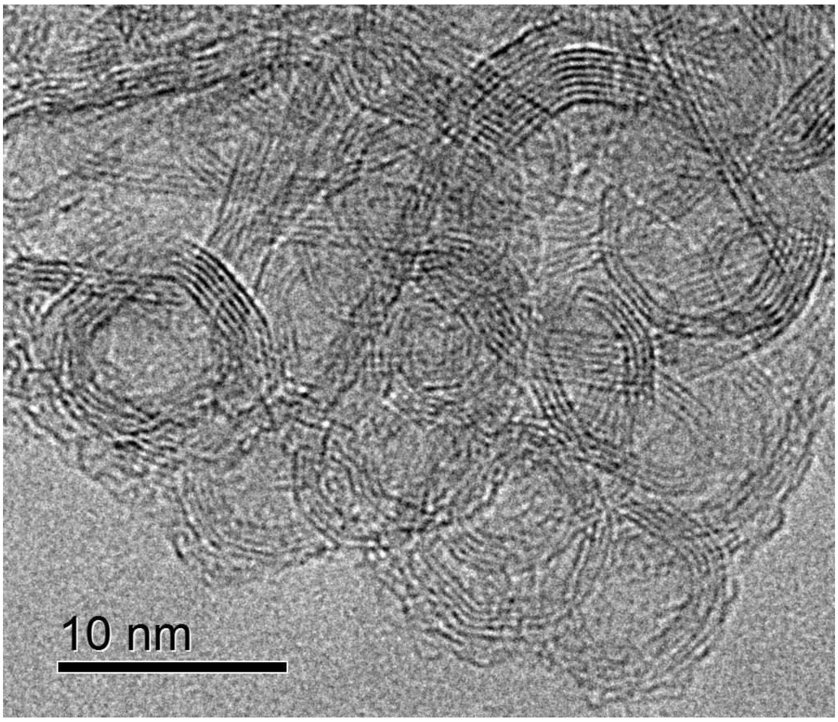

Figure 4.41: The HRTEM image shows an irradiated site of LA38 (HAC). The area is characterized by big, circular structures consisting of several graphene layers.

to nearly 100%. As the layers around the iron-granules grow, the added layers have a bigger radius and thus a smaller curvature. Thus the newly-formed layers are more planar and more sp^2-like. The hydrogen-free and -containing samples increase their sp^2-content to the same degree. This resembles the results of the X-irradiation for LA112 and LA114 (Figure 4.37): Both samples become almost identical.

The white light-irradiated share some similarities with CES38, as their final sp^2-contents are similar. Furthermore, both CES38 (Figure 4.40) and LA38 (Figure 4.41) show onion-like structures. However, the onions of CES38 are fully packed, whereas the onions of LA38 (HAC) consist of onion of fewer layers and which are hollow on the inside. Furthermore, the onions of LA38 are smaller, having diameters of less than $10\,nm$. CES38 is characterized by more ordered onions that seem to be fused with other onion-like structures, resulting in lower curvatures. This is also reflected in the position of the absorption peak, which is $255\,nm$ for CES38 and between $200\,nm$ and $210\,nm$ for the samples irradiated with ArF, DUV, HUV, XUV and X.

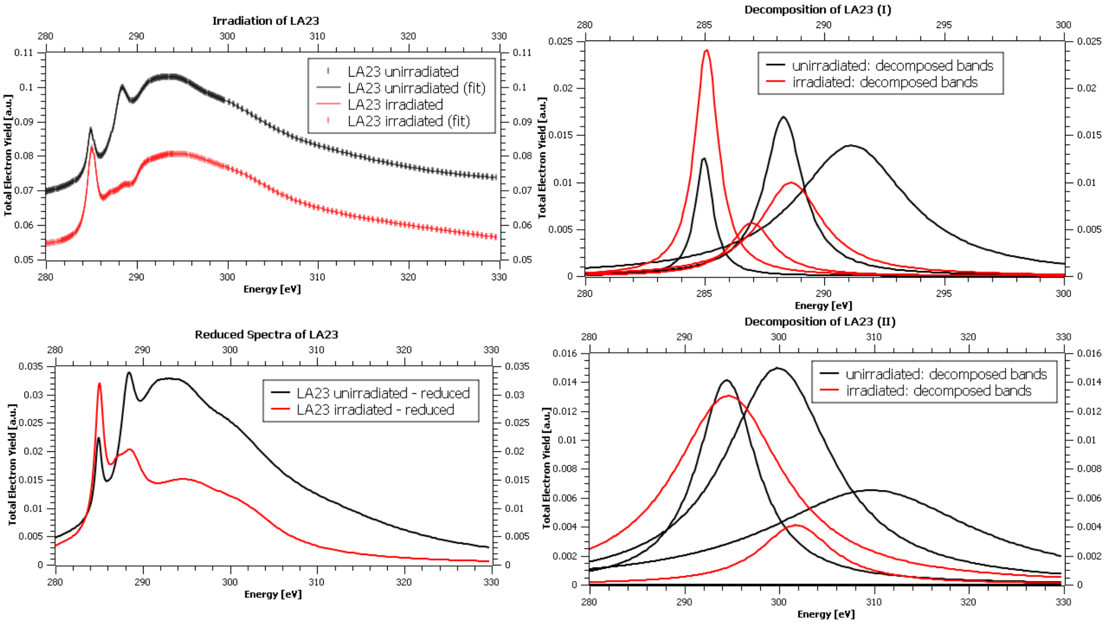

Figure 4.42: The graphs show the deconvolution of LA23, an iron-containing AC sample. The upper left graph displays the measured spectrum of the irradiated and unirradiated samples as well as the fit resulting from the deconvolution. The lower left graph shows the respective fits with the step removed. The upper right graph shows the individual bands that are π-related, the lower one those that are σ-related.

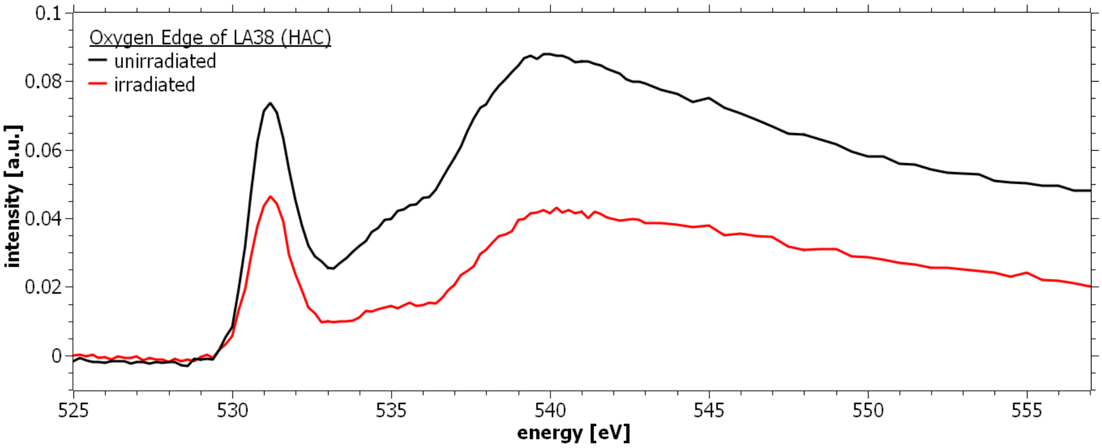

Figure 4.43: The images shows the oxygen edge of LA38 (HAC) before and after irradiation with white light. The oxygen peak decreases as result of the loss oxygen. Both spectra have been shifted downward.

	LA23 (FeAC)		**LA37** (AC)		**LA38** (HAC)	
	unirr.	*irr.*	*unirr.*	*irr.*	*unirr.*	*irr.*
E (eV) **FWHM** (eV) **A** (arb. units)					284.88 1.04 0.73	284.5 0.66 0.33
sp^2	284.97 0.88 0.01	285.07 1.20 0.03	285.11 0.49 0.09	285.06 0.83 0.47		285.06 0.93 0.67
		286.97 2.18 0.01	287.24 0.33 0.12		286.09 1.61 0.39	286.78 2.24 0.80
			287.59 0.62 0.37	287.70 1.10 0.76		
	288.29 1.95 0.03	288.61 3.17 0.03	288.21 0.95 0.46			
$\sum I_{sp^2}$	0.04	0.07	1.04	1.23	1.12	1.80
sp^3			289.37 1.79 0.87	289.29 2.21 1.60	288.70 3.87 2.33	289.00 3.07 1.47
	291.13 5.71 0.08		292.37 5.24 2.45	291.62 2.34 0.62		291.81 4.44 1.45
	294.46 7.68 0.11	294.63 14.09 0.19		293.39 4.40 1.83	293.23 6.26 1.85	295.53 7.54 3.09
	299.88 13.68 0.21		298.79 13.13 3.83	296.70 5.10 1.02	298.32 8.47 2.15	
		301.74 9.22 0.04		301.01 9.10 2.57	304.85 11.51 1.86	302.06 12.62 5.05
	309.70 26.44 0.18				314.31 9.30 0.26	
$\sum I_{sp^3}$	0.58	0.23	7.15	7.64	8.45	11.06
$\frac{\sum I_{sp2}}{\sum I_{sp3}}$	0.07	0.30	0.14	0.16	0.13	0.16
sp^2-content	30%	≈ 100%	61%	69%	56%	69%

Table 4.11: This table shows the decomposition of the NEXAFS analyses of LA23, LA37 and LA38. The first column of every sample contains the values of the unirradiated sample (*unirr.*), the second column shows those for the irradiated sample (*irr.*). The decomposition consists of the central energy of the bands in eV in the first row of every triple, the FWHM in eV in the second one and the area of the band in arbitrary units in the third one.

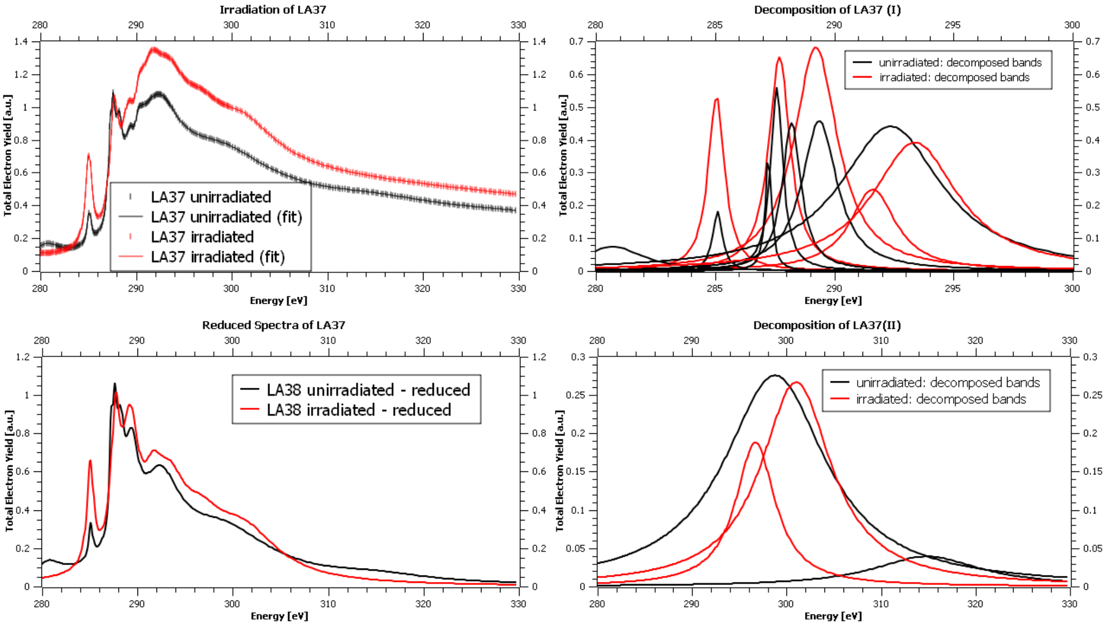

Figure 4.44: The graphs show the deconvolution of LA37, an AC sample. The upper left graph displays the measured spectrum of the irradiated and unirradiated samples as well as the fit resulting from the deconvolution. The lower left graph shows the respective fits with the step removed. The upper right graph shows the individual bands that are π-related, the lower one those that are σ-related.

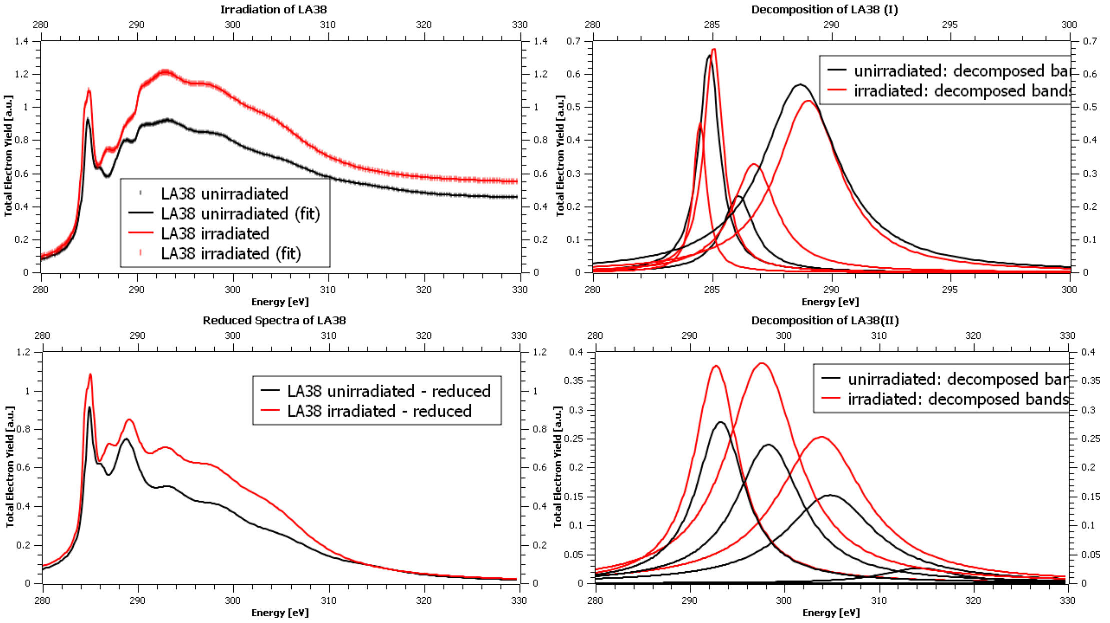

Figure 4.45: The graphs show the deconvolution of LA38, a HAC sample. The upper left graph displays the measured spectrum of the irradiated and unirradiated samples as well as the fit resulting from the deconvolution. The lower left graph shows the respective fits with the step removed. The upper right graph shows the individual bands that are π-related, the lower one those that are σ-related.

Chapter 5

Interpretation

In the following sections, we will interpret the experimental results in detail. But first, a brief introductory summary of the interpretation will be presented first.

The two most prominent changes in the spectra are firstly the graphitization and, even more significant, the formation of a band at around $5\,\mu m^{-1}$. This band is likely caused by the bending of graphene layers. Hence, we will call this particular band **OLC** — onion-like carbon-related band. Rance et al. (2010) have found a relationship for the position of the π-band of carbon nanotubes and their diameter. We calculate the corresponding diameter and try to find sites on the HRTEM images that match this diameter. Furthermore, we will explain how, why and where graphitization and the formation of OLC take place. We will find, that the thickness of the sample plays an important role, as the OLC is mostly formed by photons of an energy higher than needed to break $C{=}C$ and graphitization is caused by photons of less energy. OLC-causing photons usually have a lower penetration depth than graphitizing photons. Therefore graphitization is the dominant process in thick samples, in thin samples it is the formation of OLC.

5.1 The OLC-Band

The interstellar extinction bump at $217\,nm$ has been extensively investigated by Fitzpatrick and Massa (2007). Their findings, with respect to central wavenumbers and widths, are partially displayed in Figure 5.1. While Mennella et al. (1996) and Gadallah et al. (2011) gave rise to a band very close to $217\,nm$ or $4.6\mu m^{-1}$. The band that was given rise to here, is centred around shorter wavelengths ranging from $210\,nm$ to $202\,nm$ (Table 5.1).

In Table 5.1 we present the amplitudes of OLC.

The values have been taken either directly from the deconvolution data, or,

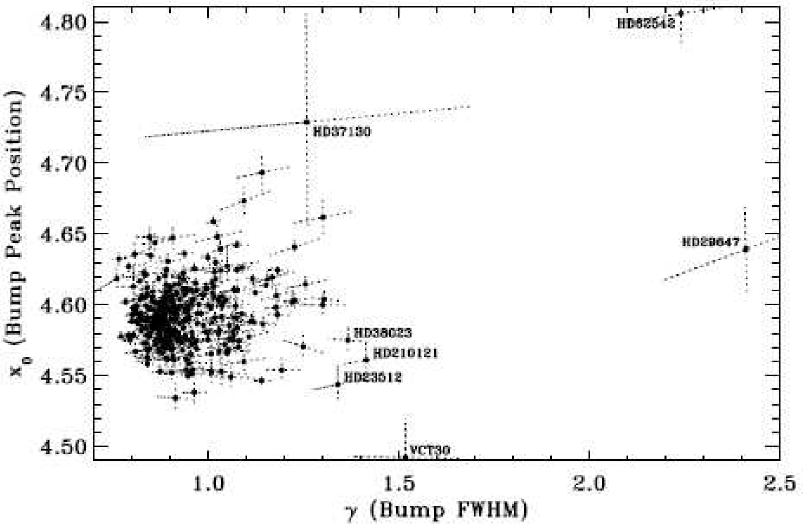

Figure 5.1: The plot shows the distribution of parameters of the interstellar extinction bump of more than 100 lines of sight. Taken from Fitzpatrick and Massa (2007).

Strength of the 5 μm^{-1}-band [$cm^2 g^{-1}$]

Material	**DUV**	**HUV**	**XUV**	**X**
AC	10^4	$5 \cdot 10^3 \ldots 1.5 \cdot 10^4$	10^4	$6 \cdot 10^3$
HAC	10^4		10^4	$6 \cdot 10^3$
FeAC	$< 5 \cdot 10^5$	10^5	$2 - 4 \cdot 10^5$	$< 10^5$
FeHAC	$< 5 \cdot 10^5$	$1.5 \cdot 10^5$		

Table 5.1: The table shows typical values for the maximum strength in $cm^2 g^{-1}$ of OLC.

where no deconvolution was possible, the strength was estimated.

It is interesting to see that for iron-free samples, the maximum value is much lower, by two orders of magnitude, than for those containing iron. The uncertainties of density and thickness do not accumulate and account for a difference that high. However, the iron-containing samples contain more graphitic sites ab initio and the OLC is attributed to bent graphene layers. Thus, it is possible, that the iron-containing samples, as their graphitic sites are already more abundant and bigger, are more efficiently processed than those, where bigger aromatic sites need to be established first.

The smallest dose that was used in the experiments and gave rise to that band, was roughly $10^{17}\,eVcm^{-2}$ for LA43, an iron containing sample. This is six orders of magnitude smaller than Habing's dose ($3 \cdot 10^{23}\,eVcm^{-2}$) and the doses used by Gadallah et al. (2011) and Mennella et al. (1996), but the corresponding photons are in different energy region. The HUV-doses, whose photons are in the same energy range as Habing's photons, are in the same order of magnitude, a millionth

Position of the 5 μm^{-1}-band [μm^{-1}]

Material	**DUV**	**HUV**	**XUV**	**X**
AC	4.89-5.01	4.92-4.95	4.92	4.99
HAC	5.04	4.94		4.97
FeAC		4.84	4.87-4.88	
FeHAC			4.84	

Table 5.2: The table shows the range of the central positions of the newly formed band. All values are given in inverse micrometers.

of Habing's dose.

The order of magnitude of the dose does not seem to play a big role, but the minimum energy of the photons seems to be important. Furthermore, the thickness of the particles and the iron-content decide whether this particular band becomes distinctly visible or is masked by graphitization, which was the case for samples whose thickness was considerably greater than the penetration depth of the photons they were exposed to.

5.2 Changes of the Morphology

In this section, the morphological changes of the materials that experienced irradiation processing, shall be discussed. Aside from descriptive analysis, I try to characterize the investigated sites with numerical values.

The quantities employed are the average length of the layers $\bar{L}$, the maximum length of the layers $\hat{L}$, the average curvature $\bar{C}$, the complexity *comp*, the range of curvatures present C, and the ratio of straight to bent layers *stb*.

Untreated Material

The products of the laser ablation are mostly amorphous. This is reflected by rather short graphene layers. Jäger et al. (2008a) mention mean lengths of around 0.55 nm for samples prepared without hydrogen under helium atmosphere and lengths between 0.4 nm and 0.5 nm for those with hydrogen. This is mostly in good agreement with the lengths found in the samples that are listed in Table 5.3. The largest fibers were found to be between 1.7 nm and 2.7 nm. The ones found here are slightly longer — probably owed to the fact that the samples differ slightly and the analysis of the HRTEM images covered often a bigger area and up to 150 single structures.

It is apparent that there are two types of areas: one that is characterized by short fibers as in AC(LA59) and one with larger fibers (AC(LA46)). This indicates

Sample	$\bar{L}$	$\hat{L}$	$\bar{C}$	*comp*	C	*stb*
	$[nm]$	$[nm]$	$[nm^{-1}]$	[1]	$[nm^{-1}]$	[1]
	untreated					
AC (b)	0.75 ± 0.55	3.45	3.323	0.073	1.5-4.5	2.00
AC (b)	1.07 ± 0.61	3.19	2.275	0.035	1.8-3.2	3.50
AC (np)	1.12 ± 0.85	3.78	2.911	0.178	1.8-4.4	1.36
AC (LA46)	1.39 ± 0.72	3.81	2.261	0.054	0.8-3.6	1.05
AC (LA59)	0.71 ± 0.47	3.15	4.278	0.182	2.5-6.4	1.4
FeAC (LA36)	0.65 ± 0.44	2.03	4.476	0.303	2.8-6.4	1.63
FeHAC (LA28)	1.12 ± 0.55	2.65	3.921	0.230	2.2-6.6	0.58

Table 5.3: The table shows the parameters for different untreated materials that were produced by laser ablation. (b) marks samples that were brushed off the skimmer and experienced rapid cooling by super-sonic expansion, (np) marks material that was collected in the laser ablation chamber of the set-up without experiencing rapid cooling.

that there are rather graphitic regions between more amorphous regions.

The sample AC(np) was extracted from the ablation chamber. It did not experience any rapid cooling and thus has more graphitic character. It is striking that the standard deviation of its length distribution is the largest. For all other samples the deviation is smaller and more alike, indicating there are indeed separated graphitic and amorphous areas. The samples AC(LA46) and AC(L59) that were scratched of the CaF_2-substrate they were deposited on are practically identical to both AC(b) samples. The AC(b) samples are composed of the material that were brushed of the skimmer and experienced only one rapid cooling event. Similarly, the iron-free regions in the FeAC and FeHAC samples behave the same way, there are graphitic and less graphitic regions.

Sample	$\bar{L}$	$\hat{L}$	$\bar{C}$	*comp*	C	*stb*
	$[nm]$	$[nm]$	$[nm^{-1}]$	[1]	$[nm^{-1}]$	[1]
	ArF					
FeHAC (LA14)	1.26 ± 0.74	3.95	3.463	0.22	2.3-5.2	0.4
	1.55 ± 0.72	3.77	2.714	0.110	1.1-4	0.5

Table 5.4: The table shows the parameters for different untreated materials that were produced by laser ablation and subsequently treated by irradiation with an ArF-laser. The applied dose was in the order of magnitude of Habing's dose ($3 \cdot 10^{23}\, eV cm^{-2}$).

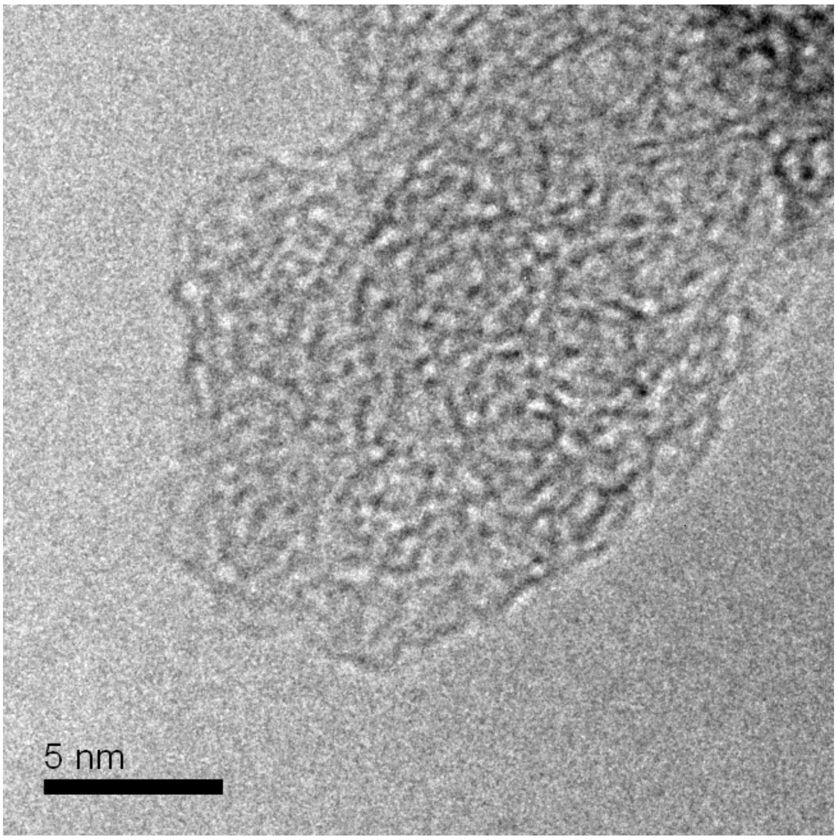

Figure 5.2: The HRTEM image shows an untreated AC sample which is fairly graphitic. The graphitic regions are visible as fibers. Most of them have a length of less than 1.5nm.

Processed Material

The ArF-irradiated samples (Table 5.4) show a slightly increased average length of the graphene layers. However, the maximum length of the longest fiber found is considerably longer than the one found in the untreated FeHAC sample in Table 5.3. This means, that even though there was no graphitization, as the spectra have shown, the aromatic sublayers became more connected forming layers that are longer on average. These connections are of aliphatic nature, for the rise of the π-band was marginal. The *stb* of these samples has decreased, meaning that more of the analyzed layers were considered to be visibly bent and not short and straight. Another sign for weak connections between stable aromatic sub-units.

The DUV-irradiated samples (Table 5.5) have — on average — longer fibers. The fibers from materials practically without hydrogen, FeHAC too, are longer than those that definitely contain significant amounts of hydrogen such as HAC. This is also resembled by the maximum length of the fibers.

The ratio of straight to bent fibers is quite low. This is caused by two effects: The graphene layers bend as a result of being connected to other graphene

Sample	$\bar{L}$	$\hat{L}$	$\bar{C}$	$comp$	C	stb
	$[nm]$	$[nm]$	$[nm^{-1}]$	[1]	$[nm^{-1}]$	[1]
	DUV					
AC (LA96)	3.19 ± 1.39	7.63	2.684	0.137	1.1-4.3	0
HAC (LA39)	1.52 ± 0.85	4.56	2.251	0.052	1.2-3.4	1.13
FeAC (LA25)	2.22 ± 1.29	7.09	3.56	0.242	1.8-5.5	0.09
FeAC (LA98)	2.42 ± 0.98	4.48	3.643	0.230	2.0-5.5	0.03
	2.68 ± 1.22	5.45	2.271	0.133	1.7-3.5	0.08
	3.03 ± 1.71	8.18	3.545	0.248	2.0-5.3	0
FeHAC (LA28)	3.05 ± 1.68	7.46	3.320	0.176	1.6-4.6	0.07
	2.30 ± 1.13	5.04	4.027	0.307	2.0-6.0	0.03
	2.43 ± 0.99	4.74	2.106	0.101	0.7-3.4	0.18

Table 5.5: The table shows the parameters for different untreated materials that were produced by laser ablation and subsequently treated by irradiation with DUV. The applied dose was roughly one order of magnitude smaller than Habing's dose ($3 \cdot 10^{23}\, eVcm^{-2}$).

layers and by turning aliphatic regions into graphitic regions. Secondly, the DUV-photons are quite powerful and manage to break even $C{=}C$-bonds and are thus able to affect the shape of the graphene layers.

Similar to the samples previously mentioned, those that were irradiated with XUV display a growth of their graphene layers. In the HRTEM pictures the presence of big and round structures becomes more dominant. An example can be seen in Figure 5.4. The structures look like dinted circles.

The X-irradiated samples show a growth of the graphene layers as well. Interestingly, the mean curvatures are relatively similar — this might come to no surprise, as the irradiated areas were marked by the formation of F-centres in the underlying substrate. Thus in this case it was rather easy to find and extract the processed area. Therefore we can conclude that the morphological key to the newly formed band can be found in these samples, especially LA114 and LA112, as they show little graphitization in the spectra and a clear band at roughly fiver per micron.

Table 5.3, Table 5.4, Table 5.5, Table 5.6 and Table 5.7 show the set of quantities describing the sites of several processed and unprocessed samples.

Roughly speaking, $\bar{L}$ and stb are a measure for the processing the sample experienced. Unprocessed AC and HAC samples do have shorter average length. The lengths found here are comparable to those found by Jäger et al. (2008b). The general trend is that processed samples have a longer average length than the untreated ones due to graphitization. Furthermore, the stb somewhat describes the analyzed layers in terms of shape: a low stb means that most of the layers

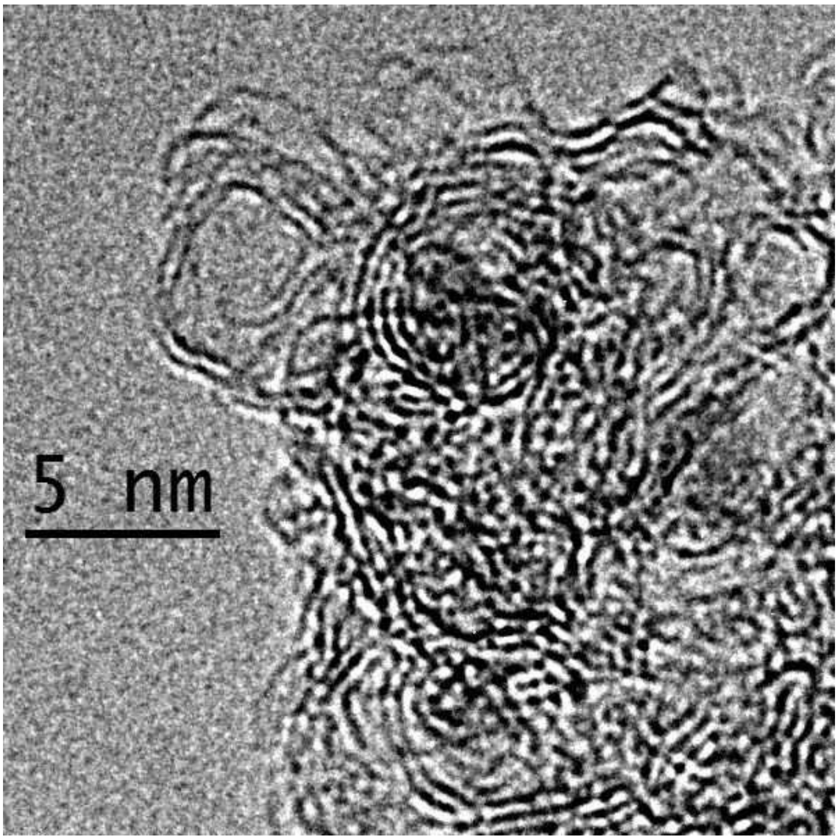

Figure 5.3: The HRTEM image shows an irradiated site of LA98, an iron-containing sample irradiated with DUV. The site consists of long and bent graphene layers that seem to form closed structures.

are bent, whereas a high *stb* means that the majority of the analyzed layers can be considered as straight or un-bent. This quantity is slightly size-dependent as shorter samples of low, but not vanishing curvature are automatically considered to be straight.

Bending usually occurs after processing. Therefore, low *stb* also means that the site experienced processing, whereas a high *stb* means less to no processing.

The quantities used here are not reliable for quantitative analyses. However, in order to show trends, they are sufficient. In section 2.3.4 a detailed explanation for the sources of errors and biases can be found.

In general, the graphitic layers of unprocessed samples containing iron are longer as the iron promotes graphene growth. An explanation for that is given in section 3.3. The short average length of the unprocessed LA36 can be explained by a lack of iron on the particular site.

A general trend of the irradiated samples is the increase of the average length of the graphene layers. Because the method with which the lengths have been derived is not suitable for very strict quantitative statements, no further general

Sample	$\bar{L}$	$\hat{L}$	$\bar{C}$	*comp*	C	*stb*
	$[nm]$	$[nm]$	$[nm^{-1}]$	[1]	$[nm^{-1}]$	[1]
	XUV					
AC (LA59)	2.27 ± 1.28	8.30	2.139	0.076	0.7-4.0	0.43
AC (LA115)	4.23 ± 1.21	6.83	2.283	0.082	1.7-3.1	0
	2.13 ± 1.03	5.92	3.467	0.121	0.7-5.5	0
AC (LA106)	3.19 ± 1.23	5.81	1.694	0.050	0.8-2.9	0.09
	2.55 ± 1.63	8.68	2.293	0.093	1.3-3.8	0.17
	2.74 ± 1.30	7.15	1.987	0.087	0.7-3.6	0.11
HAC (LA108)	5.01 ± 2.57	11.66	2.151	0.093	1.3-3.2	0
	4.31 ± 1.79	8.99	2.027	0.086	1.2-3.3	0
FeAC (LA67)	1.6 ± 0.99	5.12	2.907	0.136	1.1-6.0	0.35
	3.5 ± 1.06	5.64	2.003	0.085	1.3-2.8	0.07
	4.34 ± 2.23	11.81	1.275	0.035	0.5-2.2	0.1
	3.79 ± 1.39	6.90	1.773	0.056	0.7-2.3	0.08

Table 5.6: The table shows the parameters for different untreated materials that were produced by laser ablation and subsequently treated by irradiation with XUV.

trend can be found reliably. However, the average length of the graphene layer of iron containing samples seems to be longer, compared to similarly irradiated samples without iron.

Unfortunately, no other trend than the growth of the aromatic layers can be derived from these quantities by simple statistics. The main reason for the lack of informative values lies in the HRTEM images themselves. Obscured and overlapping structures make it difficult to fully trace the sites. As a consequence, no feature accounting for OLC can be derived from these quantities. If one could have been found, it would have been in LA114 as it did not graphitize and only

Sample	$\bar{L}$	$\hat{L}$	$\bar{C}$	*comp*	C	*stb*
	$[nm]$	$[nm]$	$[nm^{-1}]$	[1]	$[nm^{-1}]$	[1]
	X					
AC (LA114)	2.33 ± 1.33	6.65	2.76	0.188	1.3-4.5	0.21
HAC (LA112)	1.5 ± 0.67	2.94	3.098	0.138	2.2-3.8	0.36
	2.19 ± 1.15	7.43	2.950	0.174	1.6-4.0	0.08
FeAC (LA113)	2.75 ± 1.52	7.00	3.488	0.216	1.8-5.2	0.07
	2.14 ± 0.93	4.44	2.914	0.133	1.1-4.0	0.07

Table 5.7: This table displays mathematically available quantities characterising the processed samples. Each row is the characteristic of only one site. $\bar{L}$ is the average length of a layer in nm, $\hat{L}$ is the longest layer found, $\bar{C}$ is the curvature, *comp* is the complexity, C is the range of average curvature computed in the analyzed site, *stb* is the straight to bent-ratio.

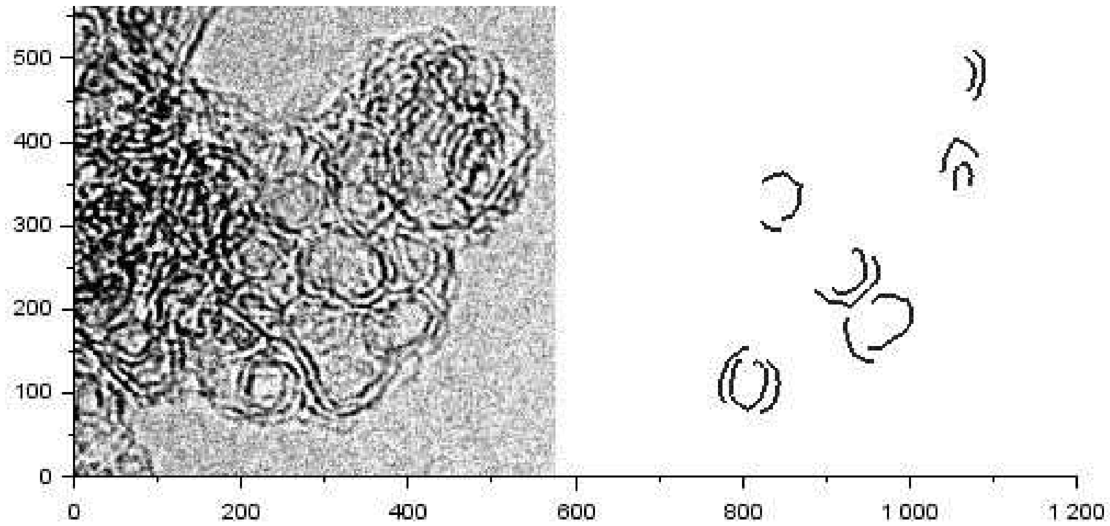

Figure 5.4: This HRTEM picture of LA108 shows an area that was heavily affected by the XUV-irradiation. The left side shows the site, the right part shows the traced paths. The scale is $30\,nm^{-1}$. The graphene layers have grown and connected to form huge, bent layers of about $5\,nm$ in diameter. The structures are analyzed in Figure 5.5.

showed the emergence of OLC. For the other samples exhibiting OLC, as most of them showed graphitization too, the graphitization would have probably masked the feature accountable for OLC.

In many samples, such as LA106 (Figure 5.6), LA108 (Figure 5.4) and LA114 (Figure 5.14), it could be observed that circular and onion-like structures emerged. They are very likely to be responsible for the emergence of OLC. Rance et al. (2010) present an empirical formula to compute the position of the absorption maximum of carbon nanotubes, Equation 1.1. This formula gives a rough idea of the diameter of the curvature needed to produce OLC. This empirical formulae gives $0.73\,nm$ as a result, which, according to Zhao et al. (2004), who have shown that the thinnest carbon nanotube produced as of 2004 has a diameter of 3Å, is reasonable. The curvature of this structure is roughly $2.78\,nm^{-1}$. The mean curvature of LA114 $\bar{C}_{LA114} = 2.76\,nm^{-1}$. As it can be seen in Figure 5.8, the distribution of mean curvatures $\bar{C}$ is rather narrowly distributed around 2.76. Similarly, the curvatures of LA106 (Figure 5.7) and LA108 (Figure 5.5)

Figure 5.12 shows a sample with a similar mean curvature, $\bar{C}_{LA14}$. LA14 has been irradiated with ArF and did not show any OLC-like structure, instead it simply graphitized as expected (Walter, 2013). This is reflected by the rather broad scattering of the mean curvatures. It is also clearly visible, that the graphitized LA14 has less complex structures than LA114. LA112, which experienced some graphitization and the emergence of OLC, is illustrated in Figure 5.10. They

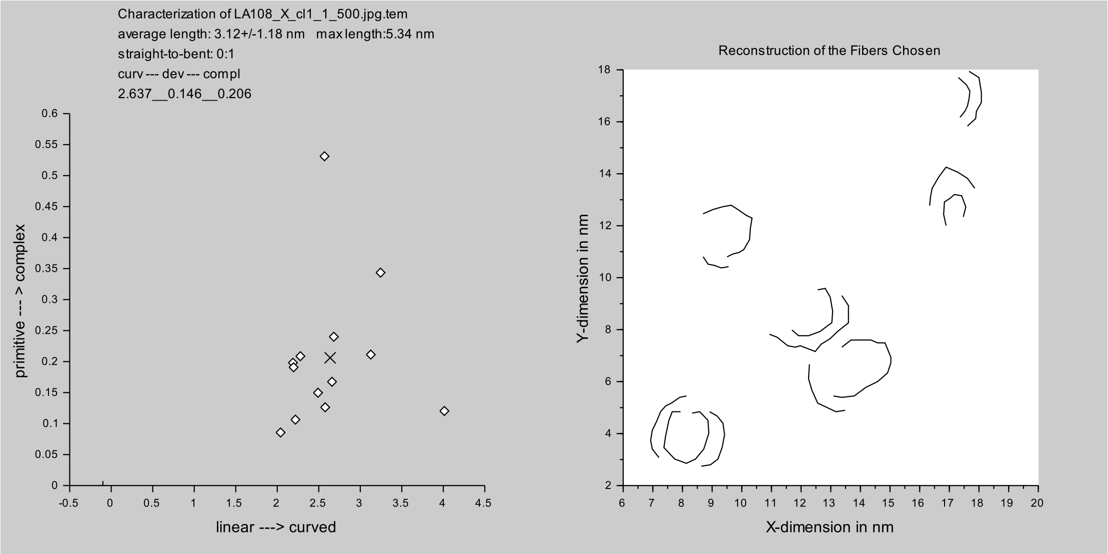

Figure 5.5: The image shows the traced paths of the onion-like structures of LA106 (AC, XUV-irradiated) and their corresponding curvatures, which is illustrated in Figure 5.4. The curvatures are centred around 2.6 nm^{-1}.

became spectroscopically similar after irradiation and thus must have become similar in morphology. Their mean curvature is similarly narrowly distributed around 2.9 nm^{-1}.

Samples like the irradiated LA98, a sample having experienced mostly graphitization, shows a quite high mean curvature.

5.3 Processing Mechanism

All in all, two distinct effects are present.

1. **Graphitization**
2. **Emergence of band at roughly 5 μm^{-1}** (OLC)

However, both processes are not too different from each other — except for that their results differ. In this section I will explain the different manifestations of the photon-carbon interactions. The emergence of a band at roughly 5 μm^{-1} is first seen with the DUV-irradiation, and is present in all other samples that were exposed to photons of higher energy. The spectrum of the D_2-lamp partially overlaps with that of the H_2-lamp. One notices that the DUV-irradiation in general increases the absorption in the π-band region more than HUV-photons do (Figure 4.27), which indicates that more graphitization has taken place in the DUV-irradiated samples. We have also seen that the ArF-photons do not give

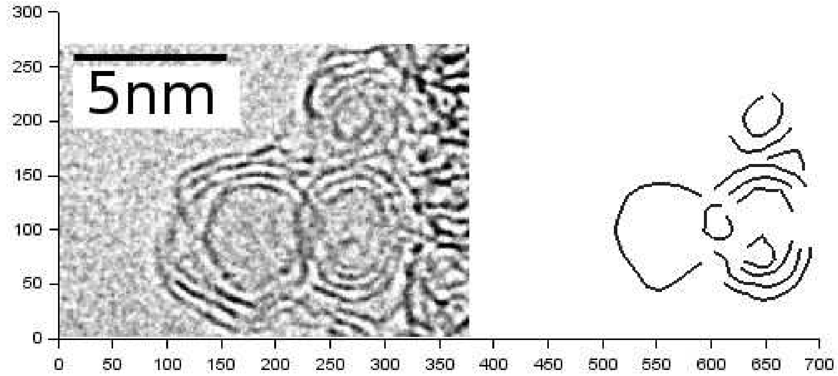

Figure 5.6: The image shows an irradiated site of LA106 (AC). The left side shows the site, the right part shows the traced paths. The scale is $30\,nm^{-1}$. The structures below the length scale are two overlapping onion-like structures that consist of only a few layers. The structures are analyzed in Figure 5.7.

rise to such a peculiar band at $5\,\mu m^{-1}$. Furthermore, we have seen that thinner samples that were DUV-irradiated, experienced less graphitization than those that were thicker (Figure 5.15).

From here we can derive the approximate photon energy that is able to give rise to a band around $5\,\mu m{-}1$. The deuterium lamps contributes mostly $7.5 - 8.0\,eV$ photons, and to a minor degree photons up to $\approx 10\,eV$. As a whole, LA107 which is a thinner sample than LA96, absorbs more higher energy photons ($E > 8\,eV$) than LA96 in relation to their uptake on lower energy photons ($E < 8\,eV$). Hence we can set the threshold, where the formation of the OLC occurs between $8\,eV$ and $10\,eV$. For reasons of practicality, we set the threshold to $9\,eV$, because this energy is just sufficient to break all carbon-carbon-bonds. So far, we know the threshold between general graphitization and the formation of quite well-defined curved structures, that cause the OLC. In order to understand the formation of the defined structures, one needs to understand, how the general photon-induced graphitization process, which can take several routes, works. We limit the photons to energies below $8\,eV$: We start with an arbitrary structure akin to Figure 1.3. We can expect that there are no dangling bonds and that the entire structure is passivated by oxygen and hydrogen. An incident photon, if its energy suffices, may break a bond between a carbon atom and one of the hetero-atoms, creating a dangling bond. Hydrogen, always a terminal partner in the graphitic structures, is expelled from the site. The dangling bond of the carbon atom immediately seeks another partner. It could recombine with any available hetero-atom or it could bind to an adjacent carbon atom with a double or triple bond. Another scenario is that a single bond between two carbon atoms is broken and the activated carbon atoms form double bonds with their remaining partners. By means of that we

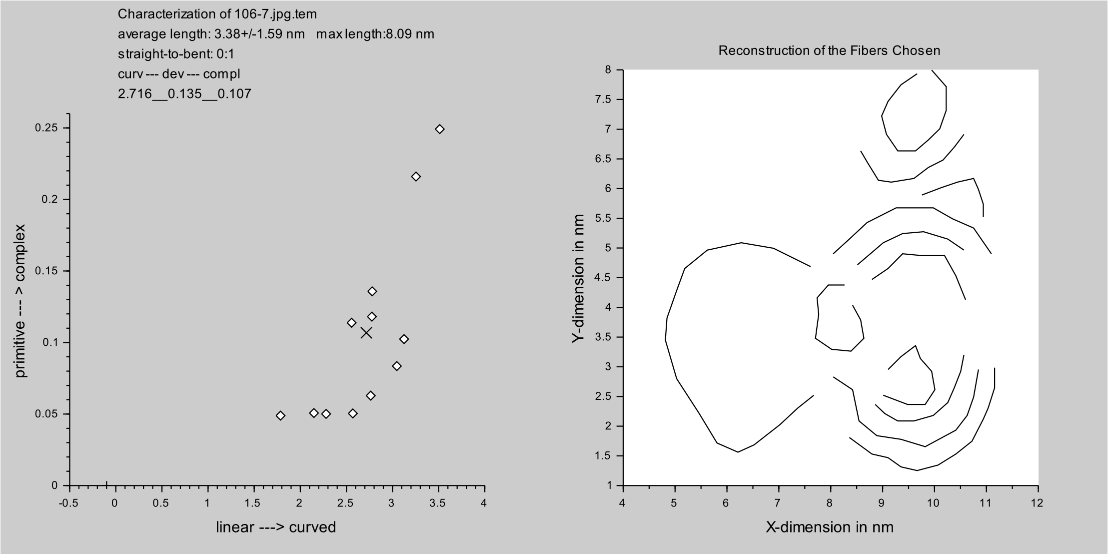

Figure 5.7: The image shows the traced paths of the onion-like structures of LA106 (AC, XUV-irradiated) and their corresponding curvatures, which is illustrated in Figure 5.6. The curvatures are centred around $2.7\,nm^{-1}$.

can explain how new connections between aromatic sub-units are formed and extended. However, there is another important factor: the penetration depth. The penetration depth decreases monotonically with growing photon energy in the range of $1\,eV$ to $10\,eV$. This quantity does not only tell how far photons can penetrate the material, but also how close to each other they are absorbed. A shorter penetration depth means that the photons are absorbed on a shorter path and thus act in closer proximity. The lower energy photons have a relatively wide reach meaning they do not act locally concentrated, but fairly widely distributed. That implies that the photon-carbon interactions are spatially and temporally isolated from another, given that the photon flux is not too high (section 4.3), lest they cause shocks, ablation and sputtering reversing the graphitization (Narayan and Bhaumik, 2015).

The bending of the structures is due to Stone-Thrower-Wales (STW) defects. In order to induce them an energy E^0_{sw} of several electron volts is needed. Kaxiras and Pandey (1988) calculated the minimum value to be $10.4\,eV$, but Zhou and Shi (2003) propose a lower minimum energy of $6.02\,eV$. For carbon nanotubes, they have empirically found the following formula for the defect energy E_{sw} that depends on the radius of the carbon nanotube among other quantities:

$$E_{sw} = E^0_{sw} + ae^{-br} + \frac{c}{r^2} \tag{5.1}$$

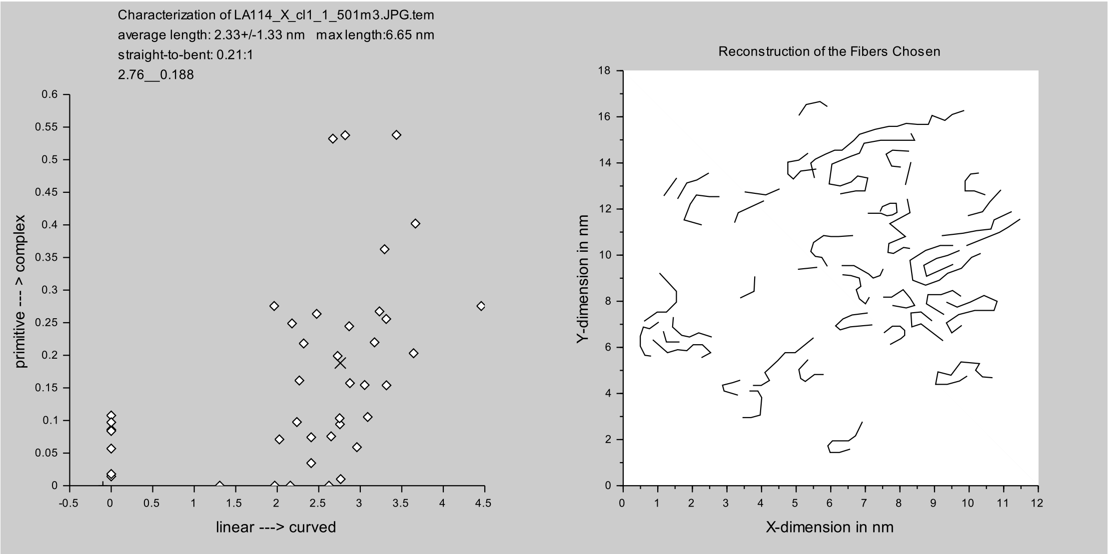

Figure 5.8: This figure shows the result window of the analysis of an HRTEM images of LA114. The right hand side shows the evaluated paths of that site. The left hand side shows a plot of the distribution of the curvature and the corresponding mean complexity. The abscissa (curvature) is in nm^{-1}. The straight structures have a curvature of zero and actually a complexity of zero, too. Random complexity values were assigned to them in the graph to better illustrate their number.The corresponding HRTEM image is Figure 5.9.

Here, a, b, c are parameters that are determined by the geometry and orientation of the carbon nanotube. For their materials they have shown that the formation energy ranges somewhere between $4.6\,eV$ and $7.6\,eV$. However, Kaxiras and Pandey (1988) give activation energies between $8\,eV$ and $12\,eV$, as there are several pathways to Stone-Thrower-Wales defects, which is in good agreement with my estimated threshold of $9\,eV$. Why both graphitization and the formation of curved structures occur under DUV- and HUV-irradiation, is obvious: The DUV contains a lot of photons that can only graphitize, and both the DUV and HUV-photons have energies around the activation energies. However, why can graphitization also be seen, even though to a smaller degree, under XUV and X-irradiation? To answer this question, I will first focus on the X-irradiated samples, especially the AC one, LA114. I will then include additional processes that affect the HAC and FeAC samples. From there I will derive the mechanism for the XUV-irradiated samples. The X-photons of $500\,eV$ have a long penetration depth of around $300\,nm$, which is approximately the thickness of LA114. This sample can hence be considered to have been processed homogeneously with respect to depth. Upon irradiation the initial high energy photon is then broken down into secondary photons and electrons of lower energy by a cascade of events: *Emission of core electrons* The X photons have sufficient energy to knock out a core electron ($1s$). The emitted

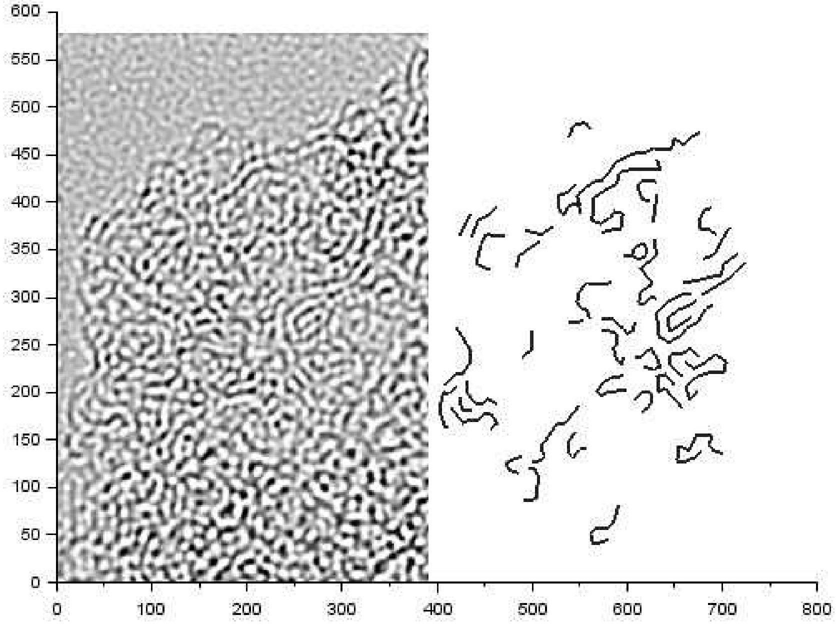

Figure 5.9: The HRTEM image shows the site of LA114 where the data of Figure 5.8 have been derived from. The left side shows the site, the right part shows the traced paths. The scale is $30\,nm^{-1}$.

electrons then have a kinetic energy of roughly $210\,eV$ $(500\,eV - 288\,eV)$. The emitted electron leaves a vacancy in the s-shell behind, that is filled by another electron plummeting in from a higher level and thereby releasing another photon of roughly $260\,eV$ $(2s \rightarrow 1s\ 288\,eV - 17\,eV)$ or $277\,eV$ $(2p \rightarrow 1s\ 288\,eV - 11\,eV)$. Every photon that has taken part in this part of the cascade, is able to induce Stone-Thrower-Wales defects. *Ionization* If the photon energy does not suffice any more to expel a core electron, the outer electrons might be expelled and gain the energy of the photon decreased by $11\,eV$ or $16\,eV$ respectively. *Auger electrons* When a $2s$-electron fills the vacancy of $1s$, the released $260\,eV$ suffice to expel the remaining $2p$ electrons. These electrons then have a kinetic energy of roughly $249\,eV$ $(260\,eV - 11\,eV)$. The energies in this process still suffice to induce these defects. *Plummeting $2p$-electrons* If $2s$ has vacancies, a $2p$-electron might plummet in there releasing photons of about $5\,eV$ $(16\,eV - 11\,eV)$. The photons emitted by this sub-process can graphitize the carbon. *Inelastic scattering of electrons* Electrons emit photons of any energy below their kinetic energy whenever they are decelerated. This is a process to continuously decrease the energy of the particles. *Ionization by electrons* Electrons can transfer parts of their energy unto other bound electrons by colliding. The energy loss depends both on the material and the collision angle, and photons are emitted as well. Now, we have shown a route how the higher energy photons can reduce their energy, process the material inducing STW defects, and give rise to graphitizing photons. LA114

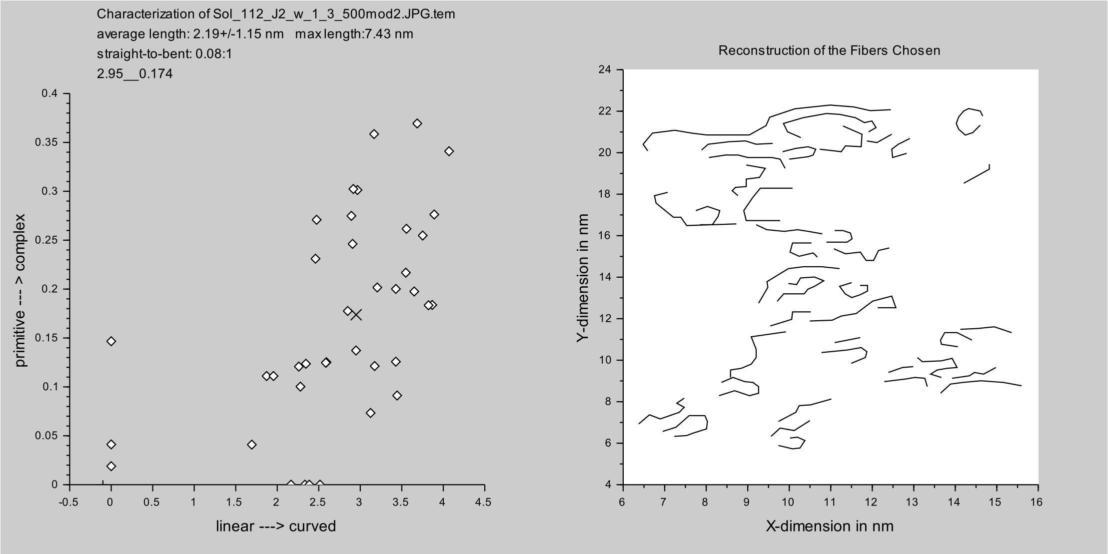

Figure 5.10: This figure shows the result window of the analysis of an HRTEM images of LA112. The right hand side shows the evaluated paths of that site. The left hand side shows a plot of the distribution of the curvature and the corresponding mean complexity. The abscissa (curvature) is in nm^{-1}. Random complexity values were assigned to them in the graph to better illustrate their number. The corresponding HRTEM image is Figure 5.11.

(Figure 4.35) did show almost no graphitization. Again, this can be explained by the penetration depth. As already mentioned, the material is processed homogeneously. Around thirty percent of the incident photons did not interact with the amorphous carbon. When the first step of the cascade happens, the emitted photons perceive a mass absorption coefficient of $\kappa = 1.96\,cm^2g^{-1}$, resulting in a penetration depth of nearly $2\,\mu m$. That is, these photons are nearly not absorbed at all have very little interaction with the material. In case there is the emission of electrons instead of secondary photons, the electrons do not have a wide reach. This again triggers a cascade of locally confined interactions in the range of up to some ten nanometers. This could aid the formation of curvatures. If there is only one interaction with only one bond, it is only the nearest neighbours that are involved in the restructuring. But if the secondary emission is able to interact with the vicinity of the initially affected atom, atoms involved are less constrained and the restructuring involves a larger area. Furthermore, if the entire wider neighbourhood of an atom is involved the restructuring can act almost simultaneously. In the case of the deeply-penetrating lower energy photons, there are only isolated photon-carbon interaction, both temporally and spatially isolated. Thus, if the constraints are too strong, the range of new configurations that could be assumed, is limited. However, if an incident photon is able to involve a wider region, there are fewer constraints. The HAC-sample LA112 is almost 50% thicker than LA114.

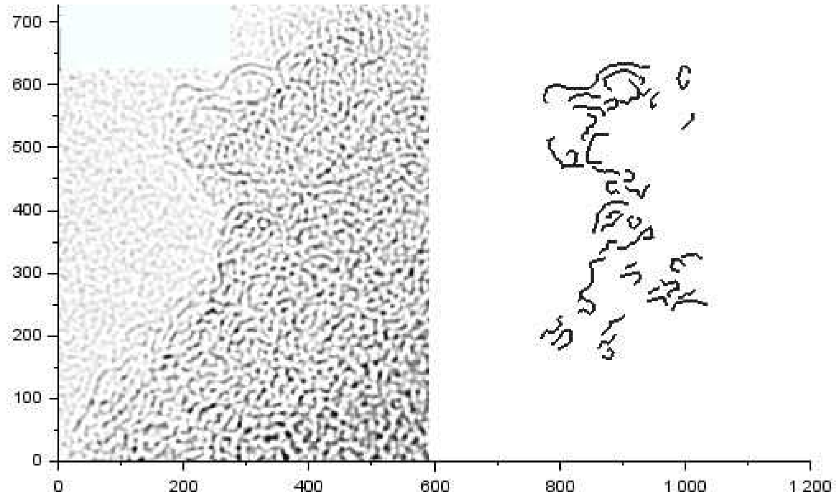

Figure 5.11: The HRTEM image shows the site of LA112 where the data of Figure 5.10 has been derived from. The left side shows the site, the right part shows the traced paths. The scale is $30\,nm^{-1}$.

But this does not affect the actual interaction with the secondary photons significantly. However, due to the presence of terminally bound hydrogen, the photons have more sites that can be restructured. The X-photons are easily capable of removing the hydrogen, creating reactive dangling bonds in the affected carbon that will bind to anything in its vicinity — other carbon atoms. Additionally, the irradiated carbon atoms might not only dehydrogenate, but will lose their bonds to anything in their vicinity. Thus they are completely free and unbound — free to assume a different and energetically more stable configuration. For LA113, which already consists of more graphitic sites being an iron-containing sample. The graphene shells around the iron are already bent and do not have as much free space to be re-arranged differently. However, the carbon matrix can still be processed — especially the matrix around very small iron nanoparticles. If we assume that an X-photon is fully absorbed by an iron nanoparticle, the emitted electrons encounter resistance inside the iron nanoparticle and heat it up. Using the simple equation $Q = mc\Delta T$ with Q being the absorbed thermal energy, c being the specific heat capacity of iron and ΔT the temperature difference. We find that the heating of spherical iron particles from $1\,nm$ in radius to $3\,nm$, may heat the granules up to $5000\,K$ to $200\,K$. That means that the smaller iron nanoparticles are able to heal any defects by thermal annealing, promoting graphitization in the vicinity of the smallest iron nanoparticles.

As for the XUV-photons, they have a rather low penetration depth. That is, if the sample is too thick with respect to the penetration depth, the sample is processed inhomogeneously. In the upper layers, the energetic photons can

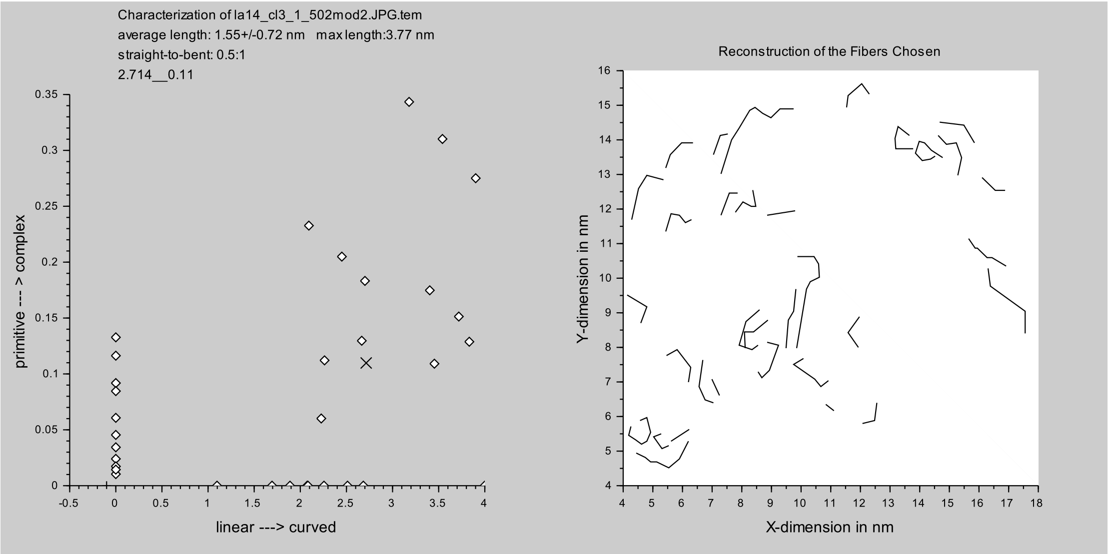

Figure 5.12: This figure shows the result window of the analysis of an HRTEM images of LA14. The right hand side shows the evaluated paths of that site. The left hand side shows a plot of the distribution of the curvature and the corresponding mean complexity. The abscissa (curvature) is in nm^{-1}. Random complexity values were assigned to them in the graph to better illustrate their number. The corresponding HRTEM image is Figure 5.13.

break bonds and ionize the carbon, but they cannot expel any 1s-photons. They can, in fact, follow every of the mentioned paths, that is in their energy range. Hence, their secondary emission will be lower energetic photons to a high degree that are capable of graphitizing. Thus, if a sample has a thickness that is by far greater than the penetration depth of the incident photons, it will experience graphitization to a higher degree. However, the higher energy secondary photons in the range of $20\,eV$ are capable of triggering locally-confined, but not isolated, cascades of interaction, as these photons have a very low range. To summarize

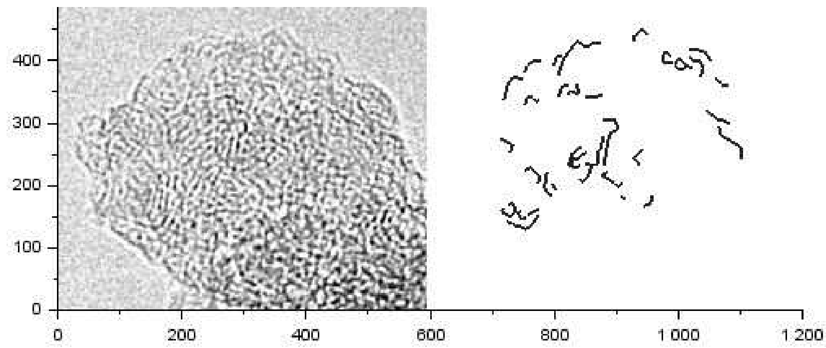

Figure 5.13: The HRTEM image shows the site of LA14 where the data of Figure 5.12 has been derived from. The left side shows the site, the right part shows the traced paths. The scale is $30\,nm^{-1}$.

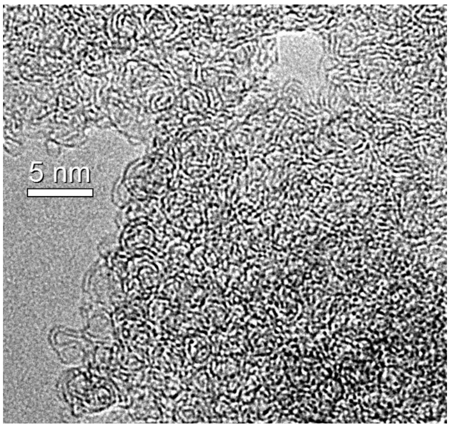

Figure 5.14: The HRTEM image shows highly processed site of LA114 (AC,X). The site is characterized by many round, hollow onion-like structures.

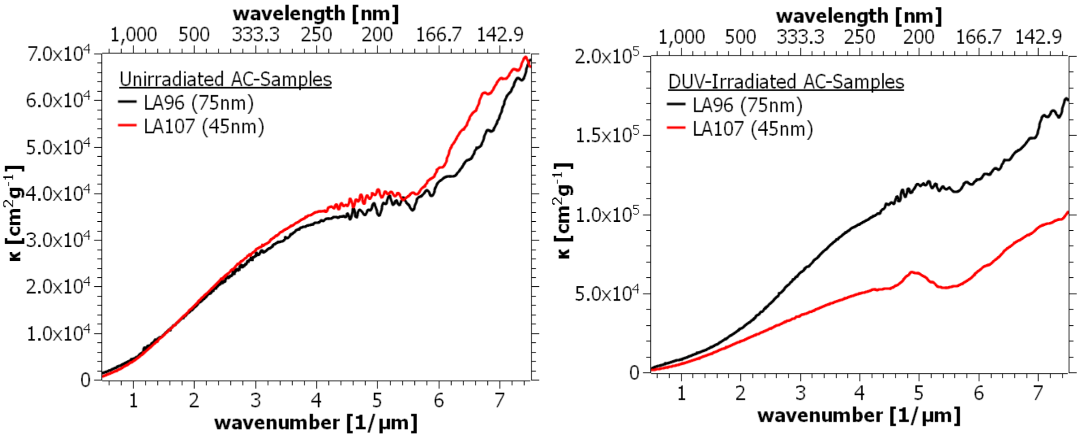

Figure 5.15: The graphs show unirradiated AC-samples (left) of different thickness and their DUV-irradiated counterparts (right). For the thicker sample (LA96), the graphitization, i.e. the general, strong increase of the π-band, is more dominant than for the thinner sample, LA107.

this section, the curvature is formed via STW defects that require photon energies above $9\,eV$. Samples whose thickness is greater than the penetration depth of the incident photons, can experience graphitization as dominant effect. The secondary emission, depending on its energy range, can trigger either graphitization or the formation of STW defects.

Chapter 6

Astrophysical Discussion

The main goal of the project was to investigate the irradiation-induced processing of carbonaceous grains of different composition and structure. The experimental approach served to understand the spectral and structural properties of interstellar and protoplanetary carbon material. Even though, the understanding of carbonaceous structures and absorption behaviour made progress thanks to the sophisticated experimental studies by Mennella et al. (1996); Gadallah et al. (2011); Rance et al. (2010) and others, the complete cycle of carbonaceous matter and the carrier of the 217 nm bump remain a mystery.
The main goal of the project was to investigate the irradiation-induced processing of carbonaceous matter. The experimental results combine and relate the findings of several authors:

- Mennella et al. (1996) found that a band arises upon treatment with UV-photons.
- Micelotta et al. (2012); Zhou and Shi (2003) described how bent structures in carbonaceous matter arise.
- Chhowalla et al. (2003) proposes onion-like carbonaceous materials as carrier of the 217 nm-bump.

We found, that upon irradiation a band, close to 217 nm, arises and the irradiated matter forms round and hollow onion-like structures (Figure 5.4).

A significant role in the processing of cosmic carbon dust grains is played by UV photons of different energies that can not only trigger reactions between atoms and clusters to form complex organic molecules in ices, but also interact with solid matter forming defects, and complete restructuring processes. UV photons are produced primarily by young stars (van Dishoeck et al., 2006) and are encountered in photo-dominated regions close to luminous O and B stars (Tielens, 2006). Furthermore, they are produced in secondary processes by interaction of cosmic rays with H_2 for example in molecular clouds leading to the subsequent emission of the excess energy at $122\,nm$ (Mathis et al., 1983). The role of X-rays on molecule formation or restructuring processes of solid grains was only studied in a few laboratory studies. However, there are astrophysical environments that can be dominated by X-rays instead of UV photons including the environment around active galactic nuclei or black holes (Green et al., 2015). Higher energy photons in the soft X-ray range are also emitted by e.g. supernova remnants as they are quite hot with temperatures around $10^6\,K$ — similar to coronal gas (Tielens, 2006; Ferrière, 2001). In addition, young stars are strong emitter of X-ray photons, too. In the first $300\,Myr$ of a solar-type star, the X-ray flux decreases by a factor of less than 10 and is about two orders of magnitude higher than for our Sun (Ribas et al., 2005). In addition, the intensity of X-rays can be increased dramatically in so-called X-ray flares. Due to their higher penetration depth, X-rays can propagate much easier than UV photons. For example, around the young star AU Mic at a distance of 10 AU of the disk, the measured photon fluxes are $10^9\,photons \cdot s^{-1}cm^{-2}$ at X-ray wavelengths (broadband) and $3 \cdot 10^8\,photons \cdot s^{-1}cm^{-2}$ at $CIII$ = 1175 $\AA$. T Tauri stars were found to have X-ray luminosities between $L_X = 10^{28} - 10^{32}\,erg \cdot s^{-1}$ (Aresu et al., 2011). These luminosities are similar to their UV luminosities ($L_{UV} = 10^{30} - 10^{31}\,erg \cdot s^{-1}$) and therefore X-rays are expected to affect the physics and chemistry of the upper layers of their surrounding protoplanetary disks. The role of low- and high-energy UV processing and of ionizing radiation such as X-rays was studied experimentally using cosmic dust analogues produced by laser ablation and subsequent condensation in a quenching gas atmosphere. Three different materials including hydrogenated fullerene-like and amorphous fullerene-like carbon grains were produced. One important aspect of the work was to study the role of iron-containing carbonaceous grains. It is well known that iron can influence the structure of carbon grains from e.g. Ristorcelli and Klotz (1997); Marty et al. (1994).

In our experimental studies we found, that upon irradiation a UV band, close to $217\,nm$, arises. The exact position varied slightly. The comparison between the pristine and irradiated carbon grains in the HRTEM images showed in many cases a general growth of the graphene layers, but also the appearance of round grain structures (Figure 5.3) and sometimes even almost onion-like structures (Figure 5.6).

In order to understand the processing completely, the structure of the pristine grain material has to be considered. What is generally produced in a laser ablation process is a grain material characterized by strongly curved graphene structures and the presence of fullerenes of different sizes. Upon irradiation defined closed curved structures are formed. The formation of such structures was observed upon irradiation with photons of $\lambda = 167\,nm$, $122\,nm \cdots 2.5\,nm$.

The required doses are small. The smallest dose that I have used and which gave rise to these structures, was around $10^{18}\,eV cm^{-2}$. Compared with Habing's dose of $3 \cdot 10^{23}\,eV cm^{-2}$ that was used as a guide line by Mennella et al. (1995); Gadallah (2010), this dose is utterly small. Mennella et al. (1996) and Henning et al. (2004) assume a time scale for the existence of a interstellar dust grain of about $10^7\,yr$ for a dose of $3 \cdot 10^{23}\,eV cm^{-2}$. For the minimum dose found here, the time scale would drop to around 10 years. This gives rise to the question whether these structures are stable under continued irradiation and whether the formation process reaches a stage of saturation and stagnates.

Other processes might reverse the formation of such curved structures, e.g. ion bombardment by cosmic rays are known to cause disorder (Baratta et al., 2004) or shock events. Furthermore, heat treatments, as shown by Wada et al. (1999) for onion-like carbon, are able to shift the maximum of the $\pi \rightarrow \pi^{\star}$-band towards lower wavenumbers, meaning that the curved structures heal their defects and become less curved. Will the cosmic dust particles eventually reach an equilibrium with respect to amorphization processes and graphitization processes?

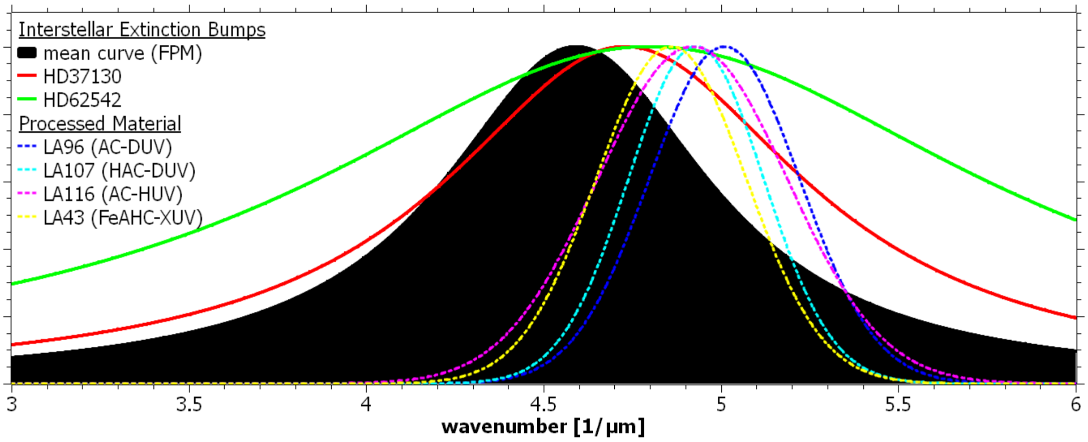

Figure 6.1: The graph shows the the normalised spectra of the interstellar extinction bump of the sightline of two stars and the averaged bump (Fitzpatrick and Massa, 2007) and compares them to the bands that were formed upon UV-photon irradiation in this thesis.

Looking at Figure 6.1 and Figure 6.2, one will find that the band position is off by ten to twenty nanometers or $0.2 \ldots 0.4\,\mu m^{-1}$. However, one also sees, that the band is narrower than the interstellar extinction band. This implies that the structures that are formed upon irradiation are distributed more narrowly, i.e. they are relatively well-defined. This gives rise to the possibility that distinct

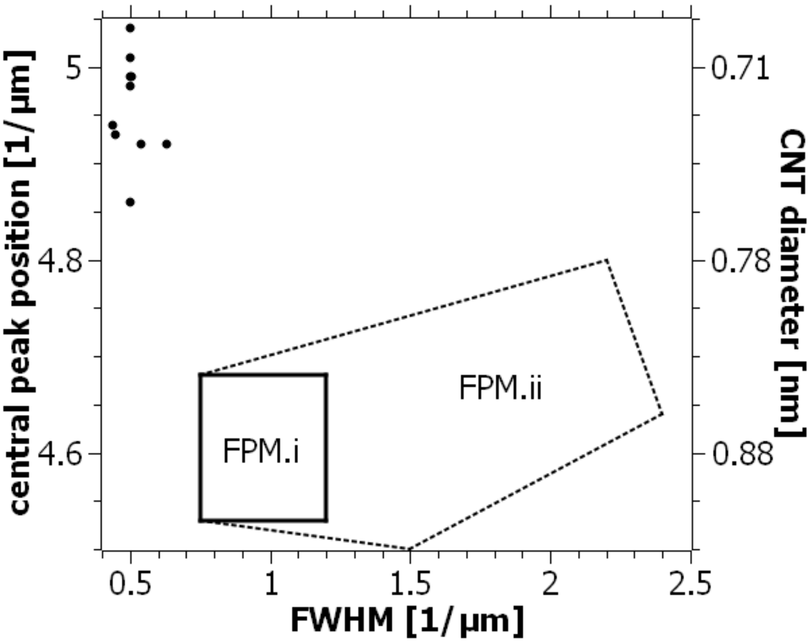

Figure 6.2: This graph is based on Figure 5.1 by Fitzpatrick and Massa (2007). The parameters of some of the bands that formed upon irradiation were included in the upper left corner as thick dots. The square with the label *FPM.i* denotes the center of the distribution of Fitzpatrick and Massa (2007), the irregular tetragon *FPM.ii* shows the range where the parameters of more deviating bands can be found. The right ordinate uses the relation found by Rance et al. (2010), that relates the central position of the π-absorption band of a carbon nanotube to its diameter.

UV-features such as the $217\,nm$ bump, could be explained by a distribution of similarly well-defined particles.

Irradiation Process

The formation of particular structures, here it is the curvature of graphene layers, upon irradiation is affected by the mobility of the affected atoms and the constraints given by its surrounding structures. We have found that medium energy-photon ($E > 9\,eV$) interaction increases the mobility, i.e. the range of variation of position, of an atom or the bonds between them, and thus the creation of well-defined structures resulting in a rather narrow band in the VUV-spectrum at around $4.95\,\mu m^{-1}$ (OLC). Furthermore, we can conclude that photons whose energy is significantly higher than $9\,eV$, reduce the constraints an atom experiences when re-arranging. This is caused by the interaction of the higher energy photons with the atoms creating photons and electrons of medium energy. Effectively, a high energy photon is transformed into a group of medium energy energy carriers, that increase the mobility of an entire site of a few nanometers, where they can induce STW defects.

Favouring of Graphitization

We have found, particularly when thin and thick, but otherwise alike samples were compared, that graphitization is not so much triggered by the high energy photons. The high energy photons trigger the formation of defects, whereas lower energy photons graphitize, meaning they heal defects. Graphitization only took place when the presence of lower energy photons in the sample could be inferred — either as primary radiation or secondary radiation. Samples whose thickness allowed the secondary low energy photons to escape with little interaction, were less graphitized than those whose secondary radiation was mostly absorbed internally.

Emergence of Particular Structures

We have found a clear candidate for the OLC-structure: bent graphene layers with a curvature of roughly $2.7nm^{-1}$. This particular structure is in good agreement with the structures that can be derived from the absorption measurements on size-selected carbon nano-tubes by Rance et al. (2010).

A consequence of this finding is, that other interesting structures like the $217\,nm$-bump, which we presume to be caused by a similarly-bent graphene layer (Figure 6.2), can be constrained further with respect to size for two reasons. The first reason is that there must be a structure that is big and stable enough to keep this curvature without healing the STW defects and straightening again. A corresponding carbon nano-tube would have a circumference of roughly $2.45\,nm$, which is probably a good guestimate for the lower limit of its size, as its edges are stabilizing each other. The $217\,nm$ bump itself would correspond to a curvature of $2.27\,nm^{-1}$. On the other hand we can estimate an upper limit. We have seen that low-energy photons graphitize the ACs and HACs. We have seen that higher-energy photons graphitize these grains too, if the sample is comparably thick, or thicker than the penetration depth of the secondary lower energy photons involved. The samples LA115 and LA43 showed mostly the emergence of OLC upon XUV-exposure, thus it seems reasonable to take their thickness as a guestimate and limit the maximum size of the carbon particles to some ten nanometers.

Combined with the knowledge of graphitization, the bending of layers and dehydrogenation, the models that demand hydrogen in their amorphous carbonaceous skeleton and exclude processing as proposed by Duley and Hu (2012), are unlikely to be the carrier of the interstellar extinction bump, as the photons would dehydrogenate the material, and thus change its electronic configuration and morphology. However, the notion of the necessity of sp^3-sites within an sp^2-like frame seems to be the right track in understanding said extinction bump. Yet, it seems likely, that the materials proposed by Duley and Hu (2012) could serve as a precursor to the carrier nonetheless.

The Incorporation of Iron

The production of graphene-covered iron granules succeeded and gives rise to two implications: Firstly, the incorporation of iron increases the aromaticity of AC, which is in accordance with Jones (2013). Secondly, the thus-formed graphene-layers make the irradiation processing more efficient and thorough, although the generally higher absorption might finally mask effects of additional bent graphene layers. Thirdly, iron itself is masked in the carbon. Iron does not contribute any specific spectral features, but increases the mass absorption by up to two orders of magnitude. In terms of similarity, the correlation coefficient of AC and FeAC samples is quite high. This yields the possibility that in cases where computations demand unreasonably high amounts of carbon, it could be substituted by iron-containing AC-grains, decreasing the required amount of carbon considerably and accounting for the invisible iron. However, this substitution only makes sense for regions where iron is to be expected.

Chapter 7

Outlook

Conclusion

In this thesis, I have investigated the morphological and electronic changes in different fullerene-like soot materials. I have irradiated iron-containing and iron-free hydrogenated and hydrogen-free soot with UV-photons from the vacuum UV-range up to the soft X-ray range.

I have found that laser-ablated mixtures of graphite and iron powder yield very small iron nanoparticles in the range of $5\,nm$. These iron nanoparticles are covered by graphene-layers that are formed by exsolution of dissolved carbon. Furthermore, I have a way to coarsely control the iron-content of the thus-produced materials — the hydrogen-content of the quenching atmosphere is able to remove excess carbon that would otherwise form matrix of more or less hydrogenated amorphous carbon.

Iron-containing carbonaceous materials can mimic the extinction curves of amorphous carbon and require less carbon to do so, as their mass absorption coefficient is considerably higher.

UV-irradiation can trigger Stone-Wales-Thrower (STW) defects in amorphous carbon. The STW defects cause graphene layers to bend. A minimum photon energy to trigger these STW defects could be determined to be around $9\,eV$. Energies below this threshold are more likely to graphitize the amorphous carbonaceous material. The STW defects can be induced by expelling both outer and inner electrons, which remove outer electrons from their shell by having them fill an electron vacancy, via energetic photons.

The irradiation processing caused a band to emerge in the range of $4.8 - 5.0\,\mu m^{-1}$. This spectral feature can be attributed to onion-like carbon (OLC). The curvature of the bent graphene layers and the central position of the thus-formed band matches the curvature of the carbon nano-tubes measured by Rance et al. (2010). So far, no correlation between the width and position on the one hand, and the photon energy and the precursor material could be established.

The energy dose required to give rise to the OLC-band is significantly lower than Habing's dose with $10^{18}\,eVcm^{-2}$ compared to $3 \cdot 10^{23}\,eVcm^{-2}$.

Open Questions and Considerations

Although we have achieved some progress in understanding the irradiation processing of amorphous carbonaceous materials, some question are still left unanswered.

Both Mennella et al. (1996) and Gadallah et al. (2011) formed a band at $215\,nm$ and $217\,nm$ respectively. In order to further investigate the restructuring mechanisms and their relation to the formation of curvature-related bands, it is advisable to study the irradiation behaviour of differently-produced precursor materials. Carbon is a very versatile element that can form numerous structures, and can at times be either very reactive or quite inert — all depending on its hybridization and structure. Therefore, investigating the restructuring of various carbonaceous materials such as those produced by arc-discharge, resistive heating or laser-pyrolysis will be necessary. Furthermore, the interaction of counter-acting processing techniques will give more insight into the cosmic processing. Thermal annealing processes create more ordered structures, whereas ion bombardments create disorder. UV-irradiation, however, depending on the photon energy, lies somewhere between. Thus, a combination of either thermal annealing with order-disrupting high energy photons or ion-bombardment with high or medium energy photons could yield useful insights. Another aspect worth investigating is simple long term irradiation. Will graphitization eventually prevail? Will the amount of STW defects reach saturation? Another aspect that requires investigation is the influence of the photon flux: depending on the flux either the effects attributed to the photon energy, or effects attributed to heating dominate. The intermediate fluxes between those, where the photon energy prevails and where the rapid heating dominate, have not been studied sufficiently. It must be stressed that the sample thickness plays a great role in the photo-processing, as secondary processes will occur. Therefore, when continuing these kinds experiments, one should try to match the sample thickness with the penetration depth — or at least make sure that the samples are processed homogeneously. In addition to the processing, the investigation of carbon onions (OLC) must continue. Especially the production of carbon onion must be optimized to allow to produce measurable quantities. Furthermore, one should aim at finding a way to control the size of the carbon onions. All this would allow to measure the spectroscopic properties of the OLC in more detail and benefit the improvement of astrophysical models of the interstellar extinction. Additionally, being able to produce well-defined iron-containing OLC might be of interest for the pharmaceutical industry.

Bibliography

G. Aresu, I. Kamp, R. Meijerink, P. Woitke, W.-F. Thi, and M. Spaans. X-ray impact on the protoplanetary disks around T Tauri stars. *Astronomy and Astrophysics*, 526:A163, 2011.

G. A. Baratta, V. Mennella, J. R. Brucato, L. Colangeli, G. Leto, M. E. Palumbo, and G. Strazzulla. Raman spectroscopy of ion-irradiated interplanetary carbon dust analogues. *Journal of Raman Spectroscopy*, 35(6):487–496, 2004. ISSN 1097-4555.

Y. Benilan, M.-C. Gazeau, E.-T. Es-Sebbar, A. Jolly, E. Arzoumanian, N. Fray, and H. Cottin. Optimization of microwave Hydrogen plasma discharges to mimic Lyman alpha (121.6 nm) solar irradiations. In *EPSC-DPS Joint Meeting 2011*, page 1317, October 2011.

C. N. Berglund and W.E. Spicer. Photoemission Studies of Copper and Silver: Experiment. *Physical Review*, 136(4 A), November 1964.

J. Bernard-Salas, J. Cami, E. Peeters, A.P. Jones, E. R. Micelotta, and M. A. T. Groenewegen. On the Excitation and Formation of Circumstellar Fullerenes. *The Astrophysical Journal*, 757(1):41, 2012.

A. Blanco, E. Bussoletti, L. Colangeli, S. Fonti, V. Mennella, and J. R. Stephens. The ultraviolet spectrum of annealed hydrogenated amorphous carbon grains. *The Astrophysical Journal*, 406:739–741, April 1993.

A. Blasberger, E. Behar, H. B. Perets, N. Brosch, and A. G. G. M. Tielens. Observational Evidence Linking Interstellar UV Absorption to PAH Molecules. *The Astrophysical Journal*, 836:173, February 2017.

C.F. Bohren and D.R. Huffman. *Absorption and Scattering of Light by Small Particles.* WILEY-VCH Verlag, Weinheim, 2004.

L. Boltzmann. Ableitung des Stefan'schen Gesetzes, betreffend die Abhängigkeit der Wärmestrahlung von der Temperatur aus der electromagnetischen Lichttheorie. *Annalen der Physik*, 258:291–294, 1884.

R.B. Cairns and J.A.R. Samson. Metal Photocathodes as Secondary Standards for Absolute Intensity Measurements in the Vacuum Ultraviolet$*$. *Journal of the Optical Society of America*, 56(11):1568–1573, Nov 1966.

J.D. Carette, B. Feuerbacher, B. Fitton, H. Froitzheim, M. Henzler, H. Ibach, J. Kirschner, and D. Roy. *Electron Spectroscopy for Surface Analysis*. Springer-Verlag, Berlin Heidelberg New York, 1977.

Chemistry. UV-Vis Absorption Spectroscopy. URL `http://teaching.shu.ac.uk/hwb/chemistry/tutorials/molspec/uvvisab1.htm`.

I. Cherchneff. Abundances in circumstellar dust. In D. Friedli, M. Edmunds, C. Robert, and L. Drissen, editors, *Abundance Profiles: Diagnostic Tools for Galaxy History*, volume 147, 1998.

I. Cherchneff. A chemical study of the inner winds of asymptotic giant branch stars. *Astronomy and Astrophysics*, 456(3):1001–1012, 2006.

I. Cherchneff and E. Dwek. The chemistry of population iii supernova ejecta. ii. the nucleation of molecular clusters as a diagnostic for dust in the early universe. *The Astrophysical Journal*, 713:1–24, 2010.

M. Chhowalla, H. Wang, N. Sano, K. B. K. Teo, S. B. Lee, and G. A. J. Amaratunga. Carbon Onions: Carriers of the 217.5 nm Interstellar Absorption Feature. *Phys. Rev. Lett.*, 90:155504, Apr 2003.

H. Cottin, M. H. Moore, and Y. Bénilan. Photodestruction of Relevant Interstellar Molecules in Ice Mixtures. *The Astrophysical Journal*, 590:874–881, June 2003.

H. Dai. Nanotube Growth and Characterization. In M.S. Dresselhaus, G. Dresselhaus, and Ph. Avouris, editors, *Carbon Nanotubes*, chapter 2. Springer, 2nd edition, 2001.

N. Damany, J. Romand, and B. Vodar, editors. *Some Aspects of Vacuum Ultraviolet Radiation Physics*. Akademie-Verlag, Berlin, 1974.

E. Dartois, O. Marco, G. M. Muñoz-Caro, K. Brooks, D. Deboffle, and L. d'Hendecourt. Organic matter in Seyfert 2 nuclei: Comparison with our Galactic center lines of sight. *Astronomy and Astrophysics*, 423:549–558, August 2004.

O. Dhez, H. Ade, and S. Urquhart. Near Edge X-ray Absorption Spectroscopy of Polymers. In *APS Meeting Abstracts*, March 2001.

V. Dose. Ultraviolet Bremsstrahlung spectroscopy. *Progress in Surface Science*, 13(3):225 – 283, 1983.

B. T. Draine. *Physics of the Interstellar and Intergalactic Medium.* Princeton University Press, Princeton, 2011.

W. W. Duley and A. Hu. The 217.5 nm Band, Infrared Absorption, and Infrared Emission Features in Hydrogenated Amorphous Carbon Nanoparticles. *The Astrophysical Journal*, 761(2):115, 2012.

P. W. Dunk, J.-J. Adjizian, N.K. Kaiser, J.P. Quinn, G.T. Blakney, C.P. Ewels, A.G. Marshall, and H.W. Kroto. Metallofullerene and fullerene formation from condensing carbon gas under conditions of stellar outflows and implication to stardust. *Proceedings of the National Academy of Sciences*, 110(45):18081–18086, 2013.

C.H.S. Dupuy, editor. *Radiation Damage Processes in Materials.* Springer-Verlag, Noordhoff - Leyden, 1975.

E. Dwek. Iron: A Key Element for Understanding the Origin and Evolution of Interstellar Dust. *The Astrophysical Journal*, 825(2):136, 2016.

U. Falke, A.-K. Weber, and J. Ullmann. Dispersion of the Valence Electron Energy Loss in Thin Amorphous Carbon Films deposited by Ion Assisted Evaporation of Graphite. *Microsc. Microanal. Microstruct.*, 6(1):113–120, 1995.

K.M. Ferrière. The interstellar environment of our galaxy. *Rev. Mod. Phys.*, 73: 1031–1066, Dec 2001.

E. L. Fitzpatrick and D. Massa. An Analysis of the Shapes of Interstellar Extinction Curves. V. The IR-through-UV Curve Morphology. *The Astrophysical Journal*, 663(1):320, 2007.

J. Franck and G. Hertz. Über Zusammenstöße zwischen Elektronen und Molekülen des Quecksilberdampfes und die Ionisierungsspannung desselben. In *Verhandlungen der Deutschen Physikalischen Gesellschaft*, number 16, page 457–467. Deutsche Physikalische Gesellschaft, 1914.

T. Fujimori, Ljubisa R. Radovic, Alejandro B. Silva-Tapia, M. Endo, and K. Kaneko. Structural importance of Stone–Thrower–Wales defects in rolled and flat graphenes from surface-enhanced Raman scattering. *Carbon*, 50(9): 3274 – 3279, 2012. ISSN 0008-6223. Festschrift dedicated to Peter A. Thrower, Editor-in-Chief, 1972 - 2012.

D. Fulvio, A. C. Brieva, S. H. Cuylle, H. Linnartz, C. Jäger, and Th. Henning. A straightforward method for Vacuum-Ultraviolet flux measurements: The case of the hydrogen discharge lamp and implications for solid-phase actinometry. *Applied Physics Letters*, 105(1):014105, 2014.

K. Gadallah. *Structure and Optical Properties of Cosmic Nanoparticles: UV Irradiation and Thermal Processing of Carbonaceous Materials*. Phd thesis, Astrophysikalisches Institut und Universitätsternwarte, Friedrich-Schiller-Universität Jena, 2010.

K. Gadallah, H. Mutschke, and C. Jäger. UV irradiated hydrogenated amorphous carbon (HAC) materials as a carrier candidate of the interstellar UV bump at 217.5 nm. *Astronomy and Astrophysics*, 528:A56, April 2011.

K. Gadallah, H. Mutschke, and C. Jäger. Mid-infrared spectroscopy of UV irradiated hydrogenated amorphous carbon materials. *Astronomy and Astrophysics*, 544:A107, August 2012.

K. Gadallah, H. Mutschke, and C. Jäger. Analogs of solid nanoparticles as precursors of aromatic hydrocarbons. *Astronomy and Astrophysics*, 554:A12, June 2013.

V. R. Galakhov, A. S. Shkvarin, A. S. Semenova, M. A. Uimin, A. A. Mysik, N. N. Shchegoleva, A. Ye. Yermakov, and E. Z. Kurmaev. Characterization of Carbon-Encapsulated Nickel and Iron Nanoparticles by Means of X-ray Absorption and Photoelectron Spectroscopy. *The Journal of Physical Chemistry C*, 114(51): 22413–22416, 2010.

V. R. Galakhov, A. Buling, M. Neumann, N. A. Ovechkina, A. S. Shkvarin, A. S. Semenova, M. A. Uimin, A. Y. Yermakov, E. Z. Kurmaev, O. Y. Vilkov, and D. W. Boukhvalov. Carbon States in Carbon-Encapsulated Nickel Nanoparticles Studied by Means of X-Ray Absorption, Emission, and Photoelectron Spectroscopies. *ArXiv e-prints*, November 2011.

L. Gavilan, I. Alata, K.C. Le, T. Pino, A. Giuliani, and E. Dartois. Vuv spectroscopy of carbon dust analogs: contribution to interstellar extinction. *Astronomy and Astrophysics*, 586(A 106), 2016.

M. Güdel, A. Telleschi, M. Audard, S. L. Skinner, K. R. Briggs, F. Palla, and C. Dougados. X-rays from jet-driving protostars and T Tauri stars. *Astronomy and Astrophysics*, 468(2):515–528, 2007.

C.-E. Green, M. R. Cunningham, J. A. Green, J. R. Dawson, P. A. Jones, Á. R. López-Sánchez, L. Verdes-Montenegro, C. Henkel, W. A. Baan, S. Martín, and et al. Intensity ratios for XDR/PDR identification. *Proceedings of the International Astronomical Union*, 11(S315), 2015.

H.J. Habing. The interstellar radiation density between 912Å and 2400Å. *Bulletin of the Astronomical Institues of The Netherlands*, 19:421, January 1968.

B.L. Henke, E.M. Gullikson, and J.C. Davis. X-Ray Interactions: Photoabsorption, Scattering, Transmission, and Reflection at E = 50-30,000 eV, Z = 1-92. *Atomic Data and Nuclear Data Tables*, 54(2):181 – 342, 1993.

S.J. Henley, P.C.P. Watts, N. Mureau, and S. Ravi P. Silva. Laser-induced decoration of carbon nanotubes with metal nanoparticles. *Applied Physics A*, 93(4): 875–879, 2008.

Th. Henning and F. Salama. Carbon in the Universe. *Science*, 282:2204, December 1998.

Th. Henning, C. Jäger, and H. Mutschke. Laboratory Studies of Carbonaceous Dust Analogs. In A.N. Witt, G.C. Clayton, and B.T. Draine, editors, *Astrophysics of Dust*, volume 309, 2004.

S. Hüfner. *Photoelectron Spectroscopy: Principles and Applications.* Springer-Verlag, Berlin Heidelberg, 3rd edition, 2003.

Y. Iida and E.S. Yeung. Optical Monitoring of Laser-Induced Plasma Derived from Graphite and Characterization of the Deposited Carbon Film. *Applied Spectroscopy*, 48(8):945–950, 1994.

C. Jäger, H. Mutschke, Th. Henning, and F. Huisken. Spectral Properties of Gas-phase Condensed Fullerene-like Carbon Nanoparticles from Far-ultraviolet to Infrared Wavelengths. *The Astrophysical Journal*, 689:249-259, December 2008a.

C. Jäger, H. Mutschke, I. Llamas-Jansa, Th. Henning, and F. Huisken. Laboratory analogs of carbonaceous matter: Soot and its precursors and by-products. In S. Kwok and S. Sanford, editors, *Organic Matter in Space*, volume 251 of *IAU Symposium*, pages 425–432, October 2008b.

C. Jäger. Spectral properties of carbon black. *Journal of Non Crystalline Solids*, 258:161–179, November 1999.

C. Jäger, H. Mutschke, and Th. Henning. Optical properties of carbonaceous dust analogues. *Astronomy and Astrophysics*, 332:291–299, April 1998.

A. P. Jones. Heteroatom-doped hydrogenated amorphous carbons, a-C:H:X - “Volatile” silicon, sulphur and nitrogen depletion, blue photoluminescence, diffuse interstellar bands and ferro-magnetic carbon grain connections. *Astronomy and Astrophysics*, 555:A39, 2013.

A.P. Jones. Iron or iron oxide in the interstellar medium? *Monthly Notices of the Royal Astronomical Society*, 245:331–334, 1990.

A.P. Jones, W.W. Duley, and D.A. Williams. The structure and evolution of hydrogenated amorphous carbon grains and mantles in the interstellar medium. *Royal Astronomical Society, Quarterly Journal*, 31:567–582, December 1990.

E. Kaxiras and K. C. Pandey. Energetics of defects and diffusion mechanisms in graphite. *Phys. Rev. Lett.*, 61:2693–2696, Dec 1988.

Y. Kimura, K. K. Tanaka, T. Nozawa, S. Takeuchi, and Y. Inatomi. Pure iron grains are rare in the universe. *Science Advances*, 3:e1601992, January 2017.

E. Kovačević, J. Berndt, I. Stefanović, H.-W. Becker, C. Godde, T. Strunskus, J. Winter, and L. Boufendi. Formation and material analysis of plasma polymerized carbon nitride nanoparticles. *Journal of Applied Physics*, 105(10):104910–104910, May 2009.

S. A. Krasnokutski and F. Huisken. A simple and clean source of low-energy atomic carbon. *Applied Physics Letters*, 105(11):113506, 2014.

A. Laikhtman, I. Gouzman, and A. Hoffman. NEXAFS spectroscopy of crystalline and ion beam irradiated diamond surfaces. *Diamond and Related Materials*, 9 (3–6):1026 – 1031, 2000. ISSN 0925-9635.

C. Lenardi, P. Piseri, V. Briois, C. E. Bottani, A. Li Bassi, and P. Milani. Near-edge x-ray absorption fine structure and Raman characterization of amorphous and nanostructured carbon films. *Journal of Applied Physics*, 85(10):7159–7167, 1999.

X. F. Li, A. L’Huillier, M. Ferray, L. A. Lompré, and G. Mainfray. Multiple-harmonic generation in rare gases at high laser intensity. *Phys. Rev. A*, 39: 5751–5761, Jun 1989.

I. Llamas-Jansa. *Experimental Study of the Optical and Structural Properties of Carbon Nanoparticles*. Phd thesis, Astrophysikalisches Institut und Universitätsternwarte, Friedrich-Schiller-Universität Jena, 2006.

N. Luo, K. Liu, Z. Liu, X. Li, S. Chen, Y. Shen, and T. Chen. Controllable synthesis of carbon coated iron-based composite nanoparticles. *Nanotechnology*, 23:475603, November 2012.

P. Marty, G. Serra, B. Chaudret, and I. Ristorcelli. Iron-Aromatics Chemistry in Interstellar Clouds. In I. Nenner, editor, *Molecules and Grains in Space*, volume 312 of *American Institute of Physics Conference Series*, page 183, January 1994.

J. S. Mathis, P. G. Mezger, and N. Panagia. Interstellar radiation field and dust temperatures in the diffuse interstellar matter and in giant molecular clouds. *Astronomy and Astrophysics*, 128:212–229, November 1983.

V. Mennella, L. Colangeli, A. Blanco, E. Bussoletti, S. Fonti, P. Palumbo, and H. C. Mertins. A dehdrogenation study of cosmic carbon analogue grains. *The Astrophysical Journal*, 444:288–292, May 1995.

V. Mennella, L. Colangeli, P. Palumbo, A. Rotundi, W. Schutte, and E. Bussoletti. Activation of an Ultraviolet Resonance in Hydrogenated Amorphous Carbon Grains by Exposure to Ultraviolet Radiation. *Astrophysical Journal Letters*, 464:L191, June 1996.

V. Mennella, G. A. Baratta, M. E. Palumbo, and E. A. Bergin. Synthesis of CO and CO_2 Molecules by UV Irradiation of Water Ice-covered Hydrogenated Carbon Grains. *The Astrophysical Journal*, 643:923–931, June 2006.

E.R. Micelotta, A.P. Jones, J. Cami, E. Peeters, J. Bernard-Salas, and G. Fanchini. The Formation of Cosmic Fullerenes from Arophatic Clusters. *The Astrophysical Journal*, 761(1):35, 2012.

Y. Miyajima, A. A. D. T. Adikaari, S. J. Henley, J. M. Shannon, and S. R. P. Silva. Electrical properties of pulsed UV laser irradiated amorphous carbon. *Applied Physics Letters*, 92(15):152104, April 2008. doi: 10.1063/1.2908208.

J. Narayan and A. Bhaumik. Novel phase of carbon, ferromagnetism, and conversion into diamond. *Journal of Applied Physics*, 118(21):215303, 2015.

R.J. Narayan and D. Scholvin. Nanostructured carbon-metal composite films. *Journal of Vacuum Science & Technology B: Microelectronics and Nanometer Structures Processing, Measurement, and Phenomena*, 23(3):1041–1046, 2005.

W.D. Nesse. *Introduction to Mineralogy.* Oxford University Press, New York, 2000. ISBN 978-0-19-510691-6.

F. Neufingerl, editor. *Chemie 1 — Allgemeine und anorganische Chemie.* Jugend & Volk, Wien, 2006.

NIST:Water. Water: Condensed Phase Spectrum, 1969. URL `http://webbook.nist.gov/cgi/inchi?ID=C7732185&Type=IR-SPEC&Index=1#IR-SPEC`.

M. A. Ordal, L. L. Long, R. J. Bell, S. E. Bell, R. R. Bell, R. W. Alexander, and C. A. Ward. Optical properties of the metals Al, Co, Cu, Au, Fe, Pb, Ni, Pd, Pt, Ag, Ti, and W in the infrared and far infrared. *Appl. Opt.*, 22(7):1099–1119, Apr 1983.

G. A. Rance, D. H. Marsh, R. J. Nicholas, and A. N. Khlobystov. UV-vis absorption spectroscopy of carbon nanotubes: Relationship between the π-electron plasmon and nanotube diameter. *Chemical Physics Letters*, 493:19–23, June 2010.

L. Ravagnan, G. Bongiorno, D. Bandiera, E. Salis, P. Piseri, P. Milani, C. Lenardi, M. Coreno, M. de Simone, and K.C. Prince. Quantitative evaluation of sp/sp^2 hybridization ratio in cluster-assembled carbon films by in situ near edge X-ray absorption fine structure spectroscopy. *Carbon*, 44(8), 2006.

S. Reich, C. Thomsen, and J. Maultzsch. *Carbon Nanotubes.* WILEY-VCH Verlag, Weinheim, 2004.

L. Reimer and H. Kohl. *Transmission Electron Microscopy: Physics of Image Formation.* Optical Sciences. Springer, Berlin, 5th edition, 2008.

I. Ribas, E. F. Guinan, M. Güdel, and M. Audard. Evolution of the Solar Activity over Time and Effects on Planetary Atmospheres. I. High-Energy Irradiances (1-1700 Å). *The Astrophysical Journal*, 622:680–694, March 2005.

I. Ristorcelli and A. Klotz. Organometallic catalysis for aromatic molecules formation in carbon rich envelopes. *Astronomy and Astrophysics*, 317(317):962–967, 1997.

J. Robertson and E. P. O'Reilly. Electronic and atomic structure of amorphous carbon. *Phys. Rev. B*, 35:2946–2957, Feb 1987.

F. Rouleau, Th. Henning, and R. Stognienko. Constraints on the properties of the 2175Å interstellar feature carrier. *Astronomy and Astrophysics*, 322:633–645, June 1997.

T. Sabri, G. A. Baratta, C. Jäger, M. E. Palumbo, Th. Henning, G. Strazzulla, and E. Wendler. A laboratory study of ion-induced erosion of ice-covered carbon grains. *Astronomy and Astrophysics*, 575(A76):A76, March 2015.

A. Sakata, S. Wada, A. T. Tokunaga, T. Narisawa, H. Nakagawa, and H. Ono. Ultraviolet spectra of quenched carbonaceous composite derivatives: Comparison to the '217 nanometer' interstellar absorption feature. *The Astrophysical Journal*, 430:311–316, July 1994.

J.W. Salisbury, L.C. Walter, N. Vergo, and D.M. d'Aria. *Infrared (*$2.1 - 25\mu m$*) Spectra of Minerals*. The John Hopkins University Press, London and Baltimore, 1992.

S. Schlemmer, T. Giessen, H. Mutschke, and C. Jäger, editors. *Laboratory Astrophysics*. Wiley-VCH, Weinheim, 2015.

M. Schnaiter, H. Mutschke, Th. Henning, D. Lindackers, M. Strecker, and P. Roth. Ultraviolet Spectroscopy of Matrix-isolated Amorphous Carbon Particles. *Astrophysical Journal Letters*, 464:L187, June 1996.

M. Schnaiter, H. Mutschke, J. Dorschner, Th. Henning, and F. Salama. Matrix-isolated Nano-sized Carbon Grains as an Analog for the 217.5 Nanometer Feature Carrier. *The Astrophysical Journal*, 498:486–496, May 1998.

G. Scoles, D. Bassi, U. Buck, and D. Lainé, editors. *Free Jet Sources*. Number v. 1 in Atomic and Molecular Beam Methods. Oxford University Press, 1988. ISBN 9780195042801.

T. P. Stecher. Interstellar Extinction in the Ultraviolet. II. *The Astrophysical Journal*, 157:L125, August 1969.

T.P. Stecher and B. Donn. On graphite and interstellar extinction. *The Astrophysical Journal*, 142:1681, 1965.

M. Steglich, C. Jäger, G. Rouillé, F. Huisken, H. Mutschke, and Th. Henning. Electronic Spectroscopy of Medium-sized Polycyclic Aromatic Hydrocarbons: Implications for the Carriers of the 2175 Å UV Bump. *The Astrophysical Journal Letters*, 712(1):L16, 2010.

A.J. Stone and D.J. Wales. Theoretical studies of icosahedral C60 and some related species. *Chemical Physics Letters*, 128(5):501 – 503, 1986. ISSN 0009-2614.

J. Tauc, R. Grigorovici, and A. Vancu. Optical Properties and Electronic Structure of Amorphous Germanium. *physica status solidi (b)*, 15(2):627–637, 1966. ISSN 1521-3951.

D. Thomas. The Carbon Family Group 14: C to Pb Electron Binding Energies, 1997. URL `http://www.chembio.uoguelph.ca/educmat/atomdata/bindener/grp14num.htm`.

A.G.G.M. Tielens, editor. *The Physics of the Interstellar Medium.* Cambridge University Press, Cambridge, 2006.

D. Ugarte. Formation mechanism of quasi-spherical carbon particles induced by electron bombardment. *Chemical Physics Letters*, 207:473–479, May 1993.

E.F. van Dishoeck, B. Jonkheid, and M.C. van Hemert. Photoprocesses in protoplanetary disks. *Faraday Discuss.*, 133:231–243, 2006.

S. Wada, C. Kaito, S. Kimura, H. Ono, and A. T. Tokunaga. Carbonaceous onion-like particles as a component of interstellar dust. *Astronomy and Astrophysics*, 345:259–264, May 1999.

H. Walter. Uv-irradiation processing of hydrogenated amorphous carbonaceous materials. Master's thesis, Astrophysikalisches Institut und Universitätsternwarte, Friedrich-Schiller-Universität Jena, 2013.

Y. Wang, C. G. An, Y. Z. He, and H. Li. Structure and Properties of Graphite Microspheres Containing Ferromagnetic Metal Prepared by Acid Corrosion of Cast Iron. *Journal of Materials Engineering and Performance*, 23(12):4446–4452, 2014.

Z.L. Wang, editor. *Characterization of Nanophase Materials.* Wiley VCH, Weinheim, 2000.

P. Warneck. A microwave-powered hydrogen lamp for vacuum ultraviolet photochemical research. *Applied Optics*, 1:721–726, November 1962.

C. Weidner and J. S. Vink. The masses, and the mass discrepancy of O-type stars. *Astronomy and Astrophysics*, 524:A98, December 2010.

M. S. Westley, R. A. Baragiola, R. E. Johnson, and G. A. Baratta. Ultraviolet photodesorption from water ice. *Planetary and Space Science*, 43:1311–1315, February 1995.

X. Zhao, Y. Liu, S. Inoue, T. Suzuki, R. O. Jones, and Y. Ando. Smallest Carbon Nanotube Is 3 Åin Diameter. *Physical Review Letters*, 92(12), 2004.

L.G. Zhou and S.Q. Shi. Formation energy of Stone–Wales defects in carbon nanotubes. *Applied Physics Letters*, 83(6):1222–1224, 2003.

Appendix A

The Deconvolution Programme

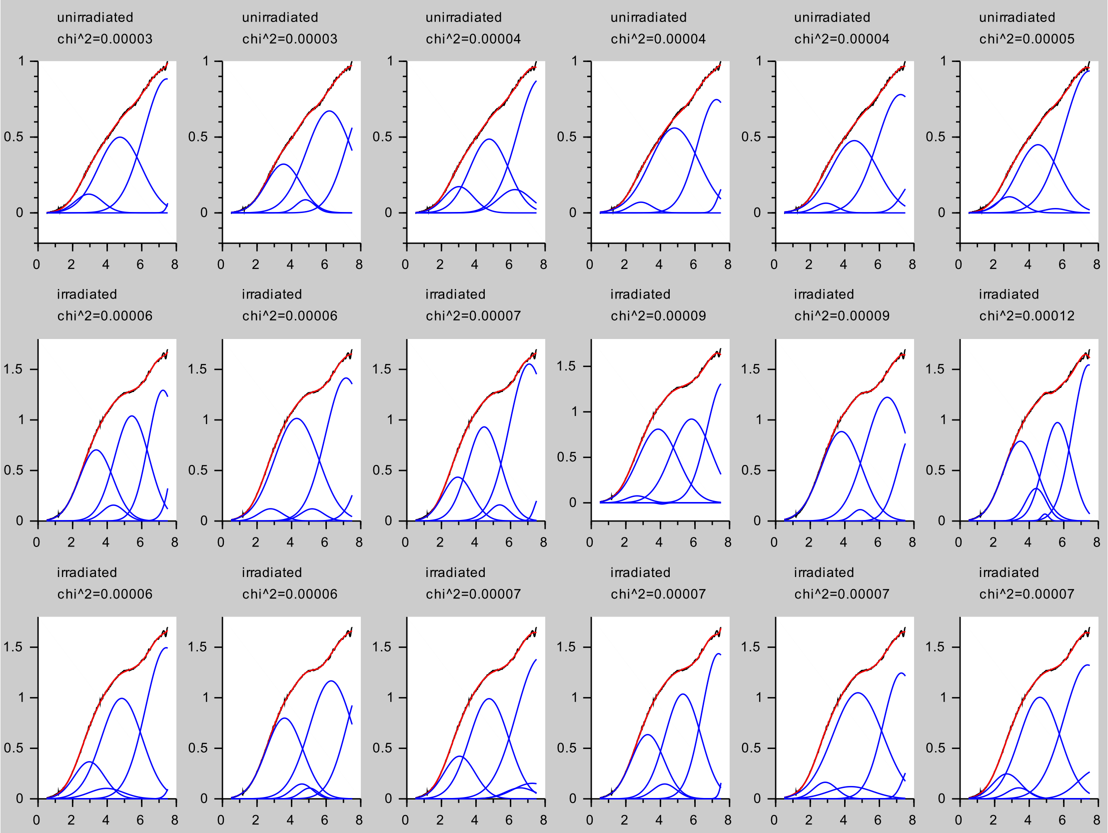

Figure A.1: This image is the actual output of the fitting routine. The first row represents suggestions for the unirradiated sample, the second row gives suggestions for an ab-initio fit for the irradiated sample. The fourth row displays suggestions for the spectrum of the irradiated sample based on the parameters of the unirradiated sample. For reasons of clarity, instead of each ten suggestions, only six are shown.

Appendix B

Gap Energy

The gap energy E_{gap} has been computed using a Tauc plot (Gadallah, 2010; Tauc et al., 1966). In a Tauc plot one usually extrapolates the linear slope of the modified mass absorption coefficient $\sqrt{\alpha h\nu}$ according to

$$\sqrt{\alpha h\nu} = A \cdot (E - E_{gap}) \Rightarrow \alpha\hbar\omega \propto (\hbar\omega - E_{gap}) \tag{B.1}$$

The original method Tauc et al. (1966) proposed, was slightly different. Instead of the mass absorption coefficient, Tauc used the imaginary part ε_i of the dielectric function:

$$\omega^2\varepsilon_i(\omega) \propto (\hbar\omega - E_{gap})^2 \tag{B.2}$$

We start by assuming that both expressions are equivalent. The left-hand side follows Tauc's findings, the right-hand side follows the more usual simplification:

$$\omega^2\varepsilon_i \propto \alpha\omega \tag{B.3}$$

$$\omega\varepsilon_i \propto \alpha \tag{B.4}$$

With $\alpha = \frac{4\pi k}{\rho\lambda}$, where k is the imaginary part of the refractive index at the wavelength λ, it follows that:

$$\omega\varepsilon_i \propto \frac{k}{\lambda} \tag{B.5}$$

ω and λ are related by $c = \frac{\omega\lambda}{2\pi}$, thus $\omega \propto \lambda^{-1}$. From here it follows that

$$\varepsilon_i \propto k \tag{B.6}$$

However, there is a relationship betweenε_i and k

$$\varepsilon_i = 2nk \tag{B.7}$$

From here we conclude, that the initial statement of equivalence is wrong, as it requires the real part n of the refractive index to be a constant, which it is not, except for vacuum. Hence, the simplified Tauc-relation needs a correction that accounts for n. Jäger et al. (2008a) uttered similar concerns. In the case of partially and fully annealed carbon made from pyrolysed cellulose, n varies significantly in the UV/VIS region, as shown by Jäger et al. (1998). The only option would be to measure the reflectance of the materials and derive the optical constants. That is not a trivial task, because amorphous carbon is nearly impossible polish.

To ensure consistency the area between $2\,eV$ and $4\,eV$ has always been chosen to be fitted. The Tauc relation allows one to compute the average length of the graphene layers according to Robertson and O'Reilly (1987). They give the following relation:

$$E_{gap} = \frac{2\beta}{\sqrt{M}} \tag{B.8}$$

Here, M is the number of aromatic rings and $\beta = 1.4\,eV$ is the Hückel-parameter. However, the authors caution that Equation B.8 only describes a trend. Furthermore, the above formalism only applies to planar structures.

B.1 Iron-Free Samples

The left side of Table B.1 shows the values derived for the AC samples. There is no apparent trend. The findings even disagree with the expected behaviour. In most samples graphitisation is observed, meaning that the material forms larger aromatic units and lower their gap energy. But especially thick samples for which graphitization is the dominant process, increase their band gap. Furthermore, form the HRTEM images we have seen that all samples increase the average length of the graphene layers by at least a factor of two.

Knowing the lattice parameter of the hexagonal structure of graphite being $a = 2.46$ Å, an approximate diameter can be derived as $d_{C6} = 2 \cdot \sqrt{\frac{3}{4}a^2} \approx 0.42nm$. If we assume the graphitic sub-structures to be planar spheres we can compute the expected diameter D of the sphere, which is roughly identical to what we can

Sample	$\mathbf{E_{gap}}$ $[eV]$	**M**	**Sample**	$\mathbf{E_{gap}}$[eV]	**M**
low iron content (AC)			**high iron content (HAC)**		
LA96-DUV	0.43	42	LA97-DUV	0.37	59
	0.97	8		0.81	12
LA107-DUV	0.49	32	LA110-DUV	1.3	5
	0.59	22		1.3	5
LA116-HUV	0.47	36	LA60-XUV	1.3	5
	0	∞		1.4	4
LA117-HUV	0.65	19	LA108-XUV	0.4	56
	0.66	18		0.4	54
LA59-XUV	1.3	5	LA112-X	0.7	15
	0.8	13		0.6	24
LA115-XUV	0.5	31			
	0.3	83			
LA114-X	0.29	96			
	0.35	65			

Table B.1: The table displays the gap energy E_{gap} and the derived number of aromatic rings in a sub-unit for various AC (left side) and HAC samples (right side). The last column give some more details about the microscopically and spectroscopically derived properties of the samples. The upper row of each entry denotes the unirradiated sample, the lower one denotes the irradiated sample.

observe as fiberlength in the HRTEM:

$$D(M) = \sqrt{\frac{4M}{\pi}} \cdot 0.42\,nm \tag{B.9}$$

The according cluster sizes are listed in Table B.2.

M	10	20	30	40	50	60	70	80	90	100
D [nm]	1.5	2.12	2.6	3.0	3.35	3.67	3.97	4.24	4.5	4.74

Table B.2: The diameter of plane aromatic structures according to Equation B.9.

Although that range of values is not unphysical, it is the lack of a trend and especially the fact that graphitized samples apparently decrease the size of their aromatic units — at least partially.

The values for the HAC-samples (Table B.1, right side) appear to be independent from whether they have been irradiated or not. Yet most of the samples experienced graphitization.

It should be noted that the gap energy, when derived that way, is highly dependent on the area that is chosen as linear slope. Table B.3 shows the dependence of the gap energy on the chosen range. The gap energy of the unirradiated sample is fairly independent from the chosen range. But the treated sample varies a lot.

Range	**Gap Energy**	
	unirradiated	*irradiated*
1-2	0.45	0.32
1-3	0.48	0.54
1-4	0.46	0.70
2-3	0.52	0.83
2-4	0.43	0.97
3-4	0.22	1.09

Table B.3: The table shows the gap energies of LA96 (AC, DUV) derived from a Tauc-plot with regard to different areas. Both the gap energy and range are given in eV.

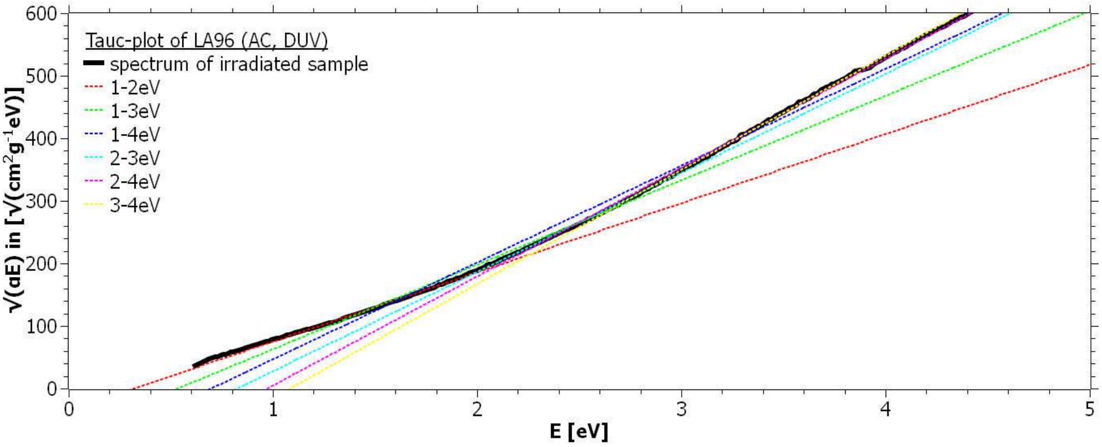

Figure B.1: This image shows the possible linear fits for the Tauc-plot of the irradiated LA96.

As it can be seen in Figure B.1, many of the fits represent the linear region, or the chosen parts, quite well. However, the resulting gap energies vary a lot.

The gap energies for the untreated sample are similar to each other, and the Tauc-plot seems to give a reasonable result in that case. However, for the treated sample it is ambiguous.

Before entering the subsection about the iron containing samples, of which we do not know for certain, whether the Tauc method can be applied to them, it appears reasonable to draw a conclusion: The combined methods of Tauc and Robertson do not yield reasonable results that match with the observations. There is a manifold of reasons that render the combination of these methods useless in this context. Firstly, the Tauc method of extrapolating the almost linear slope of the modified mass absorption coefficient is inaccurate. For samples which do not have a well-defined area with an almost linear slope, it is difficult to find the right area to fit (Figure B.1). Secondly, Robertson's approach is only valid for plane layers which we do not have as confirmed by the HRTEM. The bent graphene layers force the orthogonal $2p_z$-orbitals into a position which gives them a more sp^3-like character. Increasing the sp^3-like traits of the materials means that they behave more like a semi-conductor with a bigger band gap.

Although it is up to debate whether the combined method of Robertson and Tauc should be applied to iron-containing samples at all. The mass absorption coefficient of the iron-containing samples is influenced by the iron in two ways: Firstly, iron favours the formation of round graphene layers. Secondly, the iron itself cannot be removed from the spectrum, which is the main problem. The Tauc-relation is only valid for semi-conductors and non-metals. Anyway, the results are listed in Table B.4 in the appendix. Again, as for the other samples, the combined method does not show any clear trend or any trend whatsoever.

B.2 Iron-Containing Samples and the Tauc Relation

Sample	$\mathbf{E_{gap}}$ $[eV]$	**M**	**Sample**	$\mathbf{E_{gap}}$[eV]	**M**
low iron content (FeAC)			**high iron content (FeHAC)**		
LA9-ArF	0.73	15	LA14-ArF	1.4	4
	0.82	12		1.4	4
LA10-ArF	0.78	13	LA16-ArF	0.86	11
	0.73	15		0.94	9
LA25-DUV	0.81	12	LA28-DUV	1.4	4
	1.1	7		1.3	5
LA98-DUV	0.48	34	LA99-DUV	0.61	21
	0.77	13		0.85	11
LA103-HUV	0.71	15	LA43-XUV	1.2	5
	0.64	19		1.2	5
LA102-XUV	0.66	18	LA113-X	0.33	0.71
	0.60	22		0.27	107

Table B.4: The table displays the gap energy E_{gap} and the derived number of aromatic rings in a sub-unit for various iron-containing samples. The last column give some more details about the microscopically and spectroscopically derived properties of the samples. The upper row of each entry denotes the unirradiated sample, the lower one denotes the irradiated sample.

Acknowledgement

After a journey of four years the number of people I owe thank, is all but small.

I would like to express my gratitude to Prof. Thomas Henning for granting me the opportunity to pursue this thesis. Furthermore I would like to thank all my colleagues of the laboratory astrophysics group of the Max-Planck-Institut für Astronomie for the support, especially Dr. Cornelia Jäger for advising and guiding me, and to Dr. Gaël Rouillé who helped me on a number of technical issues. I also would like to express my gratitude to the laboratory astrophysics group at the AIU, especially Dr. Harald Mutschke for allowing me to use his facilities and spectrometers, Gabriele Born for her technical support, and Pierre Mohr for innumerable fruitful discussions.

Last, but not least, I would like to thank Dorottya Zsófia Koppenhagen, Jöran Krusch and my family for their support and patience, and the faculty's cat, Lilly, for keeping my motivation high.

Cui dono lepidum novum libellum
arida modo pumice expolitum?
Corneli, tibi; namque tu solebas
meas esse aliquid putare nugas,
Iam tum cum ausus es unus Italorum
omne aevum tribus explicare chartis,
Doctis, Iuppiter, et laboriosis!
Quare habe tibi quidquid hoc libelli
Qualecumque, quod, o patrona virgo,
Plus uno maneat perenne saeclo.

Gaius Valerius Catullus, Carmen 1

Ehrenwörtliche Erklärung

Hiermit erkläre ich, Hagen Walter, dass ich diese Arbeit selbständig und ohne unzulässige Hilfe Dritter sowie nur unter Benutzung der angegebenen Quellen angefertigt habe. Von anderen Autoren übernommene Daten sind mit der Quellenangabe als solche gekennzeichnet.
Von den folgenden Personen habe ich Zuarbeit erhalten:

- **Dr. Cornelia Jäger** hat viele der HRTEM-Aufnahmen gemacht. Einen kleinen Teil der Aufnahmen haben wir gemeinsam gemacht
- **Dr. Eva Kovacevic** hat für mich die Bestrahlungen und NEXAFS-Messungen der Proben LA23, LA37 und LA38 am BESSY vorgenommen.
- **Dr. Michael Zürch und Frederik Tuitje** haben die Bestrahlungen mit dem Multiharmonicslaser am IOQ durchgeführt.
- **Horia Popescu** hat die Bestrahlungen der Proben LA112, LA113 und LA114 am Synchrotron SOLEIL gesteuert und überwacht.
- **Gabriele Born** hat einige der Eisen-Kohlenstofftargets nach meinen Vorgaben gemischt und gepresst.

Weitere Personen waren an der inhaltlichen Erstellung der vorliegenden Arbeit nicht beteiligt. Insbesondere habe ich hierfür nicht die entgeltliche Hilfe von Vermittlungs- oder Beratungsdiensten (Promotionsberater oder andere Personen) in Anspruch genommen. Niemand hat von mir unmittelbar oder mittelbar geldwerte Leistungen für Arbeiten erhalten, die mit dem Inhalt der vorliegenden Arbeit im Zusammenhang stehen.
Die Arbeit wurde bisher weder im In- noch im Ausland in gleicher oder ähnlicher Form einer anderen Prüfungsbehörde vorgelegt.
Die geltende Promotionsordnung der Physikalisch-Astronomischen Fakultät ist mir bekannt.

Ich versichere ehrenwörtlich, dass ich nach bestem Wissen und Gewissen die reine Wahrheit gesagt und nichts verschwiegen habe.

Hagen Walter,Jena, den 05.04.2017

Curriculum Vitae

	Walter, Hagen
Geburtsdatum:	23.01.1989
Geburtsort:	Nordhausen
1995-1999	staatl. Grundschule *Käthe Kollwitz* in Nordhausen
1999-2007	staatl. Gymnasium *Wilhelm von Humboldt* in Nordhausen
2007-2010	Studium der Physik (BSc) an der *Friedrich-Schiller-Universität* in Jena, Schwerpunkte: Astronomie und Optik, Bachelorant in der AG Laserstrahlcharakterisierung am Institut für Angewandte Optik (IAO), Betreuer: Dr. M. Duparré und Prof. Dr. R. Kowarschik
2010-2013	Studium der Physik (MSc) an der *Friedrich-Schiller-Universität* in Jena, Schwerpunkte: Astronomie und Optik, Masterand in der AG Laborastrophysik am Astrophysikalischen Institut (AIU), Betreuer: Dr. H. Mutschke, Dr. C. Jäger und Prof. Dr. A. Krivov
2013-2017	Doktorand der Astrophysik in der AG Laborastrophysik des *Max-Planck-Instituts für Astronomie Heidelberg* an der *Friedrich-Schiller-Universität* in Jena, Betreuer: Dr. C. Jäger und Prof. Dr. Th. Henning